6-2019

An Analysis of Differential Reflectivity Arc Characteristics in 109 Supercell Storms

Matthew Wilson
University of Nebraska - Lincoln, mwilson41@huskers.unl.edu

AN ANALYSIS OF DIFFERENTIAL REFLECTIVITY ARC CHARACTERISTICS IN 109 SUPERCELL STORMS

by

Matthew B. Wilson

A THESIS

Presented to the Faculty of

The Graduate College at the University of Nebraska

In Partial Fulfillment of Requirements

For the Degree of Master of Science

Major: Earth and Atmospheric Sciences

Under the Supervision of Professor Matthew S. Van Den Broeke

Lincoln, NE

June, 2019

AN ANALYSIS OF DIFFERENTIAL REFLECTIVITY ARC CHARACTERISTICS IN 109 SUPERCELL STORMS

Matthew B. Wilson, M.S.

University of Nebraska, 2019

Advisor: Matthew S. Van Den Broeke

Differential reflectivity (Z_{DR}) arcs are one of the most prominent dual-polarization features of supercell storms, and are manifest as an arc-shaped area of high Z_{DR} along a supercell's forward flank reflectivity gradient. Since previous modelling studies have hypothesized that the magnitude of the drop-size sorting by the storm-relative wind which creates the arc signature is related to the strength of the low-level shear and SRH in a storm's environment, the presence of a strong Z_{DR} arc is often said to indicate that a storm may have the potential to develop strong low-level rotation and potentially become tornadic. However, observational studies of Z_{DR} arcs characteristics in large ($n > 100$) samples of supercells and the relationship of these characteristics to environmental parameters, low-level rotation strength, and whether a storm produces a tornado or not have yet to be conducted. This study intends to fill that knowledge gap, using an automated Python algorithm to identify, track, and analyze Z_{DR} arc characteristics in 109 supercells. This dataset is then used to examine the impact of various environmental parameters (obtained from proximity RAP analyses) on arc size and intensity, as well as whether arc characteristics can indicate whether a storm will develop strong rotation and whether arc characteristics differ between tornadic and nontornadic storms. Finally, a similar analysis is performed using another proxy for drop-size sorting in supercells—the

separation angle between the Z_{DR} arc and K_{DP} foot centroids. Results of these analyses indicate that Z_{DR} arc characteristics are much more dependent on instability and moisture parameters than on low-level shear and SRH and that changes in Z_{DR} arc size and intensity do not reliably foreshadow low-level rotation changes on timescales of up to 15 minutes. Furthermore, Z_{DR} arc size and intensity are not meaningfully different between tornadic and nontornadic supercells. However, a consistent increase in arc areal extent was found shortly before tornadogenesis (peak normalized rotation (NROT)) in tornadic (nontornadic) storms, and the K_{DP}-Z_{DR} separation angle was found to be substantially larger in tornadic supercells than in those which did not produce tornadoes.

Acknowledgements:

I would like to thank my advisor, Dr. Matthew Van Den Broeke, for providing excellent guidance throughout my Master's work and plenty of freedom to take my project in interesting directions. Comments and critiques from committee members Dr. Mark Anderson and Dr. Adam Houston have also been instrumental in shaping this project, and I would especially like to thank Dr. Houston for tolerating my goofy puns on three successive field campaigns. Finishing this thesis would have been immeasurably more difficult without the encouragement of friends here in Lincoln, and I would especially like to thank my officemates Nancy Barnhardt and Kun-Yuan Lee, Stephen Shield for his help with random forests, and Adrianne Engel for her assistance in interpreting the parts of the supercell dataset that I inherited from previous projects. Finally, the support from my parents and my sister has been instrumental during my grad school experience and is greatly appreciated. I would also like to thank NSF grant IIA-1539070 for providing financial support for this research.

Table of Contents

Multimedia Objects

Chapter I: Introduction

Though supercell storms represent a small fraction of all thunderstorms, they are responsible for a disproportionate amount of severe weather reports in the United States, producing 51 percent of total severe weather reports and 68.2 percent of tornado reports in the Midwest in one two-year study period despite representing only 22.8 percent of all storms examined (Duda et al. 2010). With the advent of dual-polarization (dual-pol) radar and the subsequent upgrade of the WSR-88D radar network, several dual-pol signatures have been identified in supercell storms which may be of use in determining a particular supercell's likelihood of producing severe wind, large hail, or a tornado (Kumjian and Ryzhkov 2008a; Van Den Broeke et al. 2008; Romine et al. 2008). These signatures include tornadic debris signatures (Ryzhkov et al. 2005; Van Den Broeke and Jauernic 2014; Snyder and Ryzhkov 2015), hail signatures in the core and forward flank (Dawson et al. 2014a; Van Den Broeke 2016), differential reflectivity (Z_{DR}) columns associated with convective updrafts (Snyder et al. 2015; Van Den Broeke 2016), and the Z_{DR} arc along the supercell's forward flank reflectivity gradient (Kumjian and Ryzhkov 2008a, 2009; Dawson et al. 2014a,b).

Among these supercell dual-pol signatures, initial studies (Kumjian and Ryzhkov 2008a, 2009; Kumjian et al. 2010; Palmer et al. 2011; Crowe et al. 2012, among others) have indicated that the Z_{DR} arc may show particular promise for use in operations, since it may be able to provide information about both the low-level near-storm environment and the strength of the storm's low-level inflow. The Z_{DR} arc is formed as precipitation particles falling through a supercell's forward flank are sorted by the storm-relative flow, with smaller drops taking longer to fall and thus being advected farther into the storm

core by the storm-relative wind than larger drops (Kumjian and Ryzhkov 2008a, 2009; Dawson et al. 2014a,b). Since larger drops are more oblate and thus produce higher Z_{DR} values (Seliga and Bringi 1976), this results in an arc-shaped area of high Z_{DR} along a supercell's forward flank reflectivity gradient as smaller drops are sorted out of this region. Size-sorted melting hail may also contribute to enhancing Z_{DR} in a supercell's forward flank in addition to raindrop size sorting, albeit in an area slightly closer to the storm core than the traditional Z_{DR} arc (Dawson et al. 2014a). Since the strength of the storm-relative wind is often correlated to the low-level wind shear and storm-relative helicity magnitude, Z_{DR} arc size and intensity may be a useful proxy for changes in these environmental characteristics on scales smaller than those resolved by the radiosonde network (Kumjian and Ryzhkov 2008a, 2009; Dawson et al. 2014b). Observational work by Van Den Broeke (2016) examining Z_{DR} arc characteristics in 25 classic supercells in 12 different environments found that Z_{DR} arc width, area extent, and mean Z_{DR} value were well-correlated with low-level bulk shear; however, other environmental variables such as midlevel relative humidity and the height of the level of free convection (LFC) also influenced the size and intensity of the Z_{DR} arc. Thus, further work examining a larger number of supercells in different environments may be useful in eliciting what Z_{DR} arc metrics can indicate to forecasters about a supercell's environment.

In addition to environmental information, changes in Z_{DR} arc metrics may also shed light on the progression of supercell and tornado life cycles. Palmer et al. (2011) observed a cyclic pattern of Z_{DR} arc evolution in a violently tornadic supercell during the 10 May 2010 tornado outbreak in Oklahoma, with the Z_{DR} arc extending back toward the hook echo leading up to tornadogenesis and weakening around tornado demise and

occlusion, only to strengthen again as a new mesocyclone became established and produced another tornado. Kumjian et al. (2010) documented a similar pattern of evolution during the cycling process of a nontornadic supercell in central Oklahoma, with the Z_{DR} arc strengthening and extending back toward the hook echo leading up to mesocyclone occlusion and weakening following occlusion. Z_{DR} arc behavior across tornado life cycles has also been investigated by Van Den Broeke (2017), with arcs observed to grow larger and wider from tornadogenesis to tornado dissipation. However, a study of Z_{DR} arc behavior leading up to tornadogenesis or tornadogenesis failure and over the mesocyclone cycling process in a larger sample of supercells has not yet been attempted.

This thesis will focus on examining Z_{DR} arc characteristics in a large sample of supercell storms and determining what operationally useful information can be gleaned from them. Background information on supercell dual-pol signatures, particularly the Z_{DR} arc, is provided in Chapter II. Chapter III describes the datasets and methodology employed in this study, including the development and testing of an automated Z_{DR} arc detection and tracking algorithm to objectively analyze Z_{DR} arc characteristics in a large sample of supercells, the development of the supercell dataset, and the methods employed in calculating low-level rotation metrics and analyzing mesocyclone cycling for each storm. Chapter IV presents the results of these analyses, with section I focusing on using the Z_{DR} arc characteristics output by the automated algorithm to examine how Z_{DR} arc characteristics change with various environmental parameters. Similarly, section II examines whether variations in low-level rotation in supercells are correlated with changes in Z_{DR} arc variables, section III explores arc changes over supercell and tornado

life cycles, and section IV explores how the separation of the K_{DP} foot and Z_{DR} arc varies with low-level shear and SRH and between tornadic and nontornadic storms. Section V summarizes the conclusions of this work and where they may be useful in operations, as well as presenting potential avenues for future research.

Chapter II: Background

I. Supercells and their Dual-Polarization Signatures

a. Supercells

Supercells are generally defined as storms with a deep, persistent rotating updraft known as a mesocyclone, and are often prolific severe weather producers. For example, Smith et al. (2012) found that supercells produced over 95% of EF3 or stronger tornadoes and 2 inch or larger hail in their sample of 22,901 significant severe weather events. Previous research has extensively documented the origins of rotation in the mesocyclone from tilting into the vertical of streamwise horizontal vorticity induced by environmental vertical wind shear (Wilhelmson and Klemp 1978; Davies-Jones 1984) and the effects that updraft rotation and vertical wind shear have on supercell organization, strength, and longevity (Rotunno and Klemp 1982; Weisman and Klemp 1982; Bunkers et al. 2006). The ingestion of streamwise vorticity can be quantified by calculating storm-relative helicity (SRH)—defined as twice the area swept out by the storm-relative wind vector over a given depth on a hodograph. Higher values of SRH for a given hodograph and storm motion can indicate a greater chance of a supercellular storm mode given that sufficient instability, moisture, and lift exist for deep convection. SRH tends to be maximized with a hodograph that veers significantly with height. However, SRH can still be substantial with a straight-line hodograph provided that a storm propagates off the hodograph and thus generates a component of the storm-relative wind parallel to the shear-induced vorticity vectors (Moller et al. 1994). Since the horizontal vorticity available to be tilted depends on the strength of the environmental shear, bulk shear

magnitude has also proven to be a useful parameter in differentiating between supercell and nonsupercell environments (Thompson et al. 2003; Houston et al. 2008).

Due to the presence of a mesocyclone and the vertical shear which helps create it, supercells have several unique visual and radar features. On radar, these include a sharp reflectivity gradient on the inflow side of the storm's precipitation shield, a bounded weak echo region or echo overhang associated with the mesocyclone, and a hook or pendant echo. Visually, supercells are often distinguished by a lowered area of cloud known as a wall cloud beneath the often rain-free updraft base, an inflow tail cloud which may feed into the wall cloud from along the edge of the forward flank precipitation, a tilted and sometimes spectacularly-striated updraft column, and a flanking line which often feeds into the main updraft along or ahead of the rear flank downdraft (RFD) boundary (Moller et al. 1994). These features are outlined in figure 2.1 from both a plan view radar perspective and a visual perspective. Although all supercells by definition have a rotating mesocyclone, the presence and presentation of these other features can vary greatly from the 'classic' morphology presented in figure 2.1. Some supercells, known as high-precipitation (HP) storms, have large amounts of precipitation in their mesocyclones, which can obscure many of the aforementioned visual features and can lead to a more bow-echo-like or ill-defined radar structure. Others, known as low-precipitation (LP) storms, have comparatively little precipitation overall, and often have spectacular visual presentations but somewhat innocuous radar signatures (Moller et al. 1994; Rasmussen and Straka 1998).

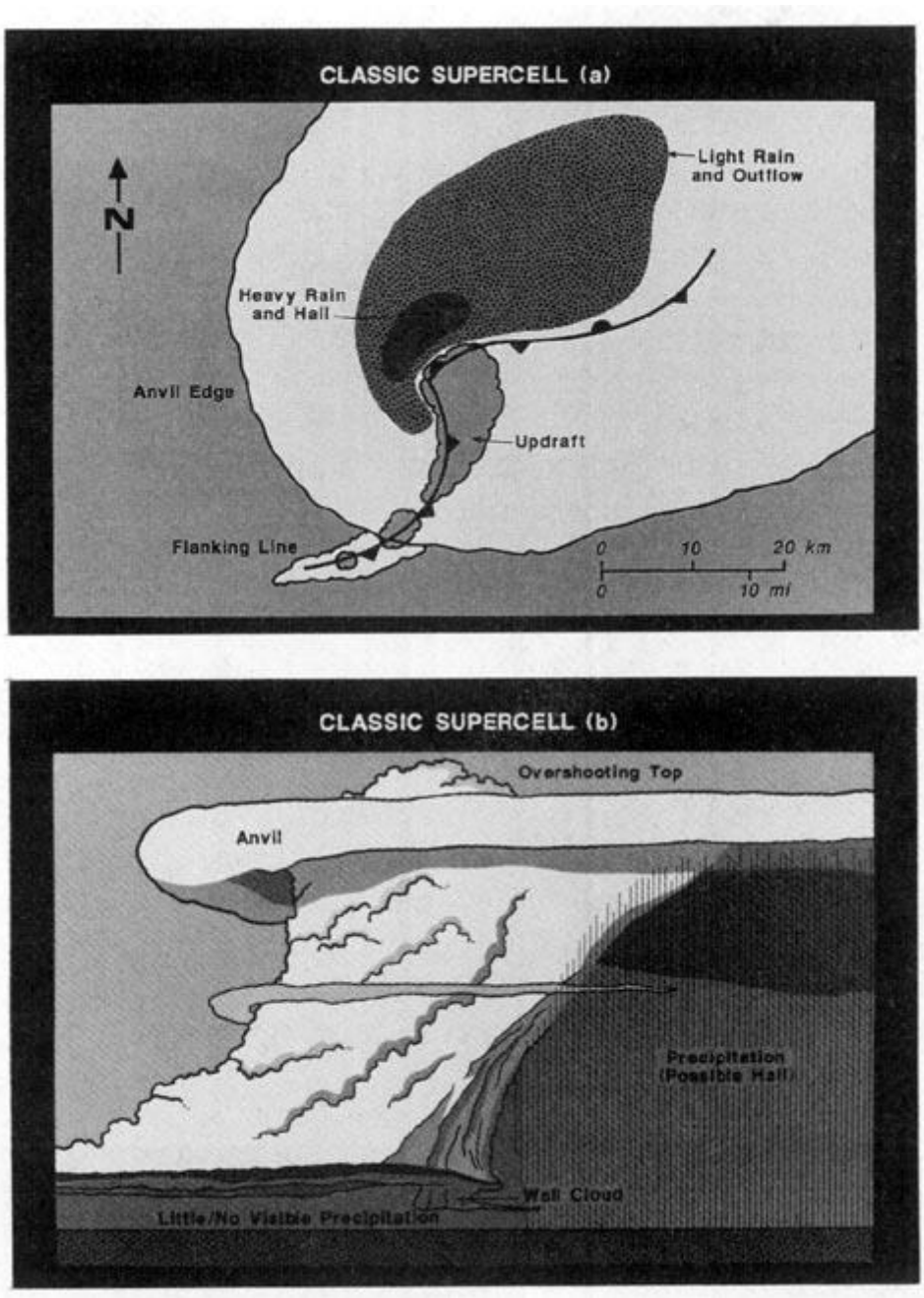

Figure 2.1: A diagram of classic supercell structure, showing (a) plan view of typical supercell features as might be seen on radar and (b) a visual perspective as seen by an observer to the east of the supercell. (Figure 1 from Moller et al. (1994))

One other feature common to many supercells is a cyclic process of mesocyclone replacement. Once a mesocyclone becomes wrapped in outflow air and cut off from its inflow, it tends to weaken and moves to the left of storm motion, while a new mesocyclone often forms along the rear flank outflow boundary and becomes the dominant updraft until undergoing occlusion itself (Adlerman et al. 1999; Dowell and Bluestein 2002; Beck et al. 2006). In tornadic storms, cyclic mesocyclogenesis can be associated with cyclic tornado formation (Lemon and Doswell 1979), with successive mesocyclones producing one or more tornadoes as shown in figure 2.2. (Dowell and Bluestein 2002). Moreover, various modes of cycling exist, with some supercells not undergoing occlusion and progressing in a quasi-steady-state fashion, some undergoing occlusions of varying frequencies, and some cycling without old mesocyclones undergoing occlusion in a process known as non-occluding cyclic mesocyclogenesis (Adlerman and Drogomeier 2005).

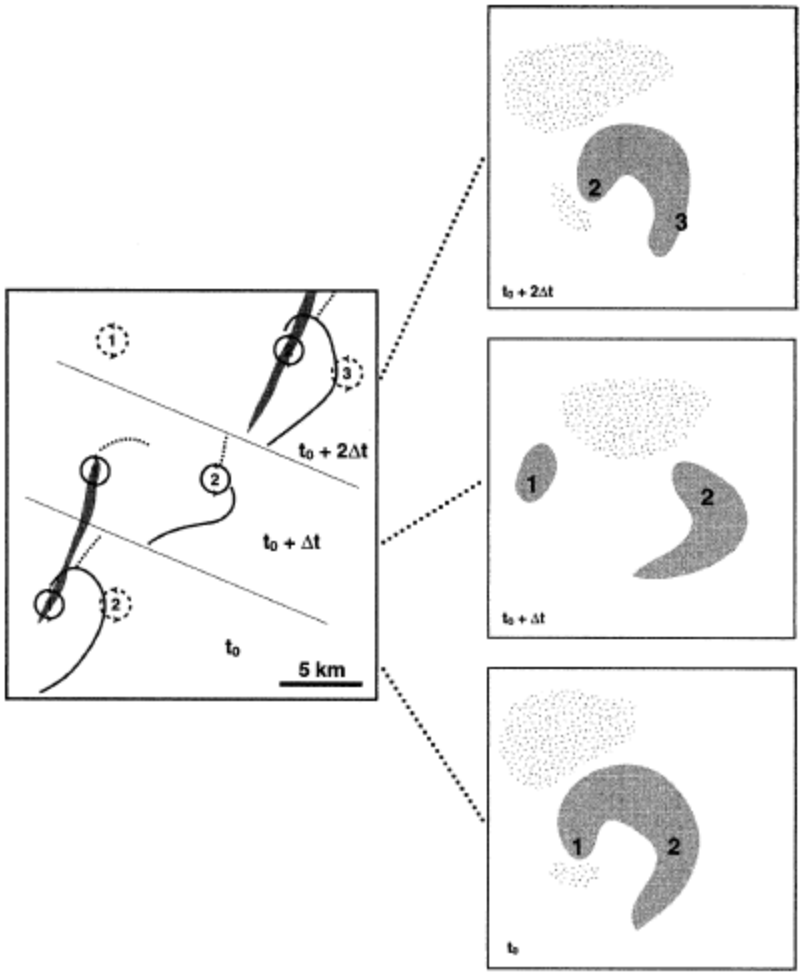

Figure 2.2: A plan view of low-level features during cyclic tornadogenesis. Mesocyclones are numbered, updrafts are shaded, and downdrafts are stippled in the figures on the right. In the figure on the left, tornado tracks are shaded black, while the lines indicate wind shift boundaries (Dowell and Bluestein (2002)'s figure 13).

Although supercells produce most of the tornadoes and the vast majority of strong tornadoes in the US (Duda and Gallus 2010; Smith et al. 2012), not all supercells are tornadic, with only 26% of mesocyclones detected by the WSR-88D Mesocyclone Detection Algorithm producing observed tornadoes (Trapp et al. 2005). Previous research

indicates that tornadic supercells tend to have stronger low-level mesocyclones than nontornadic storms (Coffer and Parker 2017; Thompson et al. 2017), which may be partially due to tornadic environments having greater low-level storm-relative helicity and thus more streamwise vorticity available for the updraft to tilt (Thompson et al. 2003; Esterheld and Giuliano 2008). Furthermore, the rear-flank outflow in nontornadic supercells has been found to be colder and less buoyant than in significantly tornadic storms (Markowski et al. 2002; Weiss et al. 2015). Much of the recent work on supercell tornadogenesis has focused on the source of low-level vorticity for the tornado being the tilting and subsequent convergence and stretching of baroclinically generated vorticity in outflow air (Rotunno et al. 1985; Markowski et al. 2008; Orf et al. 2017). Thus, the presence of stronger updrafts and more buoyant rear flank outflow in tornadic supercells makes sense, since both of these characteristics would allow a low-level mesocyclone to stretch baroclinically-generated near-surface vorticity in the outflow beneath it to tornado strength more easily through stronger rotationally-generated vertical perturbation pressure gradient forces (Davies-Jones 2015; Coffer and Parker 2017). However, timely and high-resolution measurements of outflow thermodynamics and local variations in SRH and low-level shear are seldom available to forecasters, which makes using these characteristics operationally to differentiate tornadic and nontornadic supercells a difficult task. Thus, techniques which might allow inferences to be made about these parameters using available observations would likely be useful.

b. Supercell Polarimetric Signatures

One observation platform which has shown promise in providing timely data on otherwise difficult-to-observe characteristics of severe storms is dual-polarization radar.

Instead of sending out one horizontally polarized signal as legacy radars (including the pre-dual-pol-upgrade Weather Surveillance Radar 1988-Doppler (WSR-88D) network) do, dual-polarization radars send and receive data at two orthogonal polarizations. Having data at two orthogonal polarizations allows dual-pol radars to collect much more information about the characteristics of scatterers in a sample volume and produce several new radar variables, including differential reflectivity (Z_{DR}), specific differential phase (K_{DP}) and correlation coefficient (CC) (Zrnić and Ryzhkov 1999). Z_{DR} is the difference between reflectivity returned at horizontal polarization and reflectivity returned at vertical polarization and can be thought of as a measure of the oblateness of scatterers in a sample volume, with higher values of Z_{DR} indicating increasing oblateness. Since larger raindrops tend to be more oblate than smaller raindrops or dry snow aggregates, higher values of Z_{DR} can indicate that the drop size distribution in a sample volume is dominated by larger liquid drops (Seliga and Bringi 1976; Rinehart 2010). K_{DP} is the along-beam spatial derivative of the difference in phase shift between the horizontal and vertical signal. Since liquid drops lead to much larger phase shifts than ice particles, and the oblateness of many drops will cause a greater phase shift in the horizontal signal, K_{DP} increases with liquid water content in a sample volume (Zrnić and Ryzhkov 1999; Rinehart 2010). Finally, CC is a measure of the correlation of the returned signals at horizontal and vertical polarizations. High values of CC indicate a low diversity of scatterers in a sample volume, meaning that the radar is likely sampling relatively uniform hydrometeors such as pure rain or dry snow. Low values of CC indicate a high diversity of scatterers, which can come from several different sources

including biological scatterers, mixed precipitation, and lofted tornadic debris (Zrnić and Ryzhkov 1999; Ryzhkov et al. 2005, Rinehart 2010).

Observations of supercells using dual-polarization radar have revealed several repeatable dual-polarization signals which may give forecasters useful information about a storm's dynamics, thermodynamics, and microphysics. These features include the Z_{DR} column, K_{DP} foot, hail fallout signature, tornadic debris signature, and Z_{DR} arc; their placement within a typical supercell is shown in figure 2.3 (Kumjian and Ryzhkov 2008a; Van Den Broeke et al. 2008; Romine et al. 2008). The Z_{DR} column (Illingworth et al. 1987, Kumjian et al. 2014; Van Den Broeke 2016) is a protrusion of positive Z_{DR} above the environmental freezing level in a storm, and represents large raindrops lofted above the freezing level by a thunderstorm updraft. Z_{DR} columns can be used to track the location and strength of updrafts, and an automated algorithm has been developed to track them in WSR-88D data (Snyder et al. 2015). The K_{DP} foot (Romine et al. 2008) is an area of enhanced K_{DP} due to high liquid water content in the core of a storm. Persistent, very high values of K_{DP} in this region (>8 deg km^{-1}) can indicate the potential for large accumulations of small hail (Ward et al. 2018). Larger, dry hail tends to have low K_{DP} values and near-zero values of Z_{DR} due to the tumbling of individual hailstones, and often produces a distinctive fallout signature just downshear from the mesocyclone in the forward flank (Van Den Broeke et al. 2008, 2016). In addition to indicating the presence of large hail, there are some indications that cyclic changes in the hailfall field may be different between tornadic and nontornadic storms (Van Den Broeke 2016). Tornadic debris signatures (TDSs, Ryzhkov et al. 2005) occur when high rotational velocity is collocated with a vertical plume of low CC, high reflectivity, and low Z_{DR}

associated with the diverse scatterers present in debris lofted by a tornado. The presence of a TDS is a useful tool for confirming an ongoing tornado, and recent research indicates that TDS height and areal extent can be an indicator of tornado intensity (Van Den Broeke and Jauernic 2014). An automated algorithm has also been developed to detect TDSs in WSR-88D data (Snyder and Ryzhkov 2015).

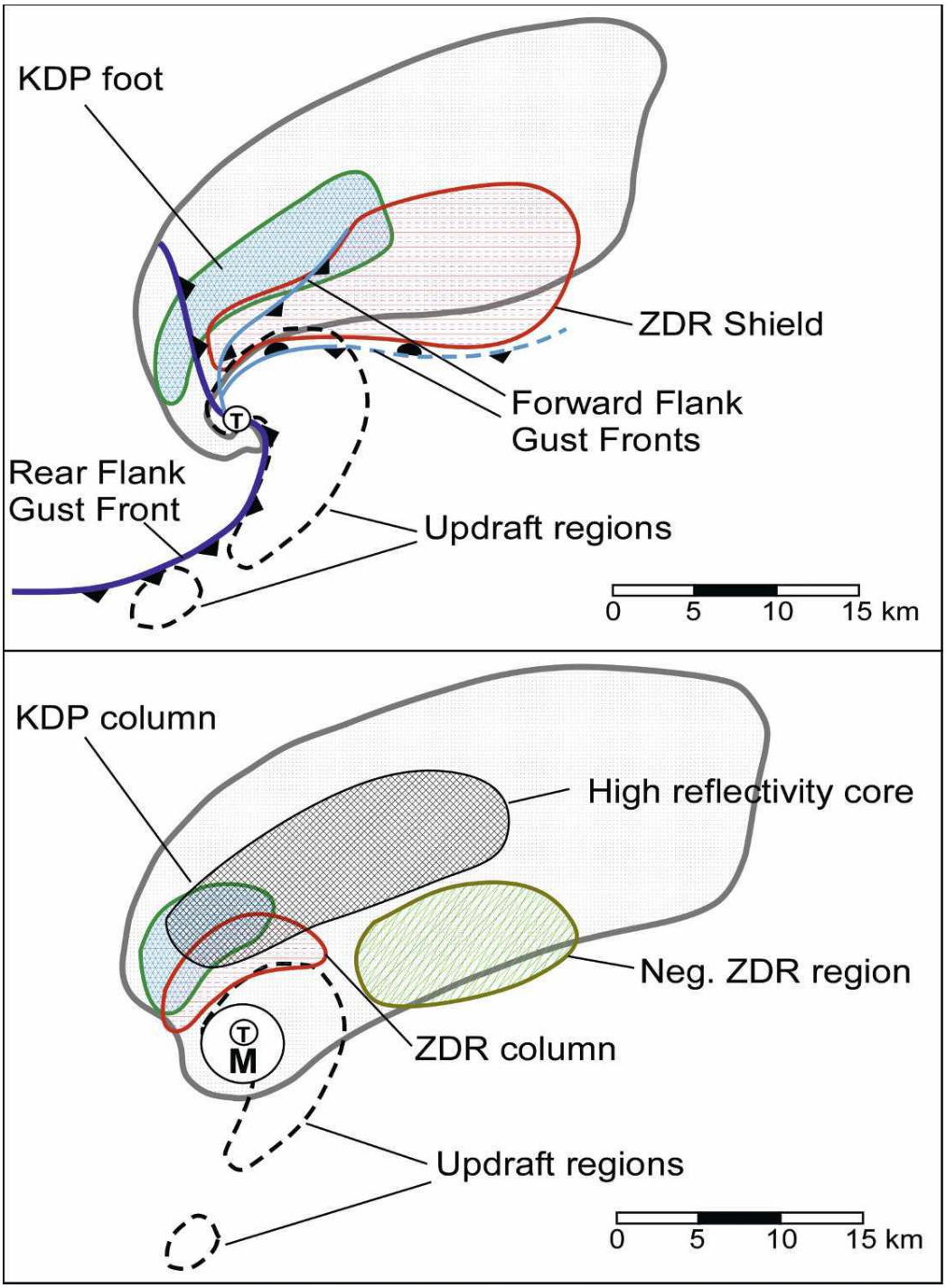

Figure 2.3: Horizontal cross-sections of an idealized supercell showing the locations of various dual-polarization signatures at low-levels (top) and mid-levels (bottom) (Figure 19 of Romine et al. (2008)).

II. The Z_{DR} Arc

The Z_{DR} arc was defined by Kumjian and Ryzhkov (2008a) as an area of high Z_{DR} on the inflow side of a supercell's forward flank, located along the strongest reflectivity gradient and often containing Z_{DR} values as high as 4 to 5 dB, with a typical threshold of ~3 dB often used to define its boundaries. Although Kumjian and Ryzhkov (2008a) coined the term "Z_{DR} arc," this area of enhanced Z_{DR} along a supercell's forward flank reflectivity gradient had been noted before by Ryzhkov et al. (2005), and Van Den Broeke (2008) had also observed high Z_{DR} values in the same region while creating a composite dual-pol schematic for several Great Plains supercells. A similar region of enhanced Z_{DR} was also identified by Romine et al. (2008) in the parent supercell for the 2003 Moore, Oklahoma F4 tornado and was referred to as the Z_{DR} shield. Several of these initial studies (Ryzhkov et al. 2005, Kumjian and Ryhzkov 2008a, Van Den Broeke 2008) attributed the high Z_{DR} values in the forward flank to drop size sorting due to vertical wind shear in the storm's environment. In a typical supercell environment with vertically veering winds, since small, more spherical drops fall more slowly than large, oblate drops, vertical wind shear would have longer to act on small drops and would advect them farther into the storm core than large drops. This would leave a drop size distribution in the Z_{DR} arc region heavily skewed toward large, oblate drops with high Z_{DR} (Seliga and Bringi 1976), accounting for the high Z_{DR} observed in this area (Kumjian and Ryzhkov 2008a, 2009).

Subsequent studies of Z_{DR} arcs built on this initial foundation by exploring possible operational implications of the Z_{DR} arc signature and refining the mechanism responsible for the drop size sorting in the arc region. Kumjian and Ryzhkov (2009)

hypothesized that the Z_{DR} arc signature was caused by extreme drop size sorting due to a storm-inflow-augmented veering low-level wind profile common in supercell environments, and that the strength of the Z_{DR} arc could thus be used to infer environmental storm-relative helicity from dual-pol radar data. Using an idealized model to simulate a simplified storm in different vertical wind profiles and with different initial drop size distributions, they found a strong correlation between the maximum Z_{DR} values in simulated Z_{DR} arcs and the environmental storm-relative helicity in the lowest 3 km above the ground (Kumjian and Ryzhkov 2009). Since supercells can substantially increase the low-level SRH in their near-inflow environment over that present in their far-field environment by accelerating and backing low-level flow towards their inflow lows (Parker 2014), Z_{DR} arc signatures could thus have some utility helping diagnose how much low-level SRH a supercell is actually ingesting compared to that present in the background environment. Dawson et al. (2014b) expanded on this conclusion by demonstrating with a series of idealized model simulations that the physical mechanism for drop-size sorting in the Z_{DR} arc is not low-level shear or storm-relative helicity, but rather the average storm-relative wind in the layer over which the size sorting occurs. Thus, wind shear is only strictly necessary for size sorting if the storm motion vector lies on the hodograph (i.e. without vertical wind shear there is no storm-relative wind anywhere in the column) and shear is needed to create a nonzero storm-relative wind in the size sorting layer. For supercells with motions which propagate off the hodograph, the strong correlation between Z_{DR} arc magnitude and storm-relative helicity is found to be due to a correlation between storm-relative helicity and storm-relative wind, with curved hodographs typical of supercell environments having higher storm-relative helicity when

storm-relative winds are stronger in the same layer (Dawson et al. 2014b). Furthermore, the contribution of size sorting by the storm-relative wind to the Z_{DR} arc may not be limited to the sorting of rain, with size sorting of melting hail found to play an important role in producing high Z_{DR} values in supercell forward flanks in the simulations of Dawson et al. (2014a), although this enhancement may be located closer to the storm core than would be typically expected for the Z_{DR} arc.

Initial observational studies of Z_{DR} arcs in supercells indicated that temporal variations in Z_{DR} arc size and intensity may be related to mesocyclone cycling and possibly to tornado production in tornadic storms. Kumjian et al. (2010) found a repetitive pattern of changes in the Z_{DR} arc of a nontornadic supercell in central Oklahoma on 1 June 2008 and related this pattern to the cycling of the storm's low-level mesocyclone. The storm's Z_{DR} arc was found to strengthen and extend back toward the mesocyclone until occlusion began, at which point the arc would quickly shrink or dissipate due to the less intense inflow during occlusion, weakening the size sorting responsible for the arc. A new arc then begins to form as precipitation previously held aloft by the updraft in the echo overhang falls out along the edge of the forward flank as the updraft weakens, leading to a small area of high Z_{DR} values. This then expands into a new Z_{DR} arc as the updraft re-intensifies and produces stronger low-level inflow, which restores size sorting in the arc region (Kumjian et al. 2010). A similar pattern of cyclic changes in Z_{DR} arc strength was observed in a tornadic supercell from the 10 May 2010 outbreak in central Oklahoma by Palmer et al. (2011). As noted by Kumjian et al. (2010), this storm's Z_{DR} arc was disrupted during occlusion and reformed as the new low-level mesocyclone strengthened. However, in this storm tornadogenesis occurred during the

organization of the new Z_{DR} arc, indicating that changes in Z_{DR} arc characteristics may be able to help indicate a storm's chance of producing a tornado as well as where it is in the cyclic mesocyclogenesis process at a given time (Palmer et al. 2011). It is not known how prevalent this pattern of Z_{DR} arc evolution is in cyclic supercells, and an examination of whether this pattern holds in a larger sample of supercells would likely be useful. It is also important to note that not all supercells, tornadic or otherwise, have a well-defined Z_{DR} arc (Van Den Broeke and Van Den Broeke 2015).

Observational work examining Z_{DR} arcs in larger samples of supercells has mainly focused on environmental controls on Z_{DR} arc characteristics and changes in Z_{DR} arcs across tornado life cycles. Van Den Broeke (2016, hereafter VDB16) examined the variability of several different polarimetric signatures—including Z_{DR} arcs—in 25 supercells across 12 different environments. Z_{DR} arc size and intensity were quantified using three different metrics: the width of the 2-dB Z_{DR} arc perpendicular to each storm's forward flank reflectivity gradient, the mean Z_{DR} value in the 2-dB Z_{DR} arc, and the areal extent of the 3.5-dB Z_{DR} arc. In keeping with previous results indicating that drop size sorting by the storm-relative wind is responsible for the formation of the Z_{DR} arc (Dawson et al. 2014b), VDB16 found that all arc metrics increased with increasing 1-3 km shear magnitude, and Z_{DR} arc width tended to increase with increasing storm-relative wind in the 0-2 km layer. However, moisture and thermodynamic variables were also important controls on arc size and intensity, although most were less well-correlated with arc metrics than 1-3 km shear. Z_{DR} arc width and areal extent were found to increase with higher most-unstable CAPE (MUCAPE), arc extent and mean value increased with higher level of free convection (LFC) heights, and all arc metrics decreased with midlevel

relative humidity (RH, 3-6 km RH for arc width and extent, 6 km RH for mean Z_{DR} value). VDB16 hypothesized that the broader initial drop-size distributions produced in stronger updrafts in higher MUCAPE environments help enhance size sorting and lead to larger and more intense arcs, while higher LFCs and lower midlevel relative humidity could have a similar effect by causing precipitation to form at a greater altitude and allowing a greater depth over which size sorting can act. In a subsequent study, Van Den Broeke (2017, hereafter VDB17) examined the variability of polarimetric signatures across tornado life cycles, including the Z_{DR} arc metrics used in VDB16, in 35 tornadic supercells. Over two-thirds of storms examined by VDB17 had larger Z_{DR} arc areas and mean values at tornadic times than nontornadic times, and over half had larger Z_{DR} arc widths. However, the differences were relatively small for operational use, with average differences in Z_{DR} arc area of 16 km^2 and in Z_{DR} arc width of 0.5 km. Similar relatively small increases in Z_{DR} arc areal extent and width were found from tornadogenesis to tornado demise. Finally, variability in Z_{DR} arc mean value and width were found to be higher in significantly tornadic storms, and Z_{DR} arc widths were larger in storms which produced EF3+ tornadoes (VDB17).

One final aspect of the Z_{DR} arc which has been examined in previous literature is the separation between the Z_{DR} enhancement in the forward flank and the area of enhanced K_{DP} typically found within the storm core. First examined in detail by Crowe et al. (2010) in three supercells in Hurricane Rita's rainbands, this separation is attributable to the same drop-size sorting that creates the Z_{DR} arc. Thus, it may also be useful as a proxy for the low-level storm-relative wind and quantities related to it, such as low-level shear, storm-relative helicity, and storm inflow (Crowe et al. 2010, 2012). Following up

on Crowe et al. (2010)'s finding that the separation of Z_{DR} and K_{DP} maxima in a tornadic supercell in Hurricane Rita's outer bands was greater and more persistent than in a nontornadic supercell or one which produced only funnel clouds on the same day, Crowe et al. (2012) examined this signature in three different severe weather events. They found that the separation between areas of enhanced Z_{DR} and K_{DP} was greater during tornadic periods in the tornadic storms examined, and that areas of enhanced Z_{DR} and K_{DP} overlapped more during nontornadic periods and in storms that never produced tornadoes. Tornadic storms in this sample also tended to be more likely to produce Z_{DR} values over 6 dB in their Z_{DR} arcs, although since the authors used C-band radar data in this study the implications of this finding for radar analysis using S-band WSR-88Ds are uncertain (Crowe et al. 2012). Martinaitis (2017) also found that a signature of horizontal separation between enhancements in Z_{DR} and K_{DP} was useful in differentiating between tornadic and nontornadic storms in convection associated with tropical cyclones in Florida when used in conjunction with analysis of the reflectivity and velocity fields for supercell signatures. Ongoing work by Jurewicz and Gitro (2018) is dedicated to determining how useful the separation between K_{DP} and Z_{DR} enhancements is in differentiating between tornadic and nontornadic supercells in a large sample of storms and working out ways to implement this signature in warning operations. Furthermore, Loeffler and Kumjian (2018) have developed a semi-automated algorithm to quantify the K_{DP}-Z_{DR} separation signature in tornadic nonsupercell storms. One parameter from this algorithm which was found to be particularly useful was the separation orientation (shown in figure 2.4) between a vector connecting the K_{DP} and Z_{DR} enhancement centroids and the storm motion vector. Separation orientations closer to 90 degrees found

to be associated with larger values of low-level SRH for a given separation vector length (Loeffler and Kumjian 2018). While Jurewicz and Gitro (2018) did not directly address the separation orientation, their diagrams using separation vectors, surface winds, and storm motion vectors to construct simple hodographs for the near-storm environment also suggest that larger angles between the separation and storm motion vectors should be correlated with higher SRH and low-level shear (figure 2.5). For brevity, separation orientation relative to storm motion will be referred to as the separation angle for the rest of this study.

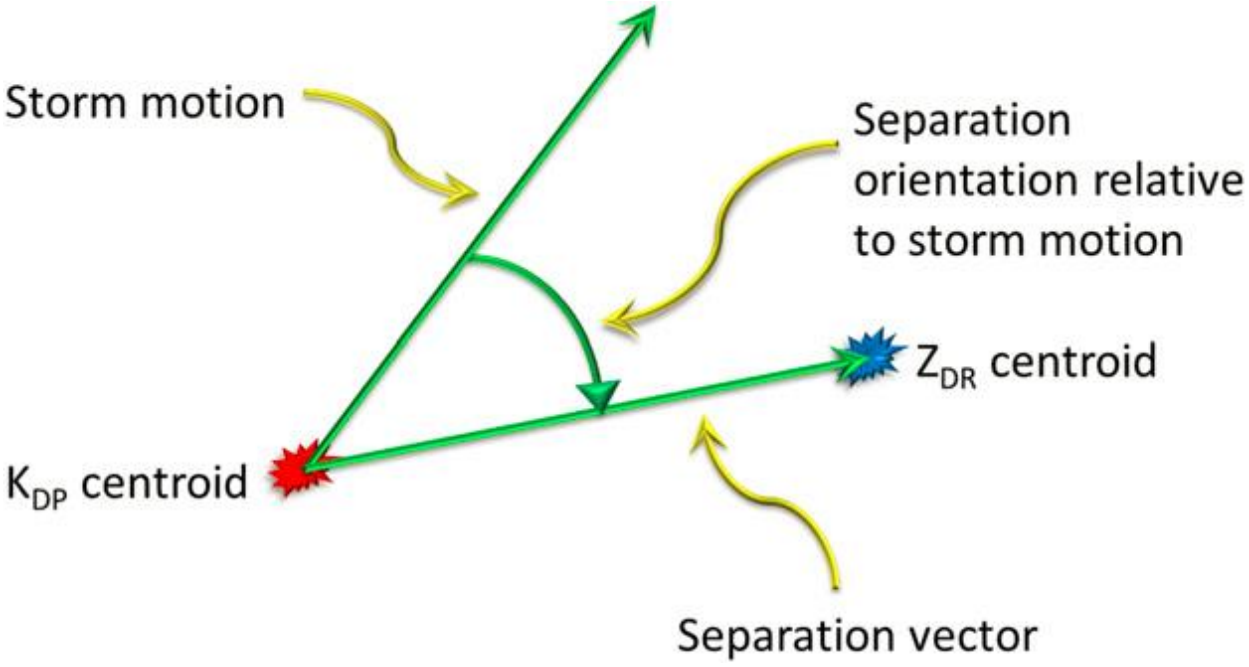

Figure 2.4 (Figure 4 from Loeffler and Kumjian (2018)): Plan view of the separation vector and separation angle in an idealized storm. The separation angle is here referred to by Loeffler and Kumjian (2018) as the separation orientation relative to storm motion.

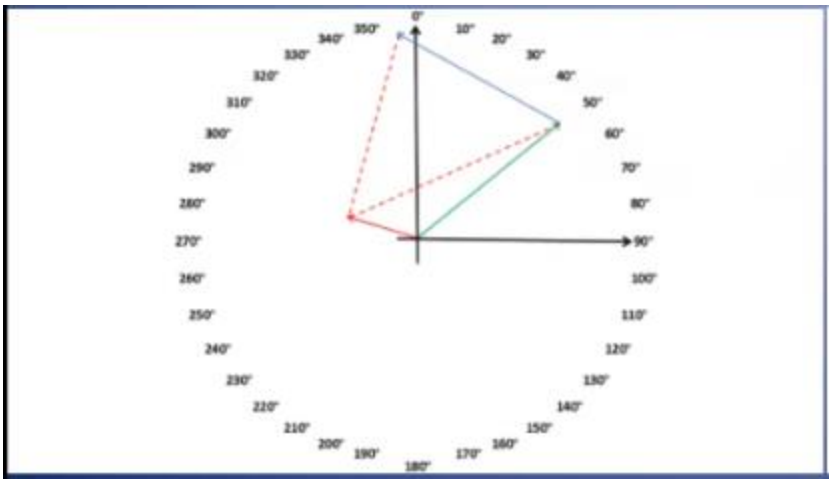

Figure 2.5: Diagram of SRH estimation using the storm motion vector (green arrow), separation vector (blue arrow) and the surface wind (red arrow). Near-storm SRH can be qualitatively assessed as the area bounded by the separation vector and the two dotted red lines (figure from Jurewicz and Gitro (2018)'s presentation).

Chapter III: Data and Methods

I. Supercell Dataset Development

In order to have a robust sample of supercells to use in the development of an automated Z_{DR} arc detection and tracking algorithm and to examine the variability of arcs in different environments, across supercell life cycles, and between tornadic and nontornadic storms, supercell cases were gathered from a number of sources. An initial dataset was compiled from the supercell cases used in VDB16, VDB17, and Heuscher (2016). This dataset contained 90 supercells, which had been selected by looking for storm reports within 125 km of a dual-pol WSR-88D and ensuring that the storm which produced the reports had a persistent mesocyclone and clearly evident supercell radar structures (Heuscher 2016, VDB17). These cases mainly originated from 2012 through 2014, so additional supercell cases were sought from 2014 to 2018. Keeping generally in line with the methodology of VDB17 and Heuscher (2016), possible supercell cases were identified by searching for linear segments of storm reports on the Storm Prediction Center archived maps of preliminary storm reports from the years in question (available at https://www.spc.noaa.gov/climo/reports/) and examining convective morphology using the radar composite archives on the UCAR Radar Archive (available at http://www2.mmm.ucar.edu/imagearchive/). Cases which appeared to contain one or more supercells were examined more closely with the Gibson Ridge GR2Analyst program using NEXRAD Level II data downloaded from the NEXRAD archive stored on Amazon Web Services (available at https://aws.amazon.com/public-datasets/nexrad/). Following the methodology of VDB16, storms were selected which consistently displayed typical supercell reflectivity structures such as hook or pendant echoes and

BWERs, dual-polarization supercell signatures such as Z_{DR} arcs and columns, and persistent midlevel mesocyclones. In order to have enough high-quality low-level data in the Z_{DR} arc region, each storm was required to have at least four 0.5 degree scans where the entire Z_{DR} arc was sampled by the radar at or below 1000 m above radar level (ARL). In addition, particular emphasis was placed on finding cases where most of the supercell's life cycle from convection initiation to tornadogenesis (or peak low-level rotation magnitude in nontornadic cases) included Z_{DR} arc data below 1000 m ARL. Adding these storms to the dataset from VDB16 and VDB17 and applying the requirement for four scans with good coverage of the Z_{DR} arc below 1000 m produced an initial dataset with 128 supercell storms. Further, more stringent criteria were applied to several smaller subsets of the supercell dataset and are discussed in later sections.

Environmental data were also gathered for each supercell, using proximity soundings from the National Center for Environmental Information (NCEI) archive of Rapid Refresh (RAP) model analyses. Starting with a database of environmental soundings from the RAP and Rapid Update Cycle (RUC) corresponding to the supercells used in VDB16 and VDB17, RAP soundings were obtained for each new supercell case from 2014-2019 from the RAP archive THREDDS server maintained by NCEI (https://www.ncei.noaa.gov/thredds/catalog/rap130anl/). Each sounding was required to be within 80 km of the supercell and had to be located on the same side of any mesoscale boundaries as the storm in question and away from the outflow of other storms to be considered representative of the supercell's inflow airmass. For cases which span multiple hours and have multiple possible proximity soundings, the sounding closest to the middle of the analysis period was used for that storm. Multiple thermodynamic and

kinematic variables and derived parameters were calculated for all soundings using the Sounding/Hodograph Analysis and Research Program in Python (SHARPpy, Blumberg et al. 2017) and Meteorological Python (MetPy, May et al. 2017) packages, and a list of these parameters is available in Table 1. Storm-relative helicity calculations (and the calculations for the derived parameters which include them) were performed twice: once with observed storm motions calculated from the tracking algorithm described in section III below, and once with sounding-derived storm motions using the Bunkers et al. (2014) technique.

Table 1: Variables collected from RAP environmental soundings for all supercells examined. Parameters were calculated using SHARPpy and MetPy.

Variable Type	Variable (units)
Thermodynamic	MLCAPE (J kg^{-1})
	MUCAPE (J kg^{-1})
	CIN (J kg^{-1})
	LCL Height (m)
	LFC Height (m)
	0 °C Height (m)
Moisture	1 km Relative Humidity (%)
	1-3 km Relative Humidity (%)
	3 km Relative Humidity (%)
	3-6 km Relative Humidity (%)
	6 km Relative Humidity (%)
	6-9 km Relative Humidity (%)
Kinematic	0-1 km Shear (m s^{-1})
	0-3 km Shear (m s^{-1})
	0-6 km Shear (m s^{-1})
	Effective Shear (m s^{-1})
	0-1 km Storm Relative Helicity (m^2s^{-2})
	0-3 km Storm Relative Helicity (m^2s^{-2})
	Effective Storm Relative Helicity (m^2s^{-2})
Derived Indices	Supercell Composite Parameter
	Significant Tornado Parameter
	Energy Helicity Index

II. Z_{DR} Calibration

To mitigate potential bias in the Z_{DR} data obtained for each case, scatterer-based Z_{DR} calibration was performed following the methodology used by Ryzhkov et al. 2005, Picca and Ryzhkov 2012, and Van Den Broeke and Van Den Broeke 2015. This calibration methodology makes use of the relatively consistent radar presentation of dry snow aggregates around 1.5 km above the environmental freezing level, which tend to have reflectivity values between 20 and 35 dBZ, CC values above 0.97-0.99, and Z_{DR} values between 0.1 and 0.2 dB (Ryzhkov et al. 2005, Picca and Ryzhkov 2012, Van Den Broeke and Van Den Broeke 2015). Thus, Z_{DR} calibration can be performed by searching for areas of dry snow aggregates 1.5 km above the environmental freezing level, calculating their average Z_{DR} value, and subtracting 0.2 dB to produce a calibration factor which can then be subtracted from the Z_{DR} field as a whole to calibrate it. To implement this process consistently across the entire supercell dataset, 15 minutes of data from the center of each case's analysis time was fed into a Python script which uses PyART (Helmus and Collis 2016) to extract Z_{DR}, CC, and reflectivity data from each scan, along with the height of each sample volume above radar level. Using the environmental freezing level obtained from each case's RAP/RUC proximity sounding, the average Z_{DR} was calculated for all radar pixels 500 m above and below a height 1500 m above the freezing level which had reflectivity between 20 and 35 dBZ and CC above 0.99. A reference Z_{DR} value for dry snow aggregates of 0.2 dB was then subtracted from this average Z_{DR} value, which produced a calibration factor which was subtracted from each case's Z_{DR} field to calibrate the data.

III. Algorithm Development

While recognizing a Z_{DR} arc is often intuitive for a human researcher or forecaster, programming a computer to identify the same signature as the human eye is no trivial matter. The first step is to precisely define what a Z_{DR} arc is. For the development of this algorithm, the definition of the Z_{DR} arc core in Van Den Broeke (2016) was used, with some simplifications, as the definition of the Z_{DR} arc. Thus, a Z_{DR} arc as defined for the algorithm is an area of Z_{DR} above 3.5 dB located on the inflow side of a storm. Next, radar data must be acquired and processed into a format which the Python modules which make up the algorithm can understand. This is done by using the nexradaws Python module (https://github.com/aarande/nexradaws) to download archived WSR-88D data from an archive Unidata maintains in partnership with Amazon (available at https://aws.amazon.com/public-datasets/nexrad/), and extracting and gridding the necessary radar variables (Z_{HH}, Z_{DR}, K_{DP}, and CC) from the lowest tilt of each scan (usually 0.5 degrees) onto a grid with a horizontal spacing of approximately 250 m using the Python ARM Radar Toolkit module (PyART, Helmus and Collis 2016). In order to identify the inflow side of the storm, the direction of the reflectivity gradient vector is calculated for all points where gridded reflectivity is greater than 20 dBZ, and the direction of a manually-defined vector perpendicular to the storm's forward flank and pointing into the core is subtracted from it (referred to as the forward flank downdraft (FFD) vector, figure 3.1a,b). The gridded Z_{DR} field is masked in areas where this difference is greater than 120 degrees, since these areas are likely not on the inflow side of the storm. Areas with CC values below 0.60 are also masked out in the Z_{DR} field, since these areas likely represent nonmeteorological scatterers and can create spurious Z_{DR} arc

identifications in the algorithm (Figure 3.1c,d). The Z_{DR} field is then contoured at 3.25 dB (reduced slightly from the 3.5 dB in the arc definition to account for smoothing-induced arc area loss as the data are gridded). The Shapely module (available at https://github.com/Toblerity/Shapely/tree/master/docs/) is used to split this contour into individual closed polygons. For each polygon, the polygon area, centroid, mean Z_{DR} value, maximum Z_{DR} value, mean reflectivity gradient value, mean reflectivity gradient direction relative to the FFD vector, mean CC, and mean reflectivity are calculated.

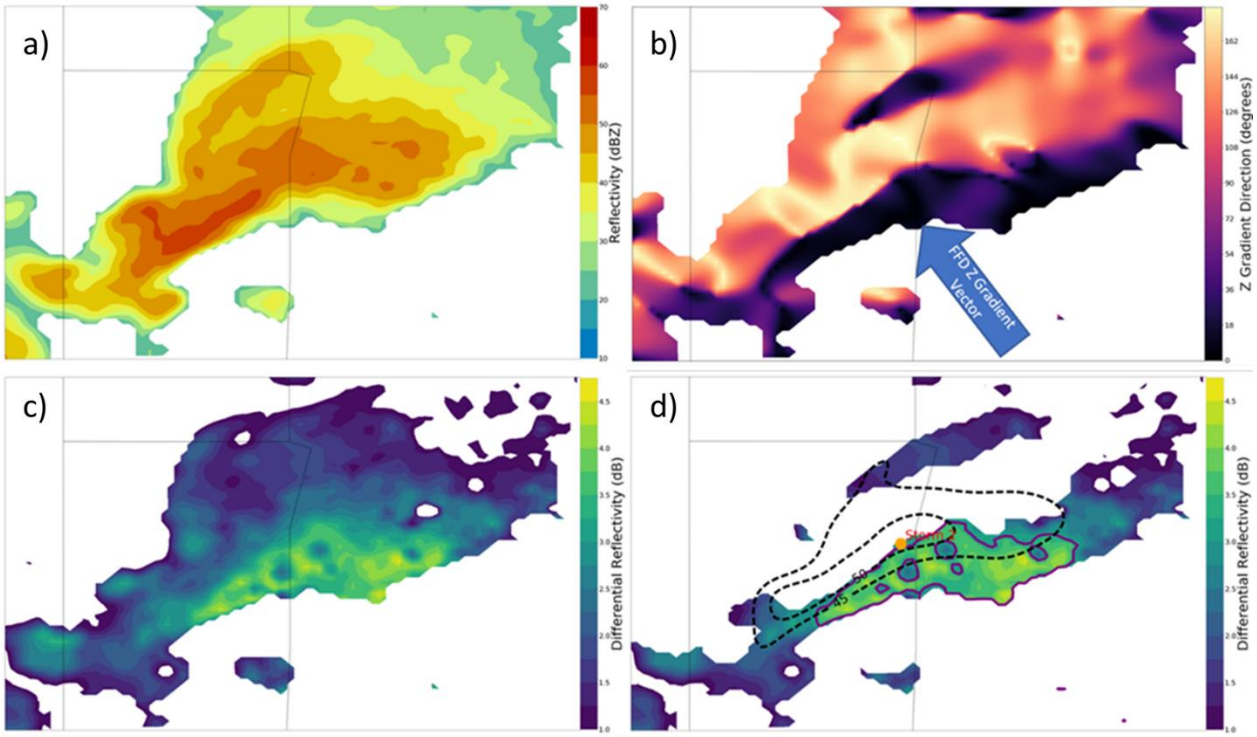

Figure 3.1: Inputs for the Z_{DR} arc algorithm, showing (a) gridded reflectivity, (b) the FFD gradient vector and reflectivity gradient direction relative to that vector, (c) the raw gridded Z_{DR} field and (d) Z_{DR} field with data masked where the Z gradient direction relative to the FFD gradient vector direction is > 120 deg and CC < 0.60, along with the 3.25 dB Z_{DR} contour (purple) and the associated storm object (dashed contours and orange dot) for reference.

Next, all Z_{DR} polygons identified in the previous step need to be associated with individual storms. To create storm objects to associate them with, the reflectivity field is smoothed and the 45 dBZ contour is plotted and split into polygons in a similar manner to the Z_{DR} fields. The algorithm plots the centroids of polygons with areas greater than 20 km^2 and saves them as storm objects which are tracked through subsequent radar scans.

To deal with the possibility of supercells embedded within larger convective structures, the algorithm plots a 50 dBZ contour inside any polygons with areas greater than 300 km^2 and uses the centroids of any polygon(s) derived from that contour as the storm objects within that polygon. Once storm objects are identified, Z_{DR} polygons are matched with the closest storm object to their centroid within a distance threshold of 30 km, and the distance and direction from the polygon to its corresponding storm object are saved for each polygon.

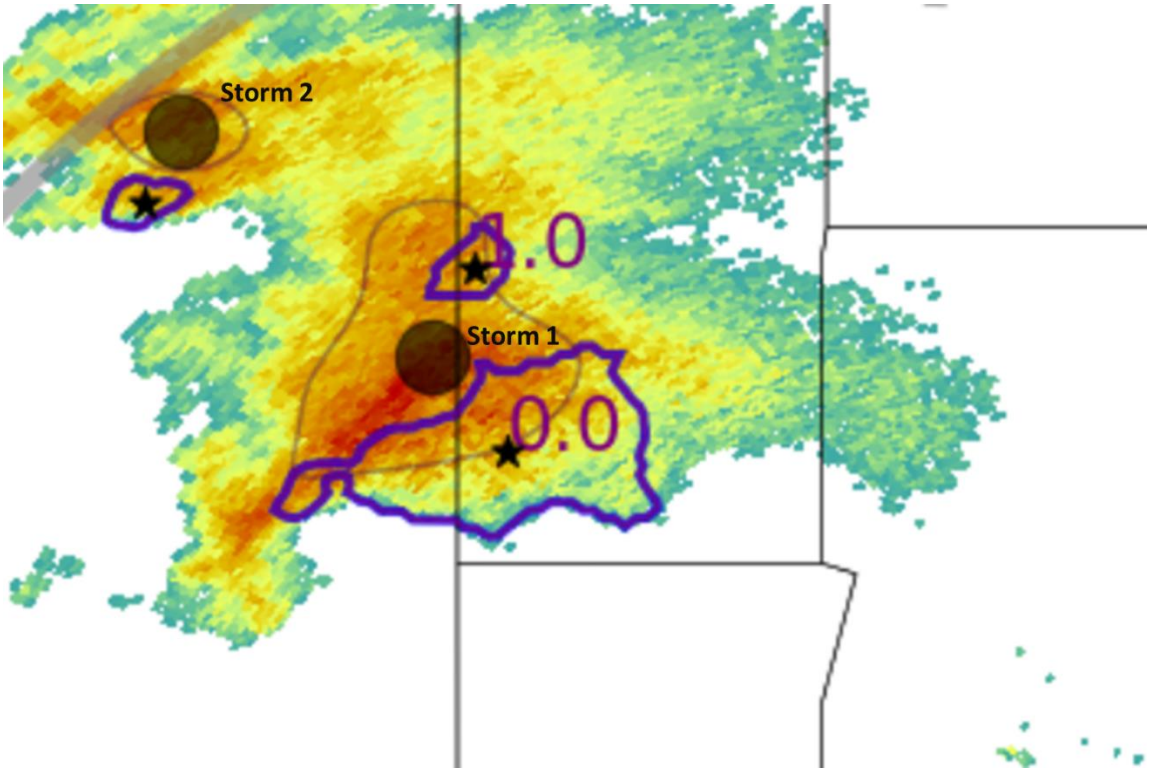

Figure 3.2: An example of a supercell (labelled as storm 1, with the storm centroid marked with a grey circle) with multiple Z_{DR} polygons (purple outlines/numbers, with centroids marked by small black stars) detected by the algorithm. In this case, object 0 is the arc, while object 1 is a spurious detection due to an area of high Z_{DR} in the northern part of the storm. Storm 2 is a nonsupercell storm object with a patch of high Z_{DR} (purple outline) associated with it.

At this point, a typical supercell with a Z_{DR} arc will often have multiple polygons associated with it, since it is not uncommon for a Z_{DR} arc to contain multiple non-contiguous regions of enhanced Z_{DR} interrupted by a hail signature or other areas of lower Z_{DR}. However, the algorithm frequently identifies polygons which represent areas

of enhanced Z_{DR} away from the inflow side of the storm's forward flank in areas such as the rear of the echo appendage, the northern or northwestern side of the precipitation shield, or with a small cell moving into the main supercell's inflow region. An example of a cell with a real and a spurious polygon is shown in Figure 3.2. Areas such as this are not part of the Z_{DR} arc, and thus a reliable method for removing these spurious polygons is needed. Random forest classifiers (Breiman 2001) are a type of machine learning algorithm which have shown promise working on classification problems like this one in meteorology, with recent work applying them to tasks as diverse as identifying and tracking mesoscale convective systems (MCSs) in regional reflectivity mosaics (Haberlie and Ashley 2018), improving the prediction of extreme precipitation events (Herman and Schumacher 2018), and forecasting the initiation of deep convection using satellite data and numerical model output (Mecikalski et al. 2015). Random forests work by training an ensemble of decision trees on manually labelled features (in this case, manually labelled arc and false detection objects) and a series of attributes of those features, with the goal being to use the attributes to accurately place the features in their manually labelled classes. Each decision tree starts by randomly picking one of the attributes and picking the attribute value which best splits the features into their correct classifications from a random subset of the attribute values. This is then repeated for several different attributes, creating a multi-level decision tree. The use of random subsets of the attributes to train each tree creates an ensemble of trees which produce slightly different outcomes. Since each tree by itself may not be an excellent classifier, the trees are combined into an ensemble to create a random forest, with the class indicated by the majority of the trees used as the output of the ensemble. The ensemble prediction produced by the random

forest tends to be much more accurate than what any individual decision tree could produce on its own (Geron 2017).

In order to create a random forest algorithm which can differentiate between actual arc objects and false detections, a large training dataset of manually labelled candidate polygons is needed. To create this dataset, 51 supercell cases from the supercell dataset used in VDB16 and VDB17 which had manual arc area time series available for comparison were run through an initial version of the Z_{DR} arc detection and tracking algorithm. This script outputs a spreadsheet of the saved characteristics for all polygons associated with each storm (listed in Table 2), as well as plots of radar reflectivity with each potential arc polygon plotted and numbered (as shown for one storm in figure 3.2). Using the reflectivity images, each polygon was manually classified as an arc polygon or non-arc polygon based on whether it was located along the inflow side of the forward flank of its associated supercell. From the 51 supercell cases examined, this resulted in 593 analysis times and 1,752 manually labelled polygons, split between 895 arc polygons and 857 false detections. To ensure that the random forest algorithm would work in differentiating between actual Z_{DR} arc objects and false detections in situations where it would be useful to define the Z_{DR} arc core with a value of Z_{DR} different than 3.5dB, the polygon mean Z_{DR} was not used as a predictor variable in the final random forest algorithm, and the polygon max Z_{DR} was normalized by each polygon's mean Z_{DR}.

Table 2: Variables saved for each arc object for use in the random forest algorithm.

Saved Arc Object Variables
Arc Area
Storm Centroid-Arc Object Centroid Distance
Mean Z_{DR} Value
Max Z_{DR} Value
Mean CC Value
Mean K_{DP} Value
Mean Z Value
Mean Z Gradient Relative to FFD Vector
Mean Z Gradient Value
Angle Between Storm Centroid-Arc Object Centroid Vector and FFD Vector
X-Component of Storm Centroid-Arc Object Centroid Vector
Y-Component of Storm Centroid-Arc Object Centroid Vector

Next, this training dataset was fed into a random forest classifier created in Python using the scikit-learn module (Pedregosa et al. 2011). This random forest classifier included 100 decision trees and used a 9:1 train-test split, meaning that 90% of the training dataset was randomly selected by scikit-learn to be set aside to train the random forest algorithm and the remaining 10% was used to test the performance of the resulting classifier. Since the partitioning of the dataset into training and testing samples is random, this can result in varying performance between different iterations of the random forest as it is trained and tested on different subsets of the data. Thus, an ensemble of 1000 different 100-tree random forest classifiers was created using the above process, and their accuracy was tested on both their particular training subset and the

entire training dataset. As seen in Figure 3.3, most of the individual algorithm iterations performed fairly well on their testing subsets, with probabilities of correctly identifying an arc object as an arc object ranging from 80% to 97% with a peak around 90%, and probabilities of incorrectly labelling a false detection as an arc generally ranging from below 5% to around 20% in a very small number of cases with a peak just under 10%. On the entire dataset, performance was even better, with probabilities of correct detection in the vast majority of iterations exceeding 98% and probabilities of false detection generally ranging between 5% and 15% (Figure 3.4).

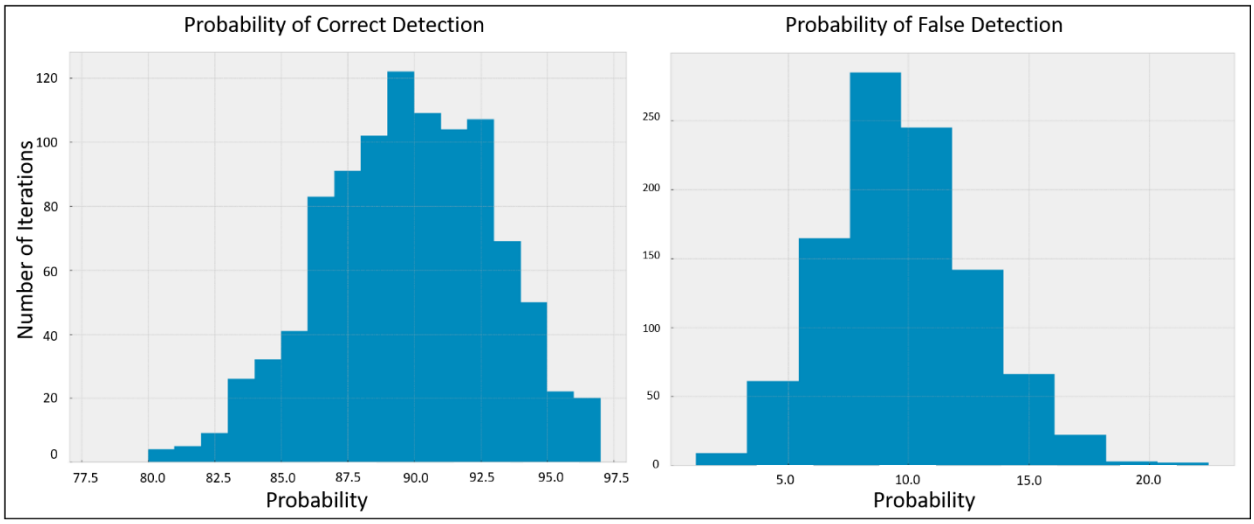

Figure 3.3: Histograms of random forest algorithm performance statistics on the test subset of the training dataset through 1000 algorithm iterations.

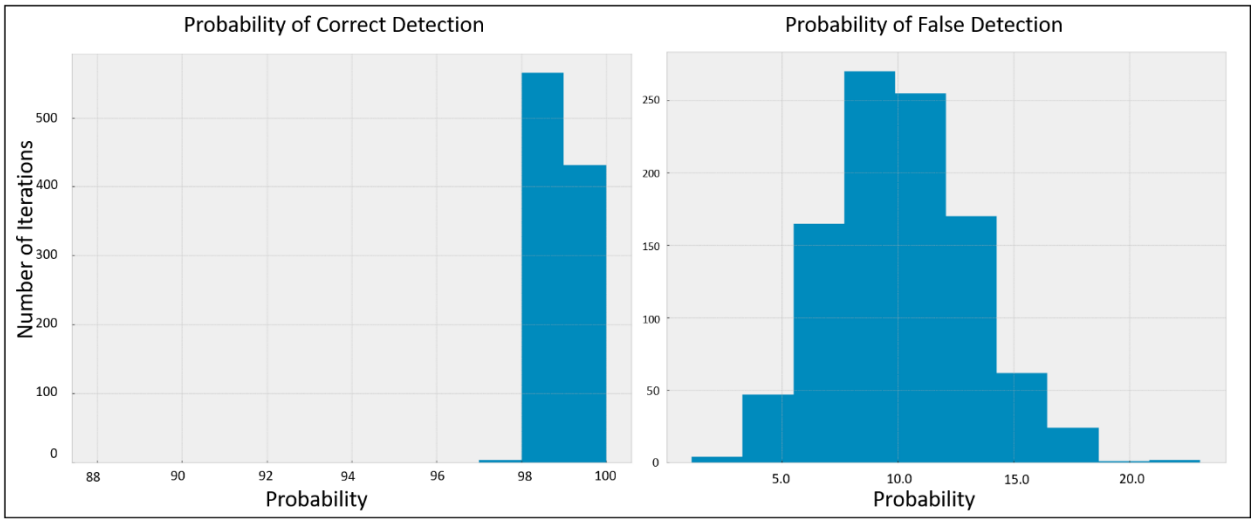

Figure 3.4: As in 3.3, but with algorithm performance statistics calculated using the entire training dataset.

From this ensemble of random forest classifiers, two iterations were identified with the highest probabilities of correct detection on the entire dataset of 99.88%. From these two classifiers, the one with the lower probability of false detection of 0.56% was added in to the Z_{DR} arc algorithm code to be used to remove spurious polygons from the arc detections. It is important to note that since the performance metrics shown above are for the entire dataset and thus include data that the classifier has already seen, its performance on unfamiliar data will likely be closer to the mean performance statistics (~90% probability of correct detection and ~10% probability of false detection) on the 10% testing samples shown earlier. However, since the 10% testing statistics are only calculated on a small portion of the dataset and thus may be unrepresentative of the algorithm's performance on a larger sample, the performance statistics on the full dataset were used despite the possibility that they may be somewhat inflated by the inclusion of the training sample, since they may be better at assessing the relative performance of

each algorithm iteration on the entire dataset. Once the random forest algorithm has removed any false arc detections for each storm, the remaining arc polygons are combined into a single arc object for each storm in each radar scan. Z_{DR} arc characteristics (listed in Table 3) are then calculated for each arc object and saved for each radar scan. This results in a Pandas dataframe containing time series of arc characteristics for each identified storm.

Table 3: List of arc characteristics calculated and saved by the algorithm.

Saved Z_{DR} Arc Characteristics
Mean Arc Z_{DR} Value (dB)
Max Arc Z_{DR} Value (dB)
Mean of 10 Max Z_{DR} Values in Arc (dB)
Arc Z_{DR} Value Standard Deviation
Mode of Arc Z_{DR} Values (dB)
Median Arc Z_{DR} Value (dB)
Z_{DR} Arc Area (km^2)

IV. Algorithm Verification

The final Z_{DR} arc detection and tracking algorithm was run on the 51 storms from the VDB16 and VDB17 dataset, and the arc areas output by the algorithm were compared to the manual arc areas for each storm. The results of this comparison are shown in figure 3.5. Overall, the algorithm performed fairly well, with a correlation of $r = 0.822$ between algorithm-calculated and manual arc areas (throughout this thesis, *r* values and *p* shown

for correlations are calculated using a Spearman's Rank-Order Correlation due to the non-Gaussian distribution of the Z_{DR} arc metrics). However, the algorithm struggled with some of the cases on the margins, overpredicting areal extents in many of the larger arcs and underpredicting smaller arc areas or failing to detect them entirely. Some of the mismatch between the algorithm and manual arc areas may be due to the inherent subjectivity of manual arc area calculations, especially in cases where the arc is small or ill-defined.

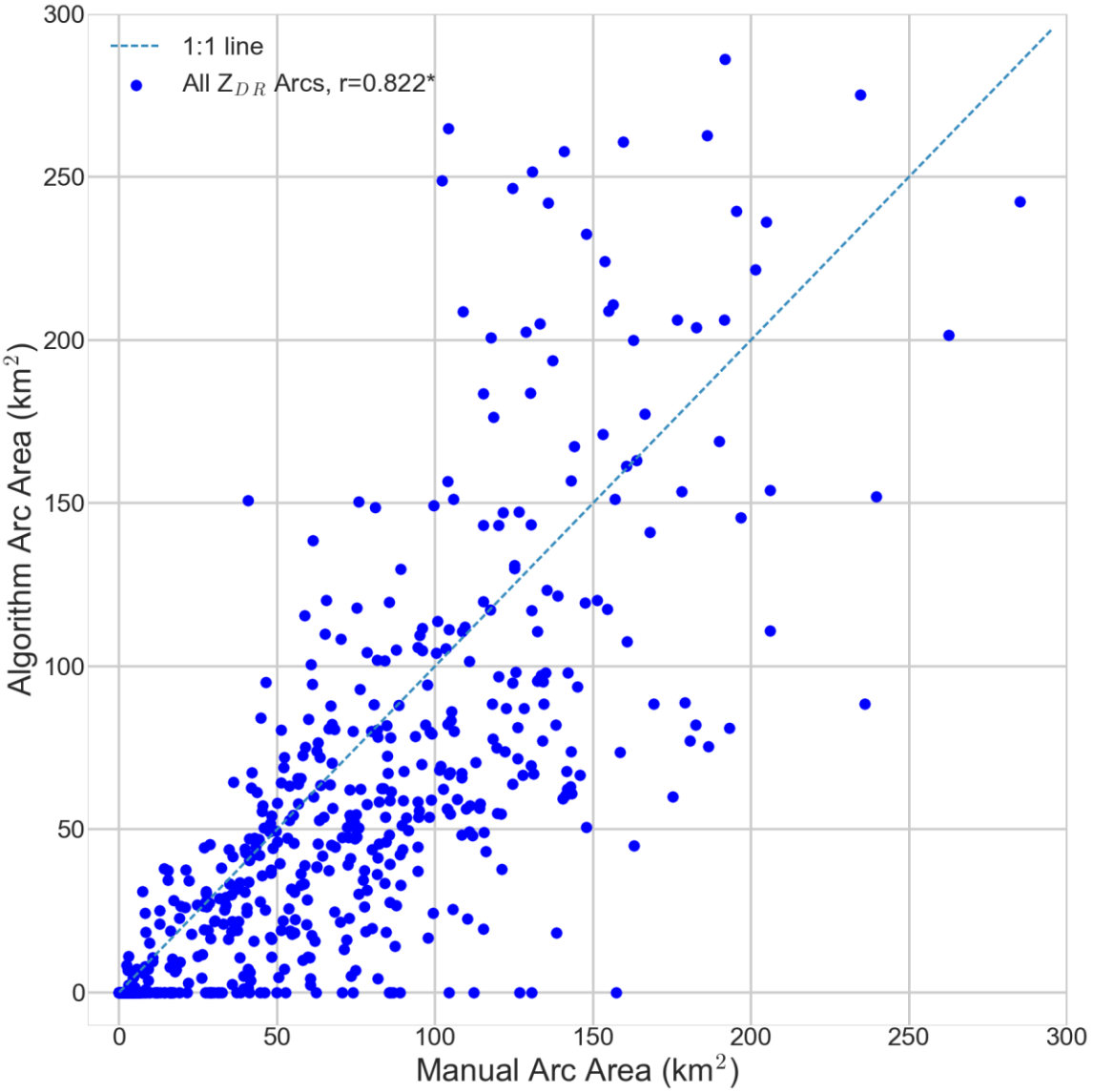

Fig. 3.5: Comparison between algorithm-derived and manual Z_{DR} arc areal extents. Dashed blue line is a 1:1 line along which a perfect match would fall.

To further explore the algorithm's performance, a detailed case study was conducted on WSR-88D data from the 30 March 2016 tornadic supercell near Tulsa, Oklahoma, which had a well-defined Z_{DR} arc for much of its lifetime. Manual arc areas

were calculated by analyzing Z_{DR} and reflectivity at horizontal polarization (Z_{HH}) data in QGIS (QGIS Development Team, 2018), and shapefiles of arc extent were saved for each radar scan from 2329 UTC 30 March to 0032 UTC 31 March 2016. A time series and scatterplot comparison of the manual and algorithm arc areas is shown in Figures 3.6b and c, and an animation of the arc outlines from the manual and algorithm analyses is shown in Figure 3.6a. Overall, the algorithm performed exceptionally well in this case, having a correlation of r = 0.94 between the manual and algorithm arc areas and capturing temporal changes in the manual arc area time series well. The animation of the manual and algorithm arc outlines shows that the algorithm struggled somewhat in the storm's early stages when the arc was smaller and more nebulous, but performed very well once the arc became large and clearly defined.

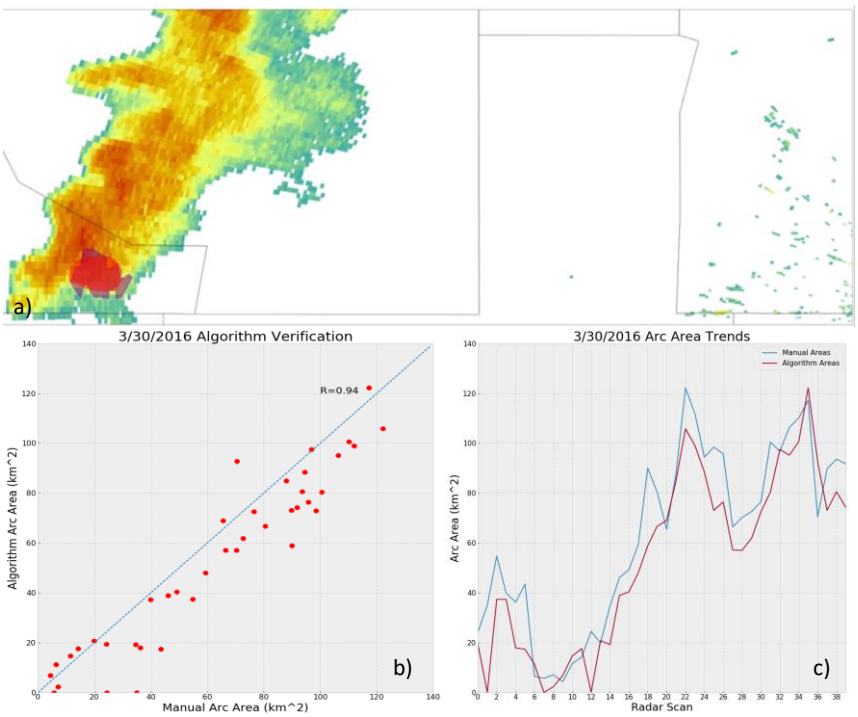

Figure 3.6: An in-depth comparison of manual and automated arc analyses from the 30 March 2016 tornadic supercell, featuring (a) an animation of algorithm (red) and manual (blue) arc outlines overlaid on base reflectivity data (double-click to play animation), (b) a scatterplot of manual and algorithm arc areas, and (c) time series of the manual and algorithm arc areas.

V. K_{DP}-Z_{DR} Separation Analysis

Since Loeffler and Kumjian (2018) identified the separation angle between the K_{DP}-Z_{DR} separation vector and the storm motion vector as potentially being useful in distinguishing tornadic and nontornadic storms, an attempt was made to include an objective version of this calculation in the algorithm. K_{DP} foot signatures were identified in a similar manner to how the initial Z_{DR} polygons were constructed. First, the K_{DP} field

was masked where reflectivity was below 35 dBZ and contoured at 1.5 degrees/km. This contour of K_{DP} was then broken into polygons using Shapely and polygons were assigned to the closest storm object within 15 km. Multiple polygons on a single storm were combined into a single K_{DP} foot object and the centroid of this object was then used as the final K_{DP} foot centroid. For storms with both a K_{DP} foot object and a Z_{DR} arc object, a separation vector was then calculated from the K_{DP} foot centroid to the Z_{DR} arc centroid. The separation angle was then calculated as the magnitude of the counterclockwise turning from the separation vector to the storm motion vector.

VI. Low-Level Rotation Analysis

Using the same subset of the supercell dataset used to train the Z_{DR} arc detection and tracking algorithm, low-level rotation time series were collected to test the hypothesis that changes in Z_{DR} arc characteristics may lead increases in low-level rotation. Two proxies for low-level rotation strength were calculated for each storm at all times with available Z_{DR} arc data using Gibson Ridge GR2 Analyst software: rotational velocity (V_r) and maximum Gibson Ridge Normalized Rotation (NROT). V_r was calculated as

1) $$(|\max V_{in}| + |\max V_{out})/2$$

for each supercell couplet following the methodology of Smith et al. (2012). Here, max V_{in} is the maximum inbound velocity in the rotational couplet, while max V_{out} is the couplet's maximum outbound velocity. Care was taken to avoid spurious couplets caused by vertical sidelobe contamination in the inflow notch or dealiasing errors. NROT is a derived product available in GR2 Analyst (version 20.19.15.4835 used) which identifies

areas of rotation in dealiased base velocity data in a similar manner to the Multi-Radar Multi-Sensor (MRMS) rotation track product. For SuperRes data, NROT is found taking a 9 by 9 box of pixels and calculating the azimuthal gradient of velocity. That azimuthal gradient is then divided by a factor related to the distance from the radar to remove the effect of beam broadening with range. According to the NROT documentation, NROT values above 1.0 are intended to be "significant" (Cooper and Vorst 2016, Gibson 2017). A similar quality control procedure was followed in calculating the max NROT time series as in the max V_r time series, avoiding signatures which may have been the result of improper dealiasing or sidelobe contamination in the inflow region. Algorithm-derived time series of Z_{DR} arc characteristics were then obtained for all of these storms and are compared to the low-level rotation time series in section 2 of chapter 4.

VII. Tornadogenesis and Tornadogenesis Failure Analysis

A smaller subset of storms was selected from the larger supercell dataset to examine whether repeatable trends in Z_{DR} arc characteristics existed prior to tornadogenesis and whether these trends differed from arc behavior prior to tornadogenesis failure. For the additions to the supercell dataset from 2014-2018, tornadogenesis times for each tornadic storm and confirmation that nontornadic storms did not produce any (reported) tornadoes were obtained from NCEI Storm Data (https://www.ncdc.noaa.gov/stormevents/). To be included in this analysis subset, tornadic supercells had to produce a tornado during the analysis period, and at least 10 0.5 degree scans prior to tornadogenesis had to be available with the entire Z_{DR} arc sampled below 1 km ARL. Nontornadic storms needed to have a clear peak in low-level rotation (measured as a value of Gibson Ridge 2 Normalized Rotation (NROT) above

0.50 co-located with a clearly evident velocity couplet) and at least 10 0.5 degree scans including the entire Z_{DR} arc below 1 km ARL prior to this NROT peak. For the nontornadic storms, this low-level rotation maximum is considered to represent tornadogenesis failure, as in Markowski et al. (2002). All storms in this subset were also required to have data from a radar operating in Supplemental Adaptive Intra-Level Low-Level Scans (SAILS, https://www.weather.gov/news/151509-meso-sails) mode to provide high-frequency sampling of the Z_{DR} arc at ~two to three-minute intervals. These criteria narrowed this subset down to 22 tornadic supercells and 10 nontornadic storms. Algorithm-calculated Z_{DR} arc characteristics were obtained for the 10 scans leading up to tornadogenesis or tornadogenesis failure for these storms and are analyzed in section 3 of chapter 4.

VIII. Mesocyclone Cycling Analysis

As previous case studies have observed that Z_{DR} arcs can show a repeatable pattern of strengthening and expanding in the lead-up to low-level mesocyclone occlusion and weakening during and after occlusion (Kumjian et al. 2010; Palmer at al. 2011), a final subset of strongly cyclic storms was selected to examine whether this behavior holds in a somewhat larger sample of supercells. Supercells in this subset had to have hook echo evolutions in radar reflectivity that clearly followed the occlusion conceptual model presented by Beck et al. (2006) as shown in Figure 3.7 to ensure that all cases were sampling an occlusion cycle. Each case had to have at least one full occlusion cycle where the entire Z_{DR} arc and low-level mesocyclone were sampled by the radar at or below 1 km ARL to ensure high-quality observations of arc evolution. These criteria yielded a sample of eight cyclic supercells, with five being tornadic and three

being nontornadic. For each of these supercells, the progress of cyclic mesocyclogenesis was examined for all radar scans for which quality data below 1 km in the arc were available. Each scan was labelled from 1 to 3 for the stage of the Beck et al. (2006) occlusion conceptual model that the storm's reflectivity and velocity structure most closely resembled. Since stage 4 of the Beck conceptual model corresponds to the supercell beginning another cycle in a similar state to stage 1, scans which resembled stage 4 were classified as stage 1. An example of how the Beck et al. (2006) stages were identified in actual WSR-88D data is shown in Figure 3.8. Changes in Z_{DR} characteristics over occlusion cycles in each storm are then analyzed in section 3 of chapter 4.

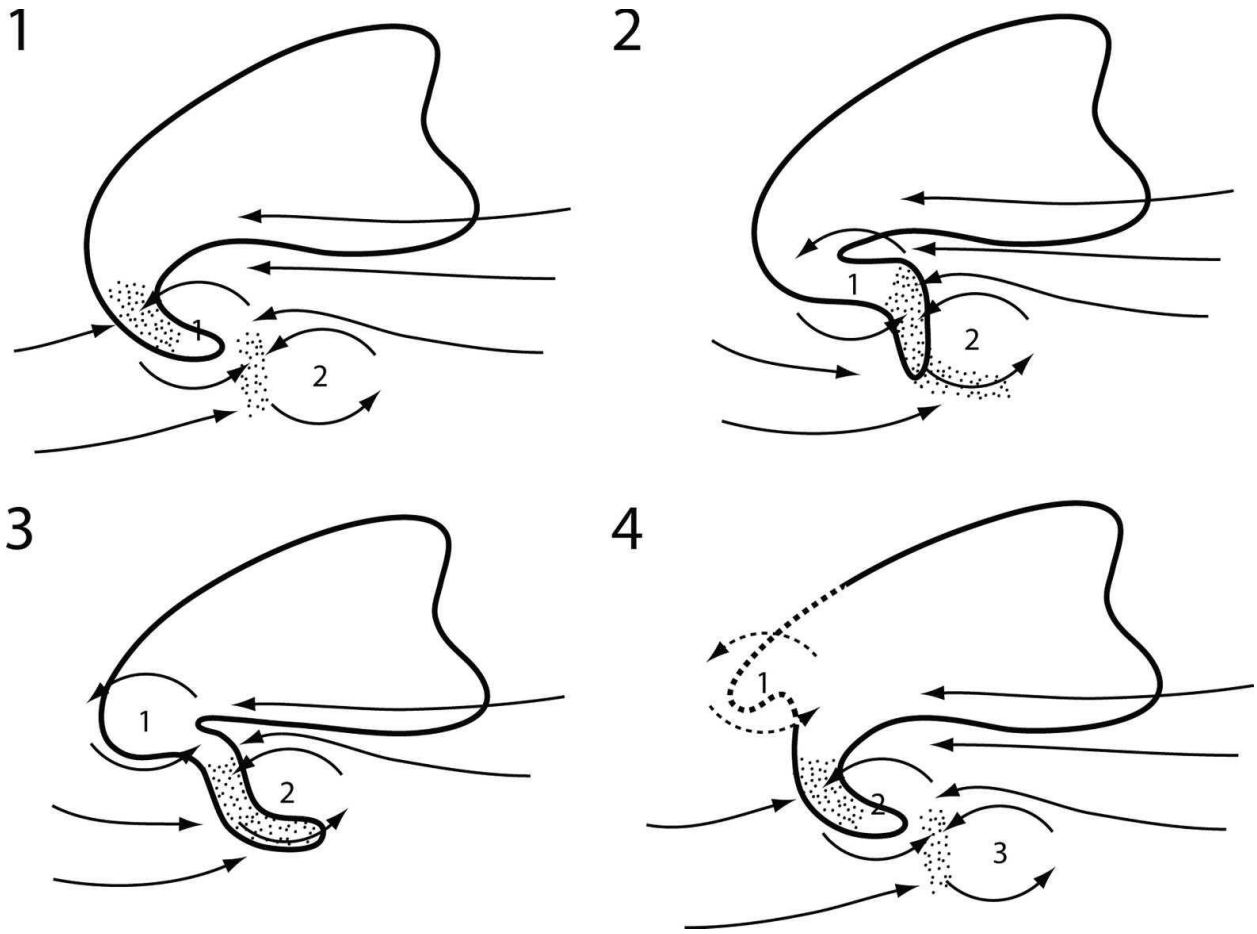

Figure 3.7: Beck et al. (2006)'s Figure 15, showing their conceptual model of hook echo reflectivity evolution during cyclic mesocyclogenesis. Mesocyclones are numbered 1 through 3, the dark line is the edge of the supercell's reflectivity echo, and stippling represents areas of deformation.

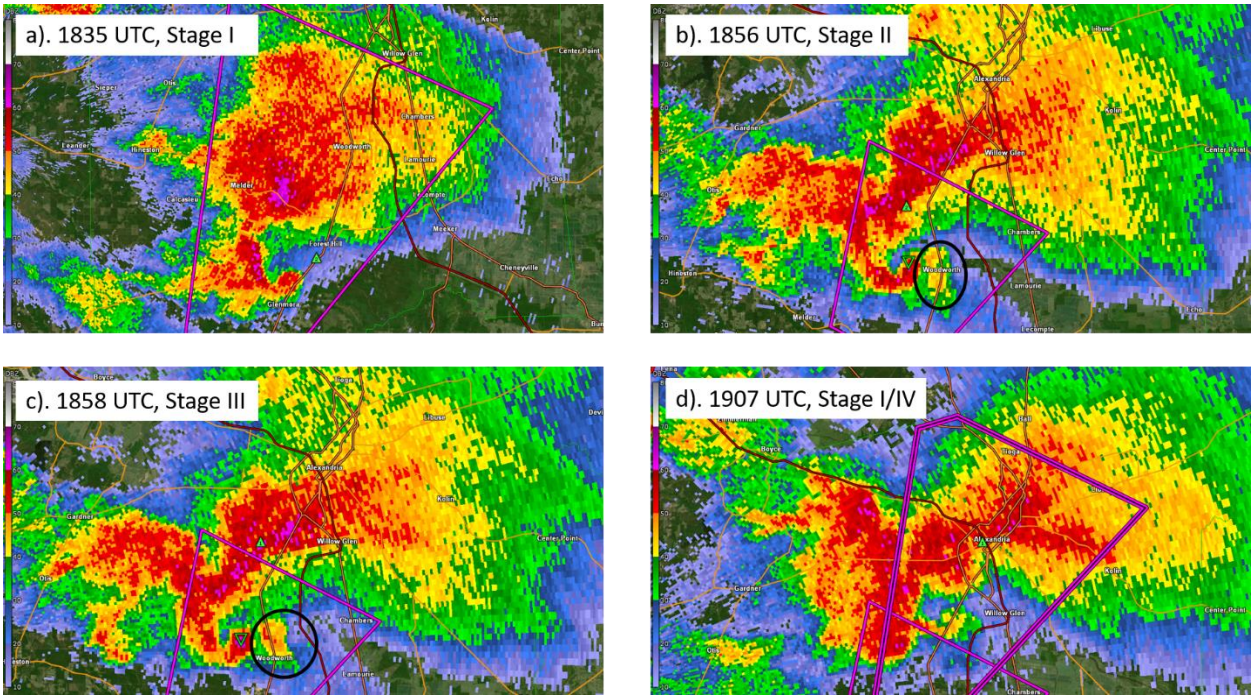

Figure 3.8: Example of Beck et al. (2006) cycling stages manually identified in WSR-88D radar data for a tornadic supercell near Alexandria, LA on 2 April 2017. The black ovals on stages II and III outline the developing appendage forming around the new mesocyclone. Stage III was identified relatively infrequently, with the main difference between it and stage II being the slight cyclonic curvature of the developing hook echo.

Chapter IV: Results

I. Z_{DR} Arc Characteristics and Environmental Variability

From the initial dataset of 128 supercells and their associated proximity soundings, 7 were removed due to poor algorithm performance which resulted in calculated arc metrics which were not representative of the storm's actual Z_{DR} arc characteristics. Cases were considered to have poor algorithm performance when three or more scans had one of three issues: large areas of a storm's rear flank region incorrectly classified as part of the arc, high Z_{DR} associated with a neighboring storm included in the arc, or a Z_{DR} arc that was clearly misclassified by the random forest algorithm. Examples of all three of these failure modes are shown in Figure 4.1. Removing these cases resulted in a dataset of 121 supercells and proximity soundings. The calculated average Z_{DR} arc metrics for each storm (arc areal extent, mean Z_{DR} value in the arc, and mean of the 10 maximum Z_{DR} values in the arc) were then plotted against the environmental parameters (listed in Table 1) for each storm. In calculating the average for each arc metric, radar scans where no arc was detected had their arc areal extent, mean Z_{DR} value and mean of the 10 maximum Z_{DR} values were set to NaN. For use in the environmental comparisons, each case was also required to have at least 15 minutes of data (working out to approximately 3 non-SAILS radar scans or 5-7 SAILS scans) where an algorithm-detected arc was present, with less than 45 minutes between non-consecutive arc detections. This reduced overall the sample size to 109 storms from 121, with 69 tornadic supercells and 40 nontornadic supercells. The major results of these environmental comparisons are summarized in this section. The value and statistical significance of the

correlations between all three arc metrics and all variables from Table 1 are summarized in Table 4.

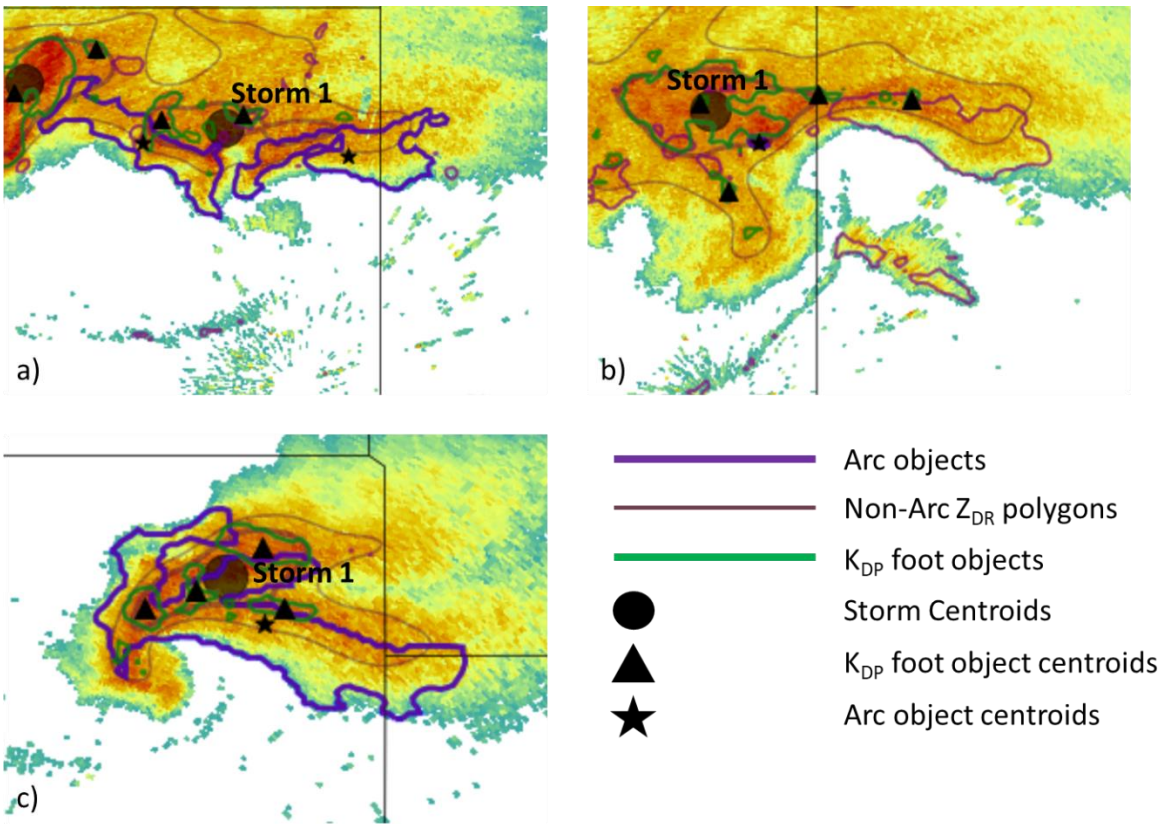

Figure 4.1: Examples of Z_{DR} arc algorithm failure cases. In all cases, the supercell of interest is labelled as storm 1. In a), an actual Z_{DR} arc is incorrectly combined with a separate area of high Z_{DR} from a trailing storm. In b), a well-defined arc is misclassified by the random forest. In c), an area of high Z_{DR} in the storm's rear flank which is contiguous with the arc is erroneously included in the final arc object.

A. MLCAPE and MUCAPE

Previous work by VDB16 examining supercell dual-polarization characteristics in 12 different environments found that Z_{DR} arc width and areal extent tended to increase with greater MUCAPE. This was attributed to the stronger updrafts produced in higher-

CAPE environments and the higher supersaturations inside those updrafts, which would result in drop-size distributions containing more large drops that would help produce higher Z_{DR} in the arc region (VDB16). In this study, Z_{DR} arc areal extent was also found to generally increase with increasing MLCAPE and MUCAPE (Figure 4.2, only MLCAPE shown since MLCAPE and MUCAPE are highly correlated in this dataset (r = 0.945)). Although the relationships between MLCAPE, MUCAPE, and arc areal extent were the strongest of any environmental variable-arc metric pairs examined, the correlations for both were only moderate (r=0.449 for MLCAPE and r= 0.487 for MUCAPE), and the plots of arc areal extent against both variables showed a fair amount of scatter. The increasing trend in Z_{DR} arc areal extent with increasing instability matches the results of VDB16, although the 109-storm dataset examined here contains 10 of the 12 storms from VDB16, so the samples are not entirely independent. Correlations between the arc intensity metrics (mean Z_{DR} value in the arc and mean of the top 10 Z_{DR} values in the arc) and instability were much smaller than those between areal extent and instability, although those for the mean of the top 10 arc Z_{DR} values still displayed significance at $p < 0.05$ (Figure 4.3, only MLCAPE shown).

Table 4: Spearman's correlations and their significance for all variables from Table 1.

Variable (units)	Area *r* (*p*)	Mean *r* (*p*)	10 Max *r* (*p*)
MLCAPE	0.449 (9.8×10^{-7})*	0.165 (0.08)	0.227 (0.02)*
MUCAPE	0.487 (7.6×10^{-8})*	0.184 (0.06)	0.255 (7.4×10^{-3})*
CIN	-0.286 (2.5×10^{-3})*	-0.196 (0.04)*	-0.233 (0.01)*
LCL Height	0.347 (2.2×10^{-4})*	0.336 (3.5×10^{-4})*	0.363 (1.0×10^{-4})*
LFC Height	0.276 (3.8×10^{-3})*	0.251 (8.7×10^{-3})*	0.291 (2.3×10^{-3})*
0 °C Height	0.215 (0.02)*	-0.119 (0.22)	-0.087 (0.37)
1 km Relative Humidity	-0.317 (7.8×10^{-4})*	-0.358 (1.3×10^{-4})*	-0.373 (6.4×10^{-5})*
1-3 km Relative Humidity	-0.274 (4.2×10^{-3})*	-0.257 (7.3×10^{-3})*	-0.264 (0.01)*
3 km Relative Humidity	-0.221 (0.02)*	-0.169 (0.08)	-0.189 (0.05)*
3-6 km Relative Humidity	-0.187 (0.05)	-0.119 (0.22)	-0.174 (0.07)
6 km Relative Humidity	-0.218 (0.02)*	-0.092 (0.34)	-0.134 (0.17)
6-9 km Relative Humidity	-0.279 (3.5×10^{-3})*	-0.113 (0.24)	0.141 (0.15)
0-1 km Shear	-0.252 (8.3×10^{-3})*	-0.248 (9.2×10^{-3})*	-0.242 (0.01)*
0-3 km Shear	-0.236 (0.01)*	-0.084 (0.38)	-0.136 (0.16)
0-6 km Shear	-0.062 (0.52)	0.125 (0.19)	0.075 (0.44)
Effective Shear	0.017 (0.86)	0.175 (0.07)	0.122 (0.21)
0-1 km Storm Relative Helicity	-0.149 (0.12)	-0.217 (0.02)*	-0.188 (0.05)
0-3 km Storm Relative Helicity	-0.127 (0.19)	-0.218 (0.02)*	-0.173 (0.07)
Effective Storm Relative Helicity	-0.077 (0.43)	-0.167 (0.08)	-0.130 (0.18)
Supercell Composite	0.316 (8.1×10^{-4})*	0.040 (0.68)	0.123 (0.20)
Significant Tornado Parameter	0.101 (0.30)	-0.02 (0.77)	0.022 (0.82)
Energy Helicity Index	0.257 (6.9×10^{-3})*	0.155 (0.11)	0.176 (0.07)

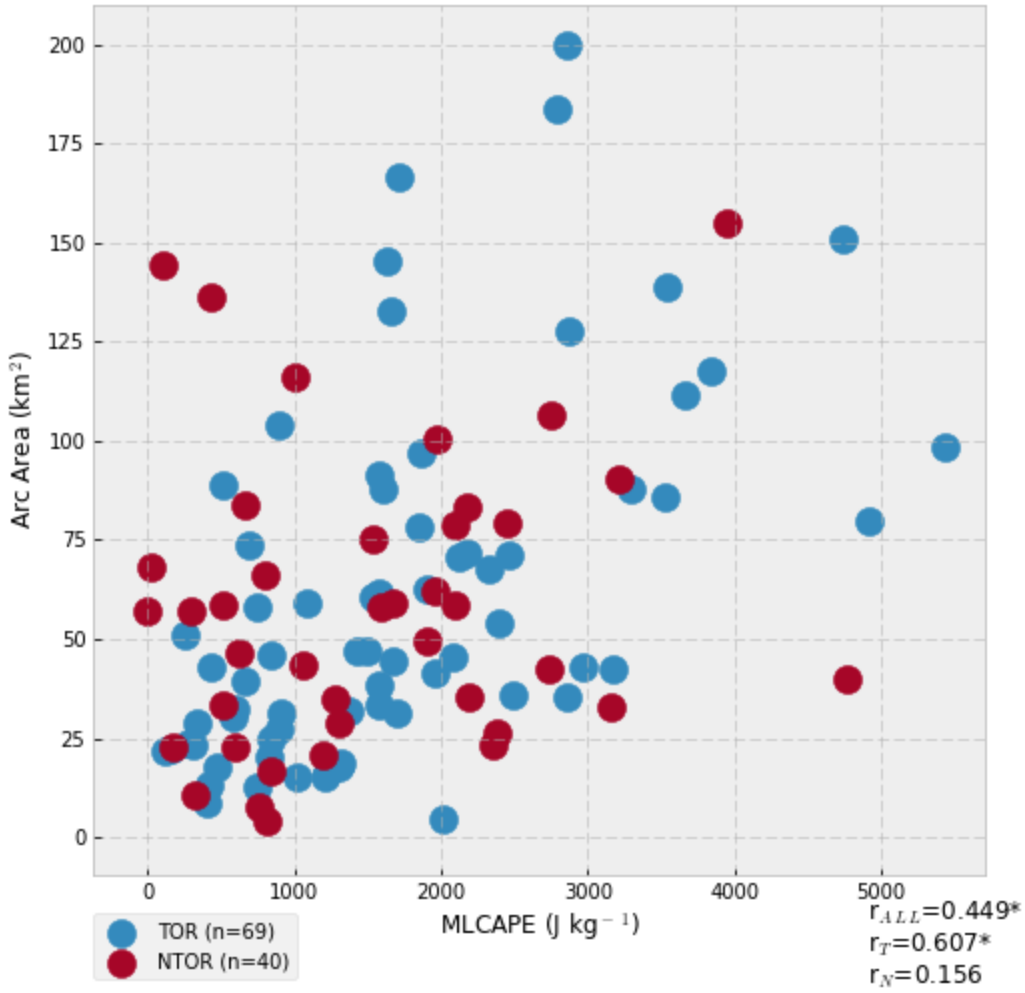

Figure 4.2: Scatter plot of Z_{DR} arc areal extent and MLCAPE. Tornadic storms are plotted in blue and nontornadic storms in red, and correlations (bottom right) are statistically significant at $p < 0.05$ if followed by an asterisk.

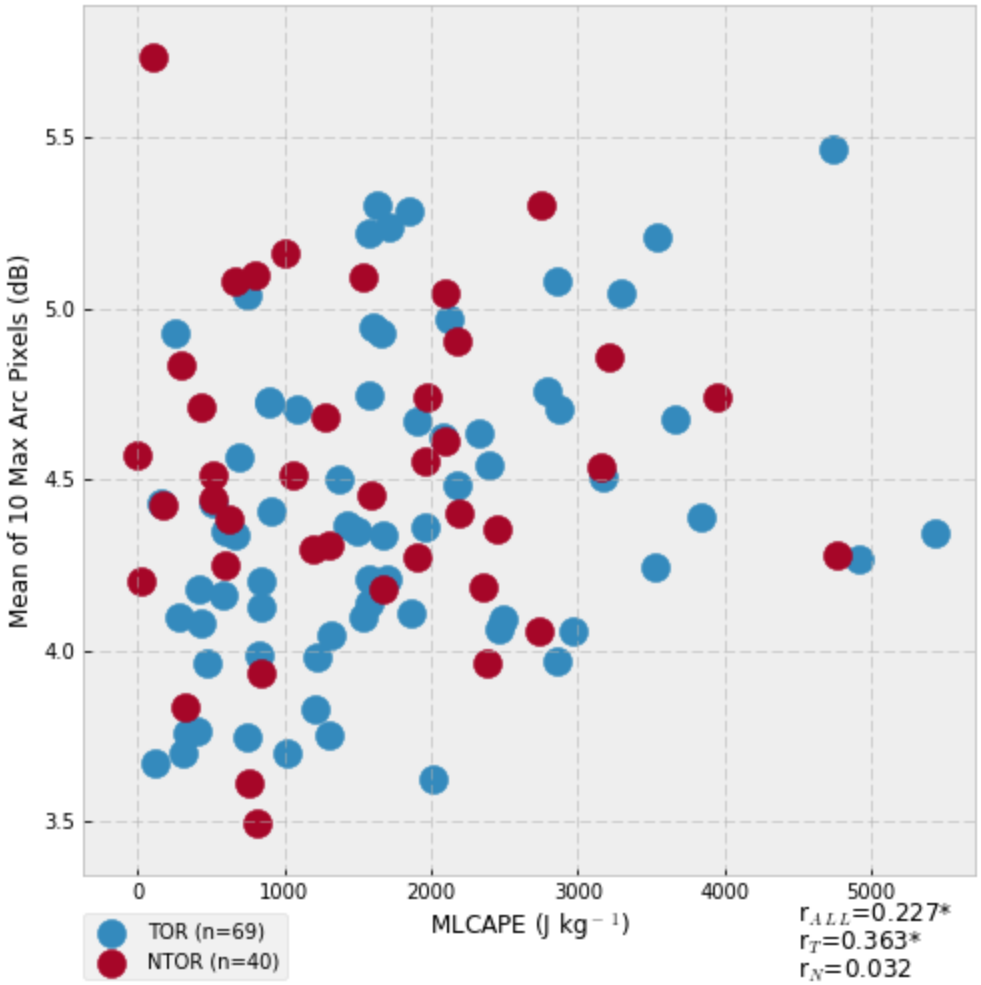

Figure 4.3: Scatter plot of the mean of the 10 highest arc Z_{DR} pixels and MLCAPE. Tornadic storms are plotted in blue and nontornadic storms in red, and correlations (bottom right) are statistically significant at $p < 0.05$ if followed by an asterisk.

B. Mid- and Low-Level Moisture

Previous work by Kumjian and Ryzhkov (2008b) hypothesized that observations of areas of higher Z_{DR} in nontornadic supercell hook echoes could be due to lower mid-

and low-level RH, which could lead to the preferential evaporation of smaller drops and help to shift the drop-size distribution in the arc toward larger drops to produce higher Z_{DR} values. This same process may make it easier for drop-size sorting by the storm-relative wind to produce larger areas of higher Z_{DR} values in the arc region, since the drop-size distribution falling into the sorting layer above the arc would be losing small drops through evaporation as well as advection toward the storm core by the storm-relative wind. In the current study, mid- and low-level moisture parameters generally displayed weak to moderate inverse correlations with Z_{DR} arc size and intensity. Arc areal extent displayed weak to moderate statistically significant correlations with all moisture parameters examined except for 3-6 km RH, with the strongest correlation found with 1 km AGL RH (r = -0.317, figure 4.4). The arc intensity metrics were a bit better correlated with moisture variables overall, with the strongest correlations for both also being with 1 km AGL RH (r= -0.358 for the mean arc Z_{DR} value and r= -0.373 for the mean of the 10 max arc pixels, figures 4.5 and 4.6). These results generally support the hypothesis that environments with low mid- to low-level RH can help enhance Z_{DR} arc size and intensity by encouraging the evaporation of small drops.

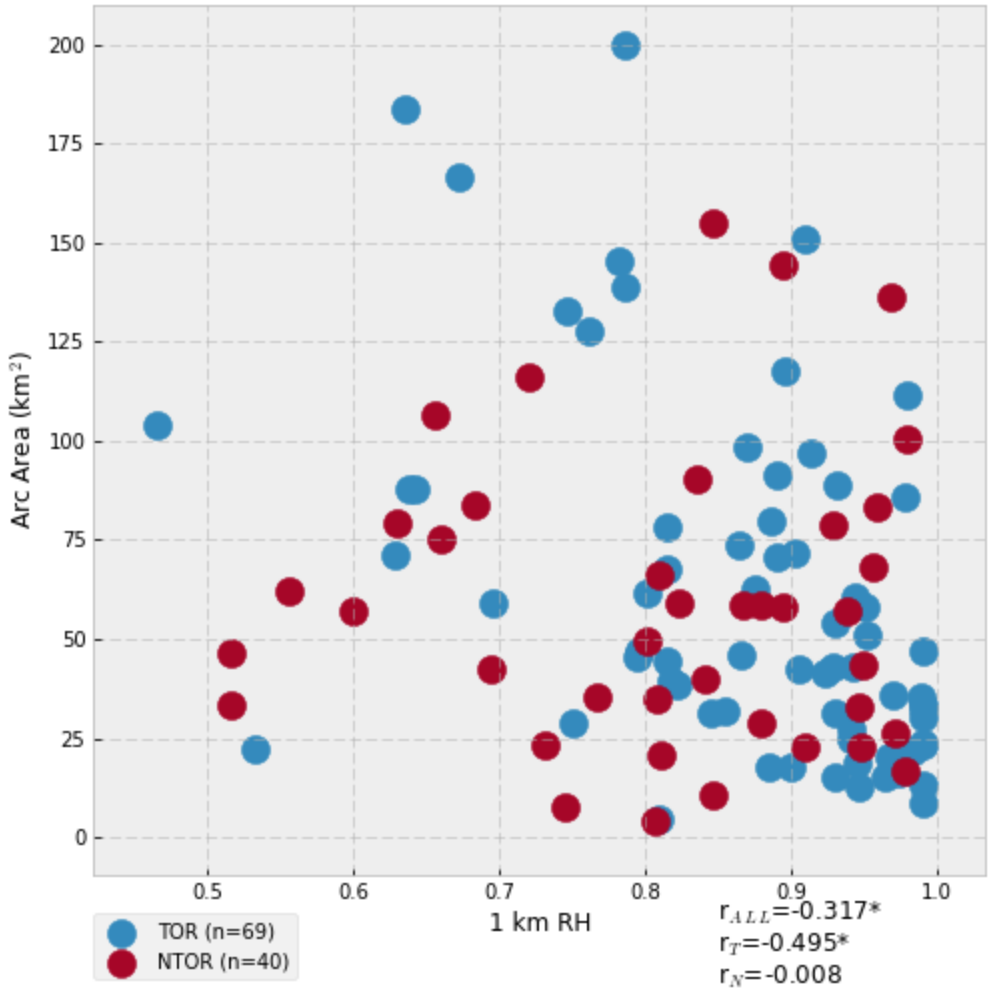

Figure 4.4: Scatter plot of arc area and 1 km AGL RH. Tornadic storms are plotted in blue and nontornadic storms in red, and correlations (bottom right) are statistically significant at $p < 0.05$ if followed by an asterisk.

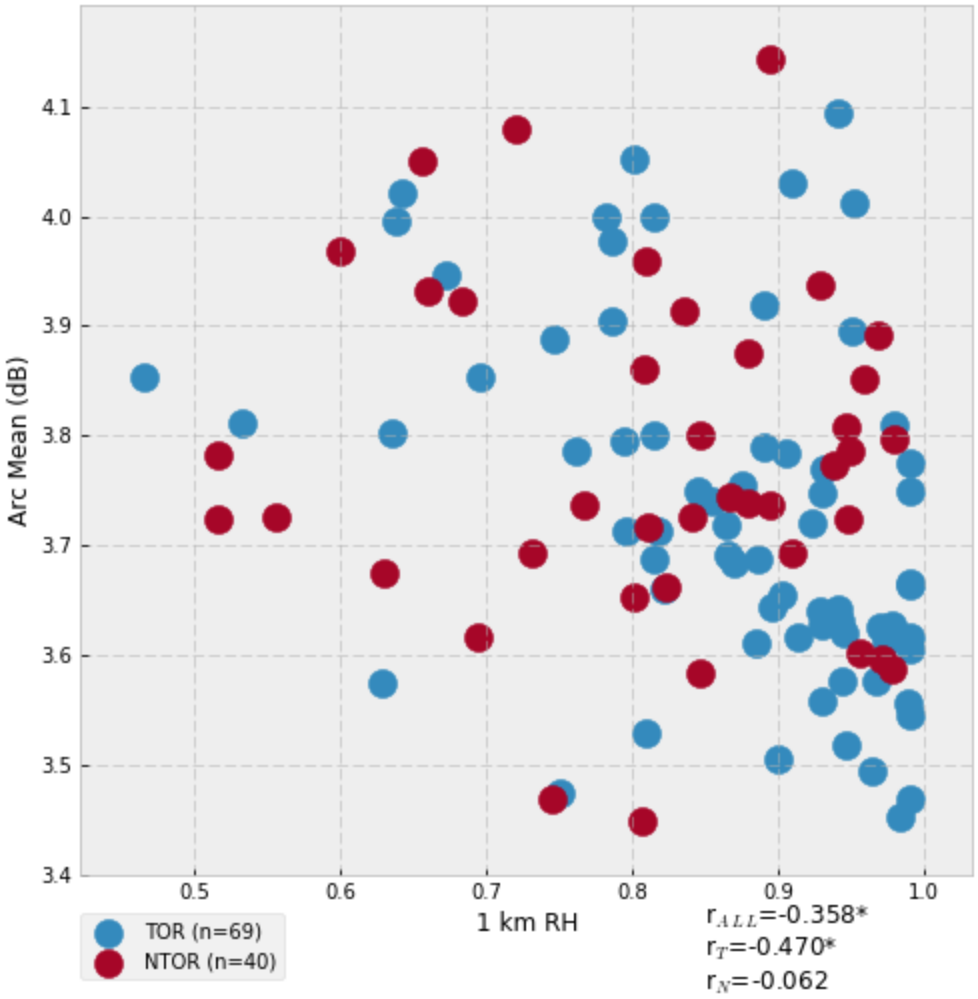

Figure 4.5: Scatter plot of mean arc Z_{DR} value and 1 km AGL RH. Tornadic storms are plotted in blue and nontornadic storms in red, and correlations (bottom right) are statistically significant at $p < 0.05$ if followed by an asterisk.

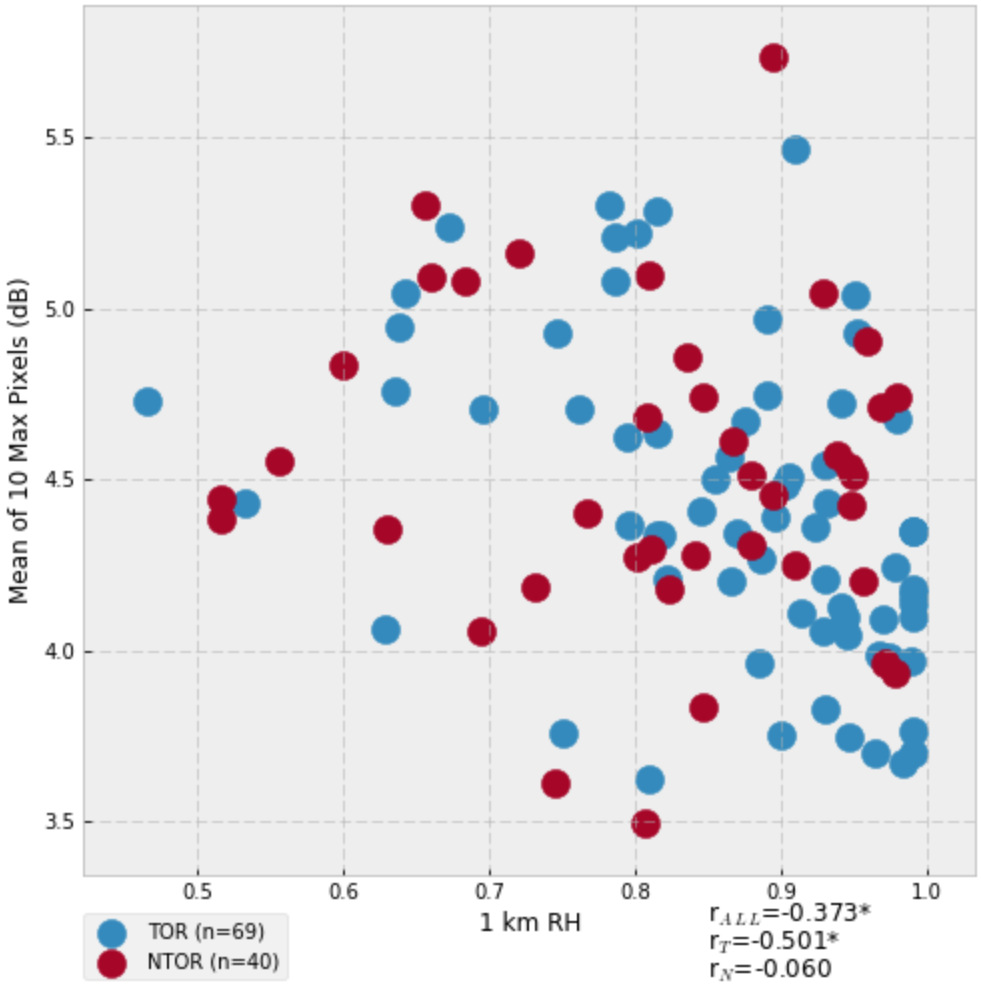

Figure 4.6: Scatter plot of the mean of the 10 max arc Z_{DR} values and 1 km AGL RH. Tornadic storms are plotted in blue and nontornadic storms in red, and correlations (bottom right) are statistically significant at $p < 0.05$ if followed by an asterisk.

C. MLLCL and MLLFC

Previous work by VDB16 suggested that higher mixed-layer lifted condensation level (MLLCL) heights and MLLFC heights (calculated here using a 100-mb mixed layer) are correlated with larger, more intense Z_{DR} arcs. VDB16 posits that this is due to precipitation forming at a higher elevation than in environments with lower MLLCLs and MLLFCs, giving the size sorting process a deeper layer and more time over which to act (VDB16). Furthermore, a higher altitude of precipitation formation and higher MLLCL heights could indicate that evaporation has more time to assist in removing the small drops from the drop size distribution and that subcloud evaporation may be contributing to this process in cases with higher MLLCLs. In the current study, MLLCL height was found to have weak to moderate significant correlations with arc areal extent and both arc intensity metrics, with *r* ranging from 0.336 to 0.363 (figures 4.7, 4.8, and 4.9). These correlations were much stronger for the tornadic part of the dataset than the nontornadic part. Meanwhile, correlations between arc metrics and MLLFC height were weaker overall, ranging from 0.251 to 0.291 (figures 4.10, 4.11, and 4.12).

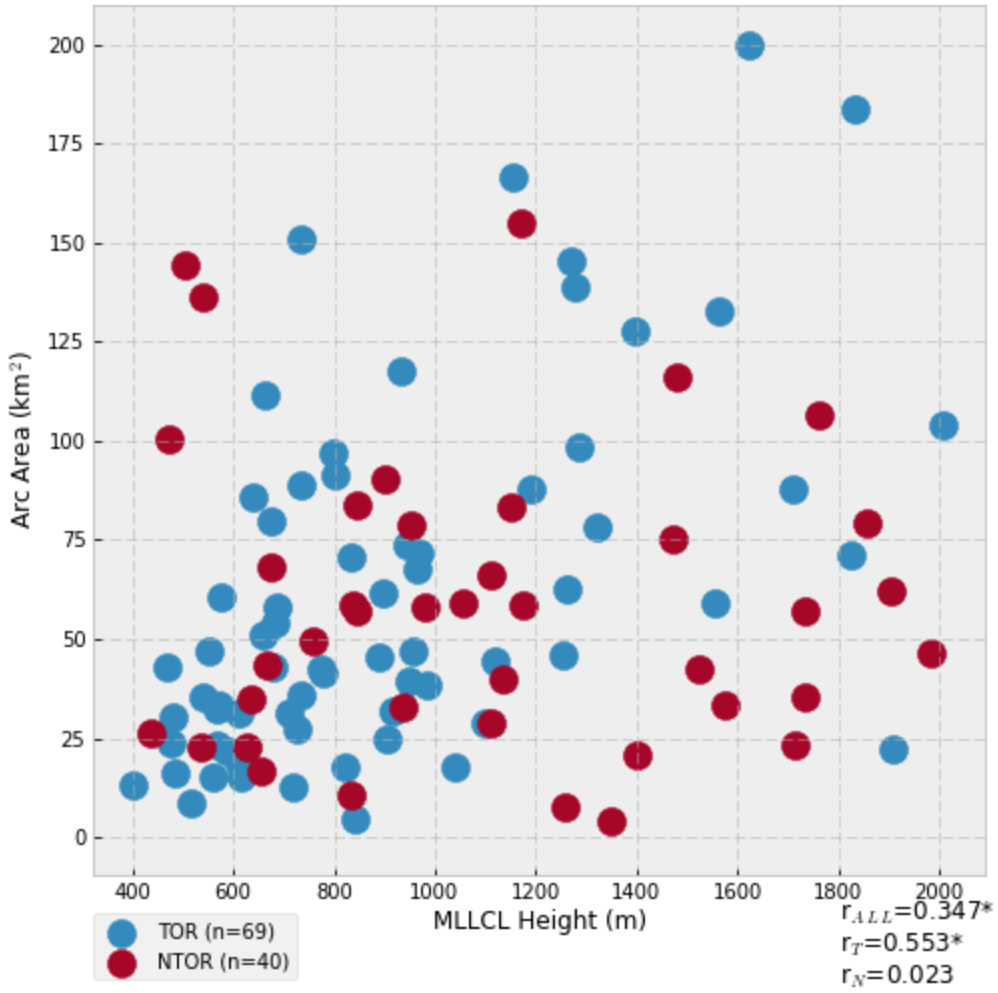

Figure 4.7: Scatter plot of arc area and MLLCL height. Tornadic storms are plotted in blue and nontornadic storms in red, and correlations (bottom right) are statistically significant at $p < 0.05$ if followed by an asterisk.

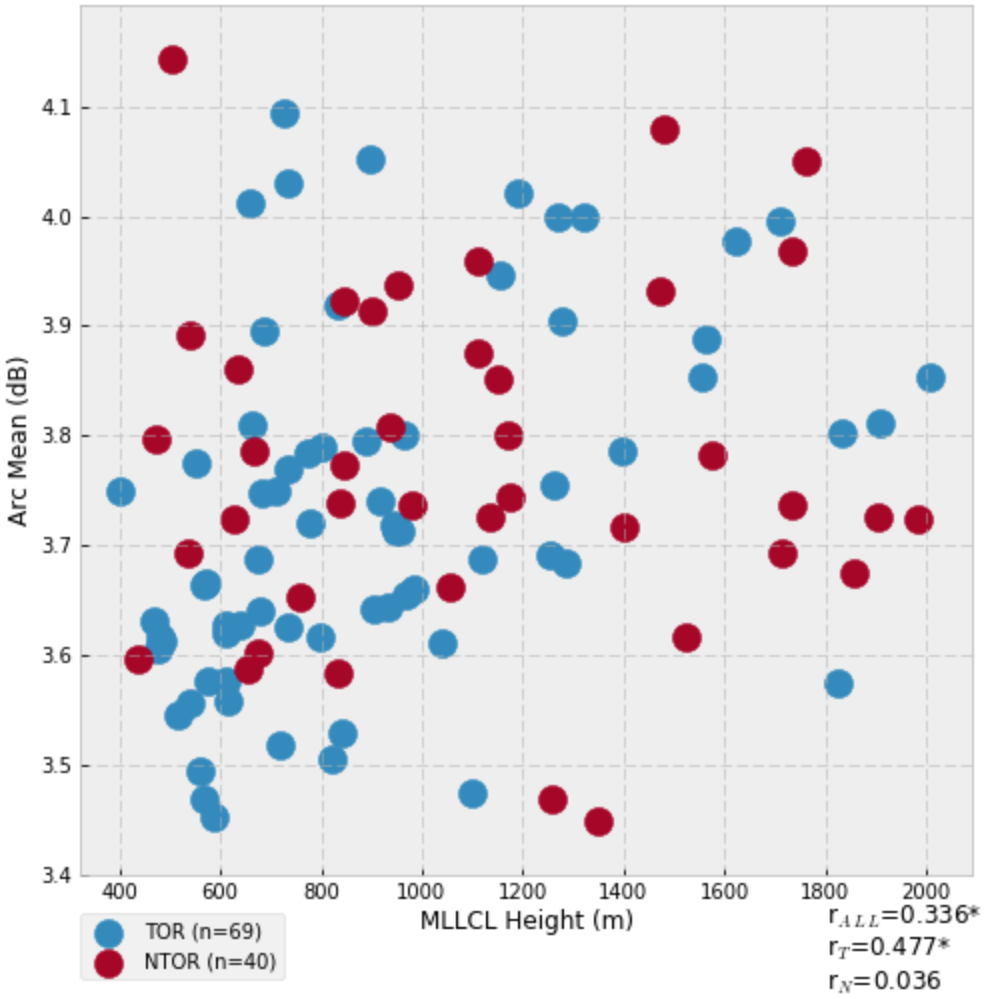

Figure 4.8: Scatter plot of mean Z_{DR} value in the arc and MLLCL height. Tornadic storms are plotted in blue and nontornadic storms in red, and correlations (bottom right) are statistically significant at $p < 0.05$ if followed by an asterisk.

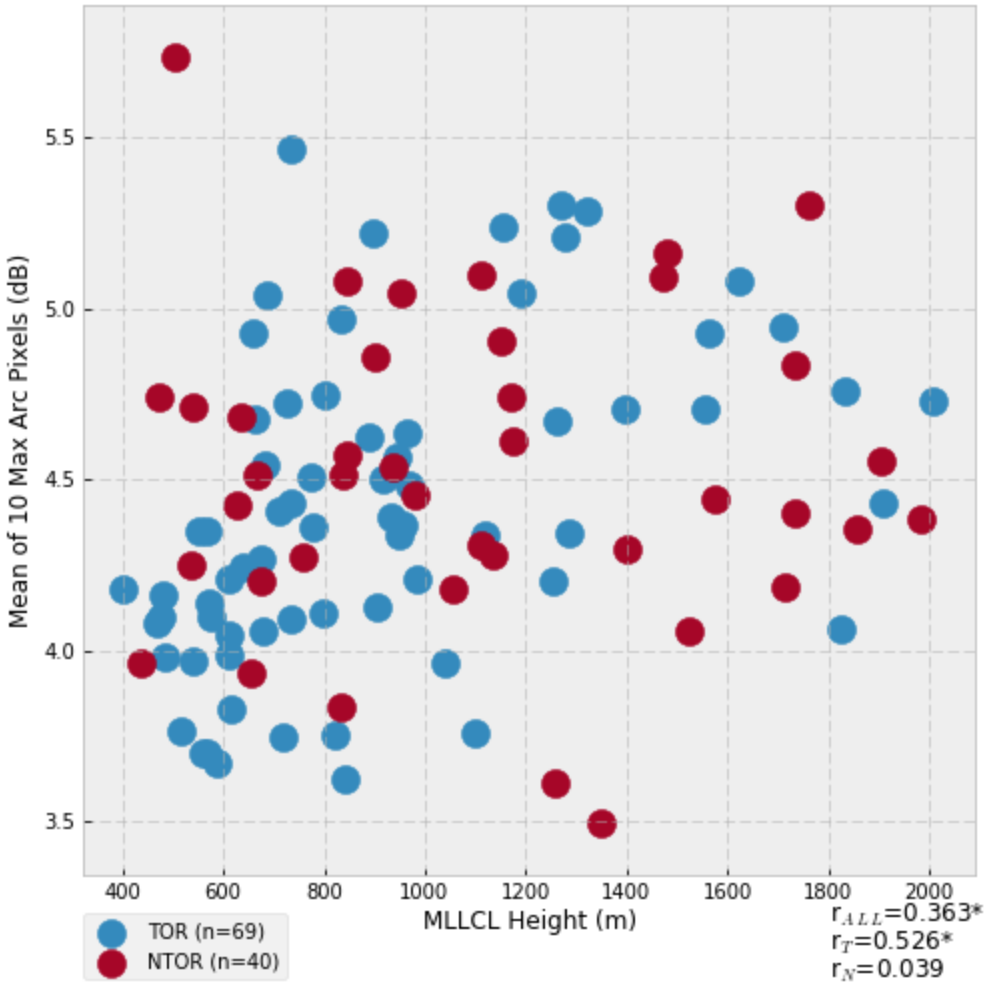

Figure 4.9: Scatter plot of the mean of the 10 top arc Z_{DR} values and MLLCL height. Tornadic storms are plotted in blue and nontornadic storms in red, and correlations (bottom right) are statistically significant at $p < 0.05$ if followed by an asterisk.

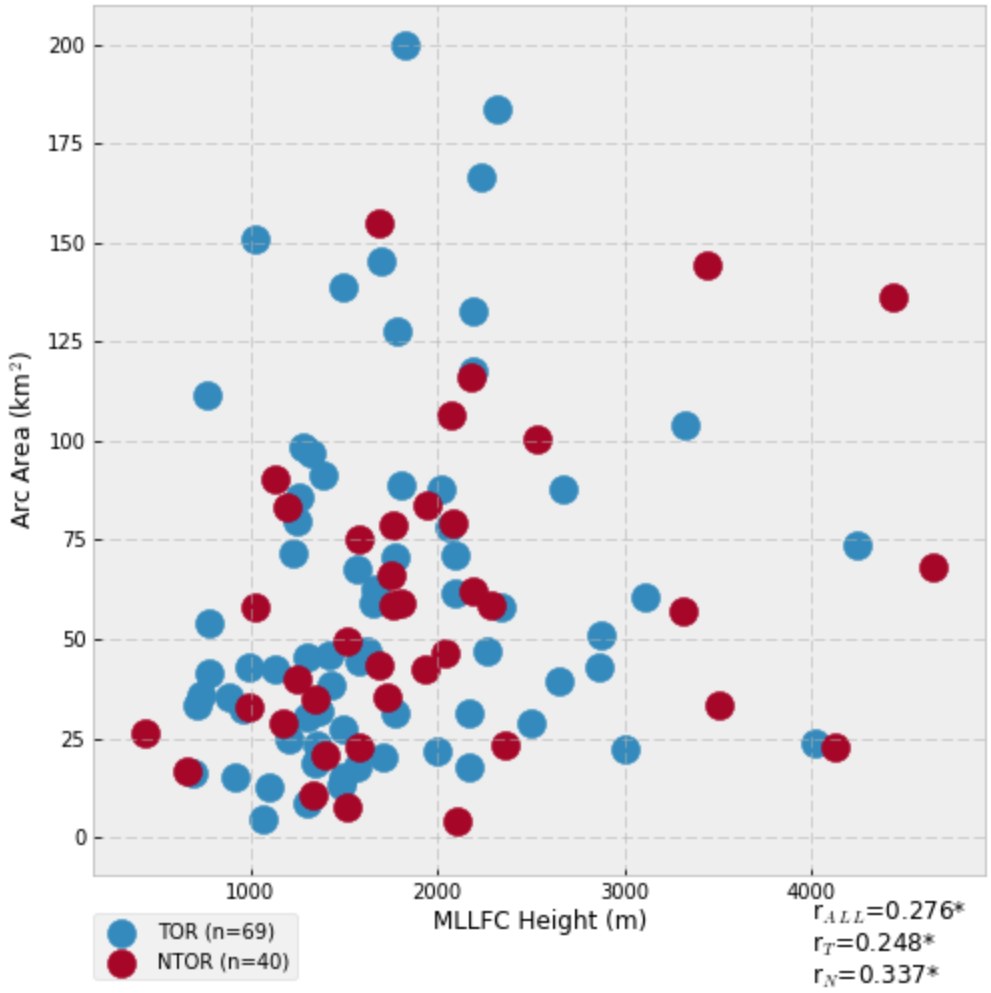

Figure 4.10: Scatter plot of arc area and MLLFC height. Tornadic storms are plotted in blue and nontornadic storms in red, and correlations (bottom right) are statistically significant at $p < 0.05$ if followed by an asterisk.

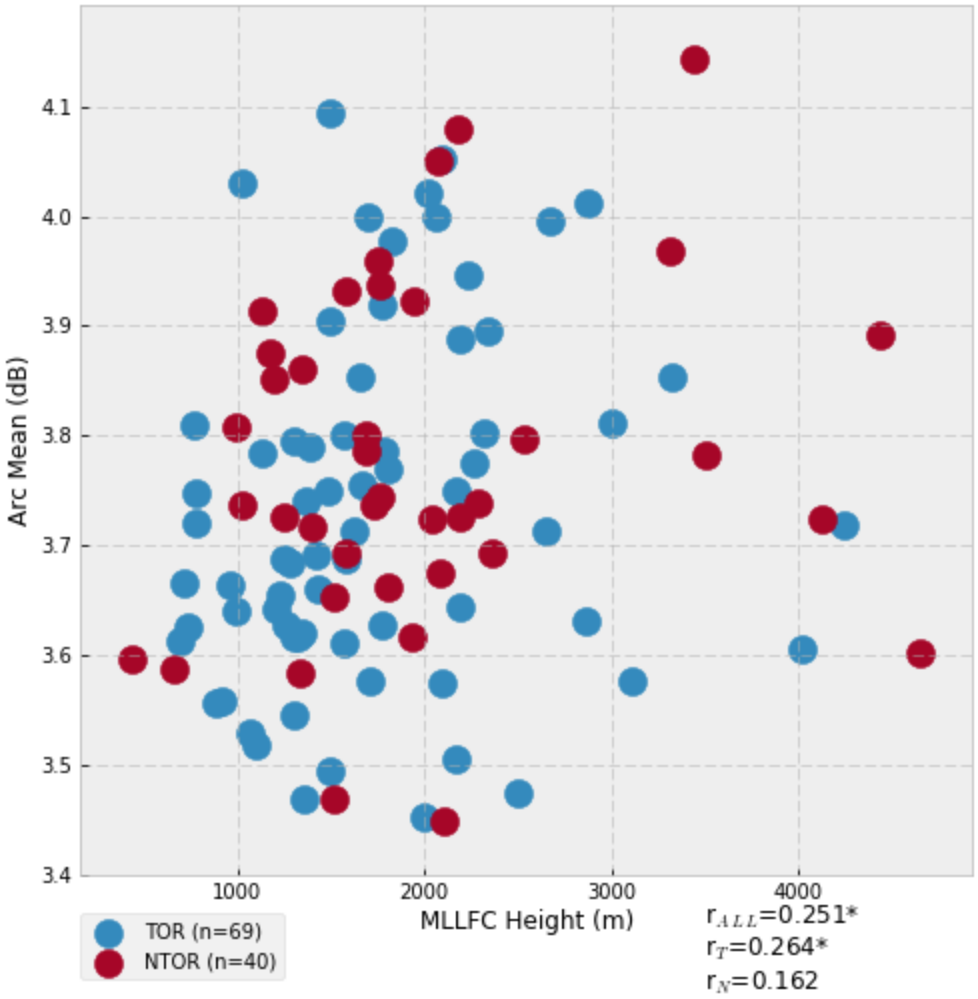

Figure 4.11: Scatter plot of mean Z_{DR} value in the arc and MLLFC height. Tornadic storms are plotted in blue and nontornadic storms in red, and correlations (bottom right) are statistically significant at $p < 0.05$ if followed by an asterisk.

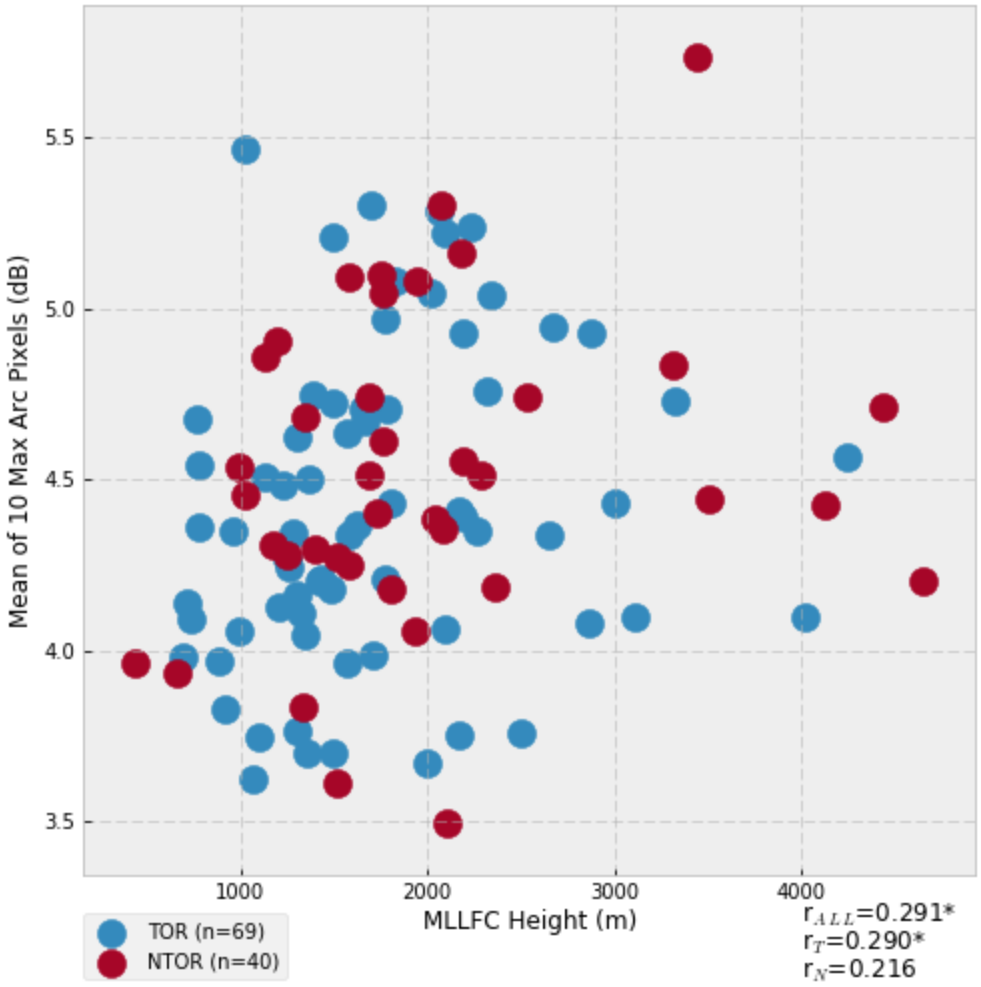

Figure 4.12: Scatter plot of the mean of the 10 top arc Z_{DR} values and MLLFC height. Tornadic storms are plotted in blue and nontornadic storms in red, and correlations (bottom right) are statistically significant at $p < 0.05$ if followed by an asterisk.

D. Low-Level Shear and SRH

Previous studies (Kumjian and Ryzhkov 2009, Dawson et al. 2014b) have used idealized simulations to indicate that Z_{DR} arcs should be more intense in environments with stronger low-level shear and larger SRH, due to the greater magnitude of storm-relative winds in these environments leading to stronger drop-size sorting. However, no significant positive correlations were found between arc areal extent or intensity and any of the shear or SRH parameters examined in this study. The strongest correlations between any SRH or shear parameters and arc metrics were found in the surface-1 km AGL layer, with weak but statistically significant inverse relationships between surface-1 km SRH and mean Z_{DR} value in the arc (r= -0.217, figure 4.13) and between all arc metrics and surface-1 km shear (r between -0.242 to -0.252, figures 4.14 through 4.16). However, the weak correlation between surface-1km SRH and mean arc Z_{DR} values weakens and becomes statistically insignificant when using observed storm motions instead of predicted motions. To further examine possible reasons for these results, pressure-weighted storm-relative wind magnitudes were calculated for all storms using the two layers just above the Z_{DR} arc (1-3 km AGL and 2-4 km AGL) using both observed and predicted storm motions.

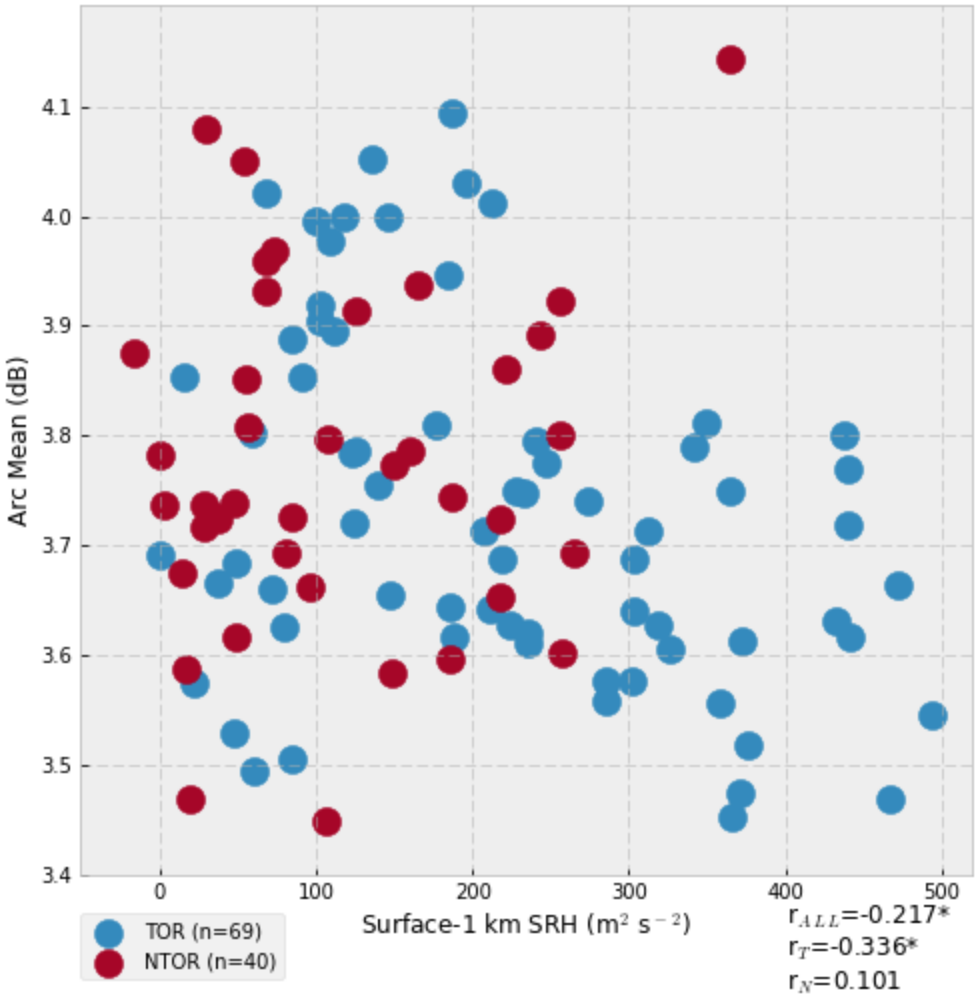

Figure 4.13: Scatter plot of mean Z_{DR} value in the arc and surface-1 km SRH. Tornadic storms are plotted in blue and nontornadic storms in red, and correlations (bottom right) are statistically significant at $p < 0.05$ if followed by an asterisk. SRH was here calculated using predicted storm motions.

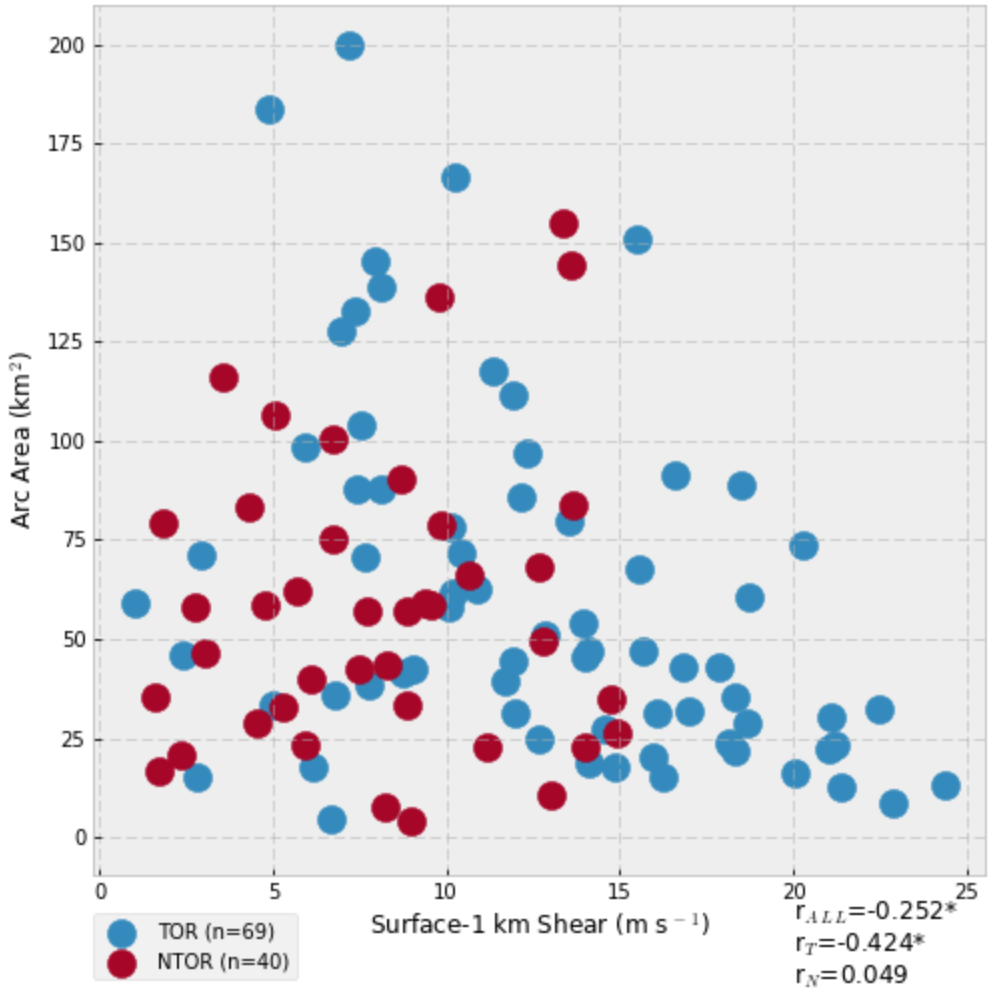

Figure 4.14: Scatter plot of arc area and surface-1 km shear. Tornadic storms are plotted in blue and nontornadic storms in red, and correlations (bottom right) are statistically significant at $p < 0.05$ if followed by an asterisk.

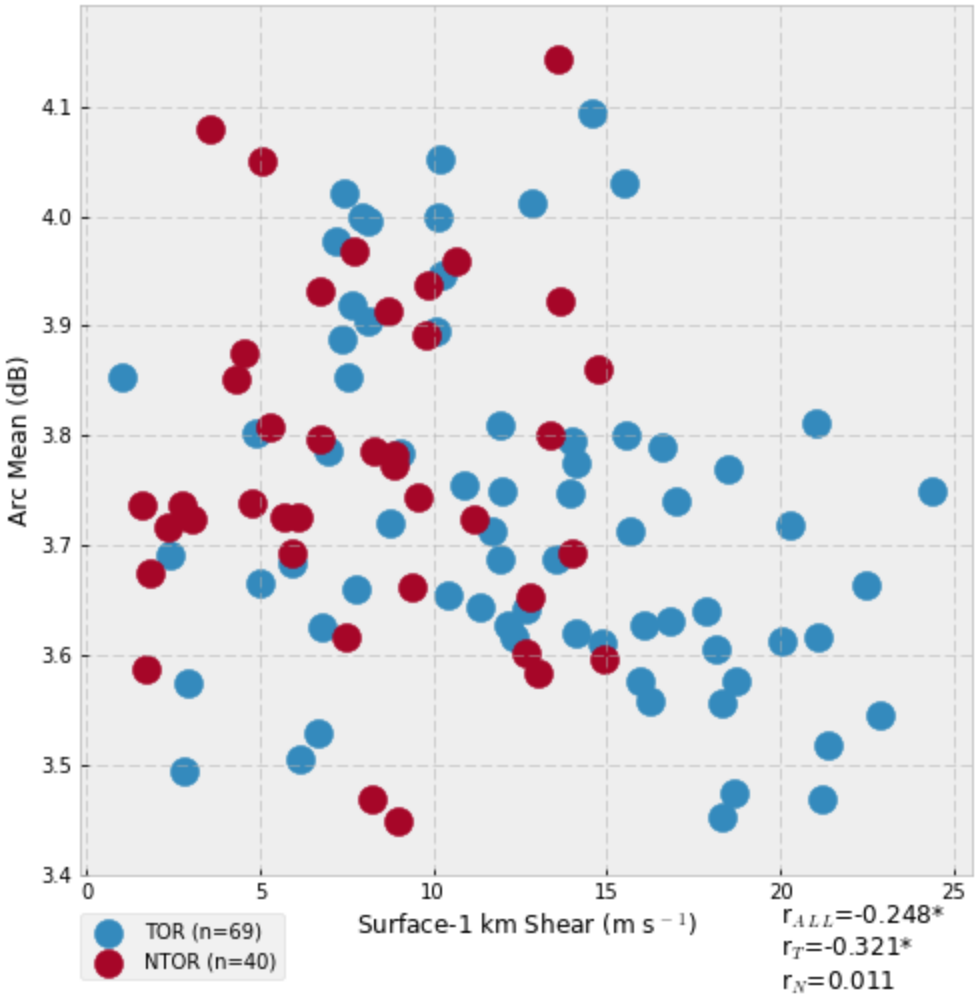

Figure 4.15: Scatter plot of mean arc Z_{DR} value and surface-1 km shear. Tornadic storms are plotted in blue and nontornadic storms in red, and correlations (bottom right) are statistically significant at $p < 0.05$ if followed by an asterisk.

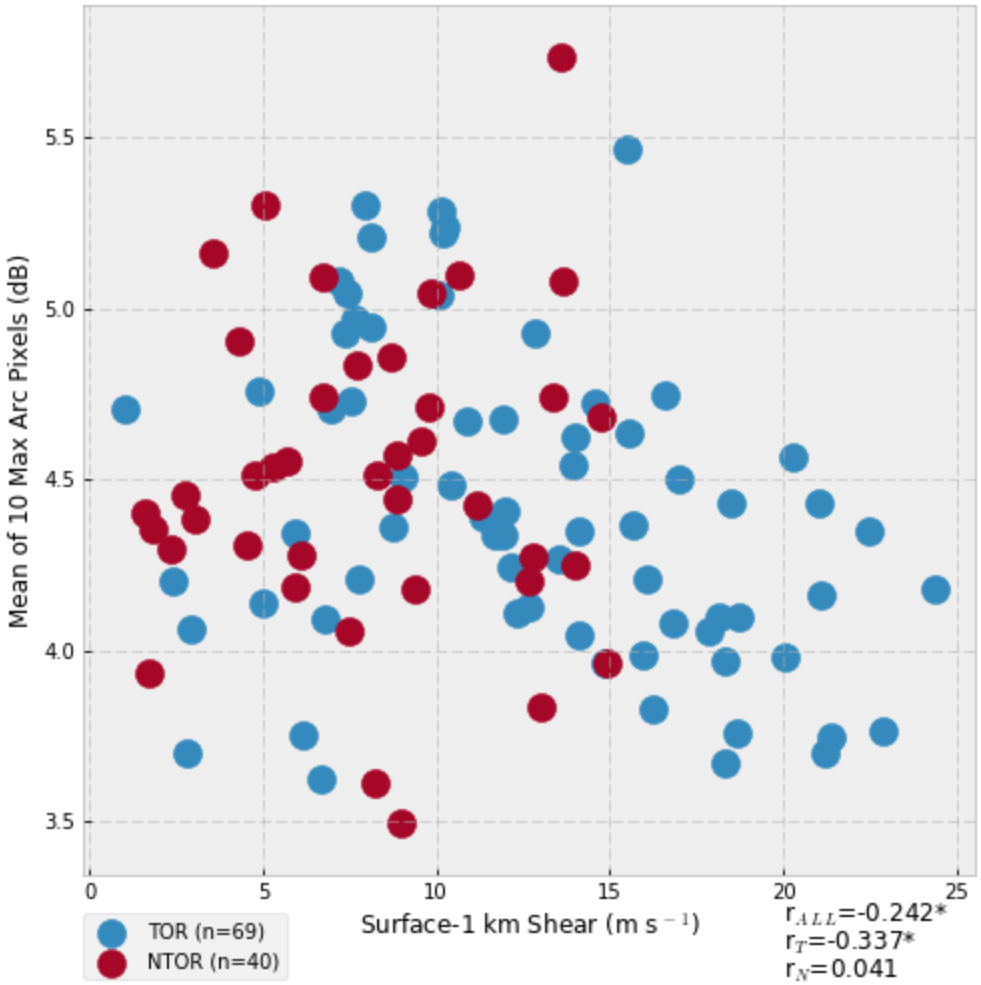

Figure 4.16: Scatter plot of the mean of the 10 max arc Z_{DR} values and surface-1 km shear. Tornadic storms are plotted in blue and nontornadic storms in red, and correlations (bottom right) are statistically significant at $p < 0.05$ if followed by an asterisk.

E. Storm-Relative Wind Magnitude

None of the storm-relative wind parameters showed statistically significant correlations with any of the arc metrics examined (figures 4.17 through 4.19, calculations performed using observed storm motions, only the 1-3 km AGL layer shown). Switching between observed and predicted storm motions (not shown) did not meaningfully change the results, with both analyses showing that arc size and intensity do not appear to be correlated to the strength of the storm-relative wind in the 1-3 km or 2-4 km layers. Since previous work has found that the mechanism for Z_{DR} enhancements in the arc is size sorting by the storm-relative wind (Dawson et al. 2014b), this result was unexpected, and will be examined in greater detail in Chapter 5.

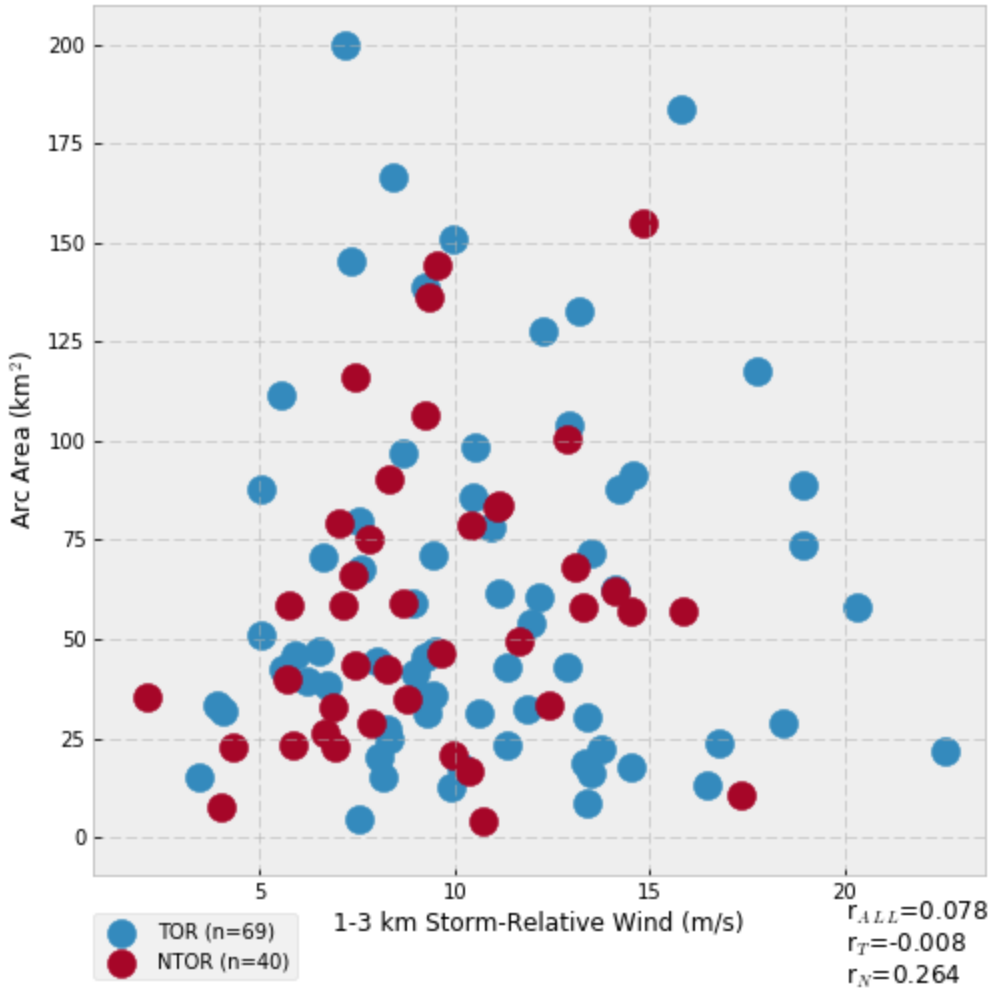

Figure 4.17: Scatter plot of arc area and 1-3 km mean storm-relative wind. Tornadic storms are plotted in blue and nontornadic storms in red, and correlations (bottom right) are statistically significant at $p < 0.05$ if followed by an asterisk. Storm-relative winds calculated using observed storm motions.

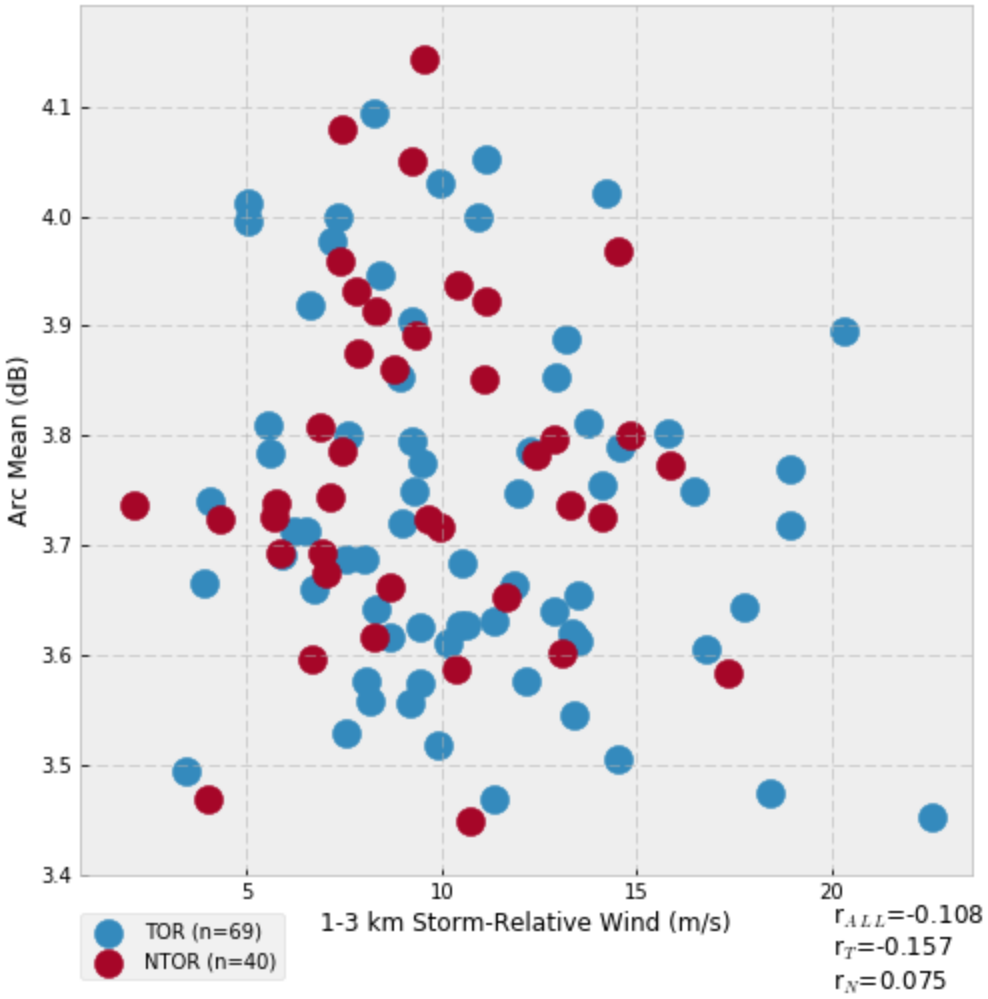

Figure 4.18: Scatter plot of arc mean Z_{DR} value and 1-3 km mean storm-relative wind. Tornadic storms are plotted in blue and nontornadic storms in red, and correlations (bottom right) are statistically significant at $p < 0.05$ if followed by an asterisk. Storm-relative winds calculated using observed storm motions

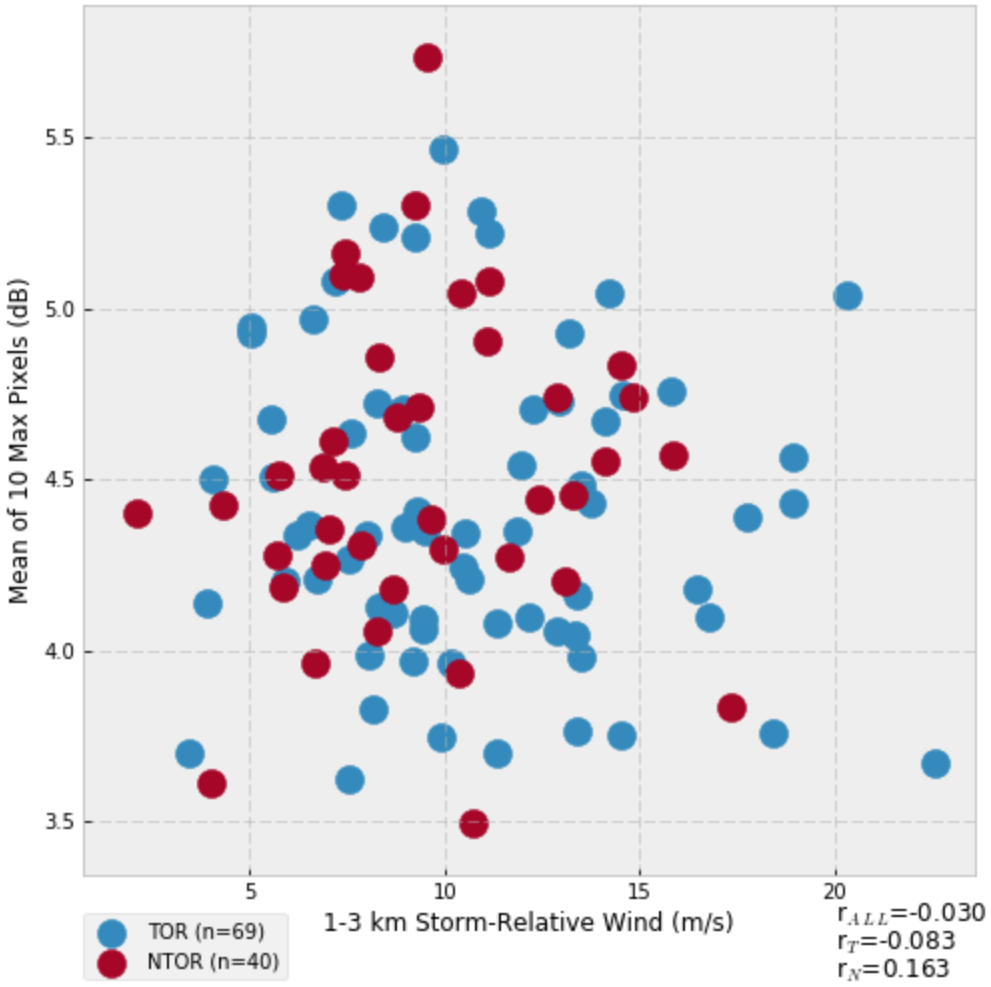

Figure 4.19: Scatter plot of the mean of the 10 max arc Z_{DR} pixels and 1-3 km mean storm-relative wind. Tornadic storms are plotted in blue and nontornadic storms in red, and correlations (bottom right) are statistically significant at $p < 0.05$ if followed by an asterisk. Storm-relative winds calculated using observed storm motions

II. Z_{DR} Arc Characteristics and Low-Level Rotation

Previous work by Kumjian and Ryzhkov (2009) and Dawson et al. (2014b) suggests that changes in Z_{DR} arc metrics could be used to anticipate the development of low-level rotation in supercells by using an increase in arc size and intensity as a proxy for increasing SRH in the near-storm environment. However, the positive correlations between low-level SRH, storm-relative wind strength just above the Z_{DR} arc, and arc size and intensity which would be implied by the results of the idealized simulations in Kumjian and Ryzhkov (2009) and Dawson et al. (2014b) were not found in this study's examination of arc metrics in different environments in the previous section. Nevertheless, since changes in Z_{DR} arc metrics may be influenced by storm inflow strength and storm-induced modifications to the near-storm environment which are not accounted for in the proximity sounding database used in the above analysis, time series of arc metrics and low-level rotation metrics for 50 storms from the dataset used to train the Z_{DR} arc algorithm were compared at lags of 0, 1, 2, and 3 radar scans (approximately 0 to 15 minutes since these cases all used non-SAILS scanning strategies) to see if any useful relationships existed between changes in arc metrics and low-level rotation. One storm was removed from the original training dataset due to most of its Z_{DR} arc detections being false detections in the RFD. Low-level rotation metrics used included rotational velocity and NROT and were calculated as described in section 3.4 for all 577 analysis times. Behavior of individual storms was quite variable, with some exhibiting a pattern where arc growth and intensification would lead low-level rotation intensification by a few radar scans, while others displayed little to no correlation between changes in the arc and changes in low-level rotation.

While larger and stronger Z_{DR} arcs might be expected when low-level rotation is stronger, since stronger low-level inflow at these times might enhance drop size sorting in the arc, correlations between low-level rotation metrics and arc metrics in this analysis were generally weak and often negative. The most substantial correlations were found between the mean Z_{DR} value in the arc averaged over each storm's lifetime and mean low-level rotation strength over each analysis period, with rotation strength generally decreasing with higher mean Z_{DR} values in the arc (r = -0.413 for rotational velocity and r = -0.444 for NROT, figures 4.20 and 4.21). Correlations were weaker between all individual observations of mean arc Z_{DR} value and low-level rotation strength and between each storm's lifetime-averaged mean arc Z_{DR} value and its lifetime-maximum low-level rotation value, but a slight negative trend was still evident in each (figures 4.20 and 4.21). Results for the mean of the 10 maximum Z_{DR} values in the arc were similar to those for the arc mean Z_{DR} value but with slightly weaker relationships with low-level rotation, with this metric having its best correlation to rotational velocity and NROT when averaged over each analysis period (figures 4.22 and 4.23). Z_{DR} arc areal extent was almost entirely uncorrelated with rotational velocity but displayed weak correlations with NROT, with the highest correlation between arc area and either rotation metric being r = -0.317 between storm-average arc area and storm-average NROT (figures 4.24 and 4.25). Correlations between rotational velocity and all three arc metrics at 1, 2, and 3 5-minute radar scan lags were generally weaker than or similar to the values found for unlagged data. Correlations for the intensity metrics tended to decrease in strength with increasing lag, while those for arc areal extent increased very slightly and became statistically significant but remained so small as to be of little practical use.

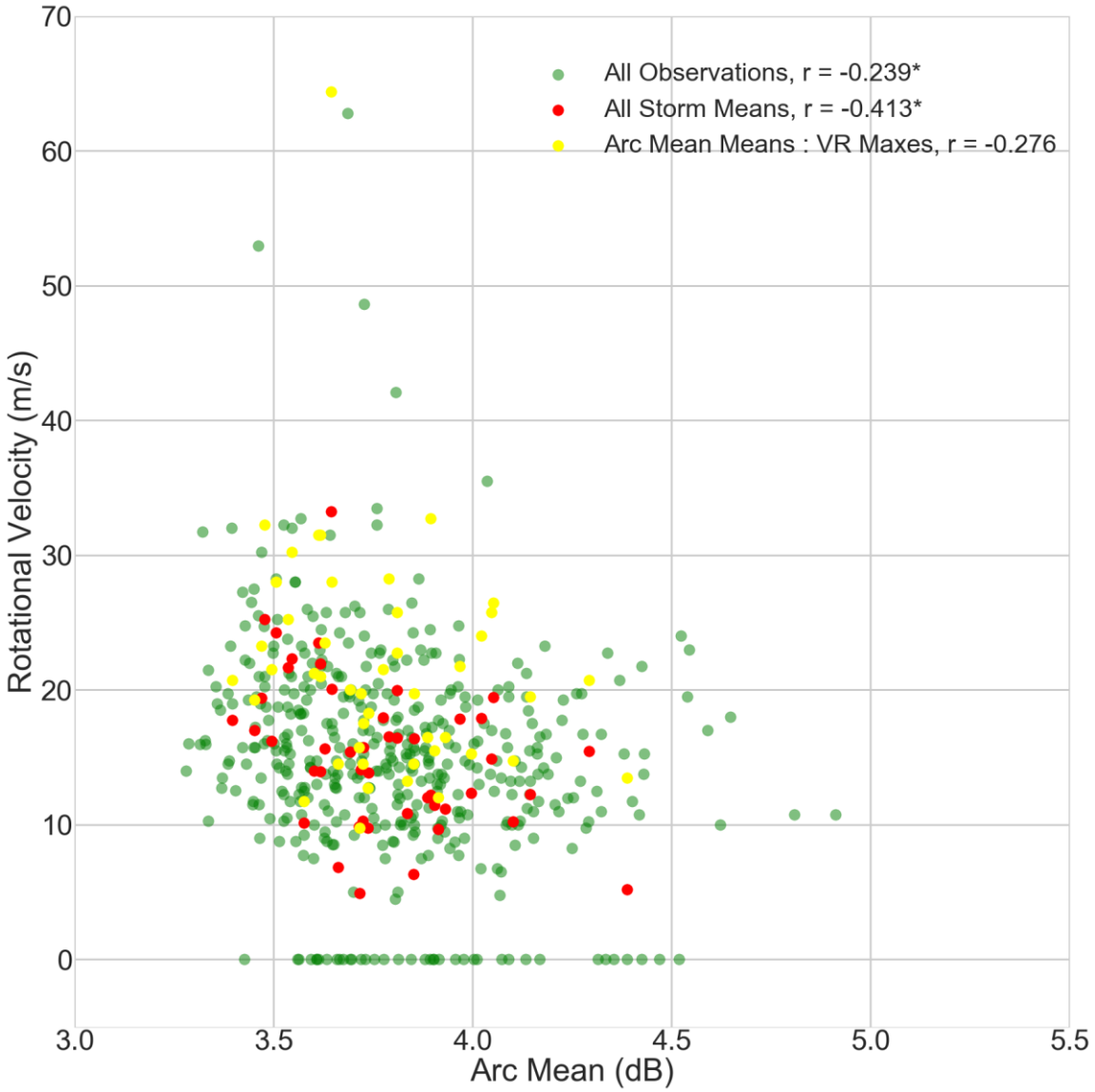

Figure 4.20: Scatter plot of mean arc Z_{DR} value and rotational velocity. Red dots indicate both variables averaged for each storm, while the yellow dots are storm-average mean arc Z_{DR} values plotted against storm maximum rotational velocity. Correlations are displayed for each comparison at top right and are significant at $p < 0.05$ if followed by an asterisk.

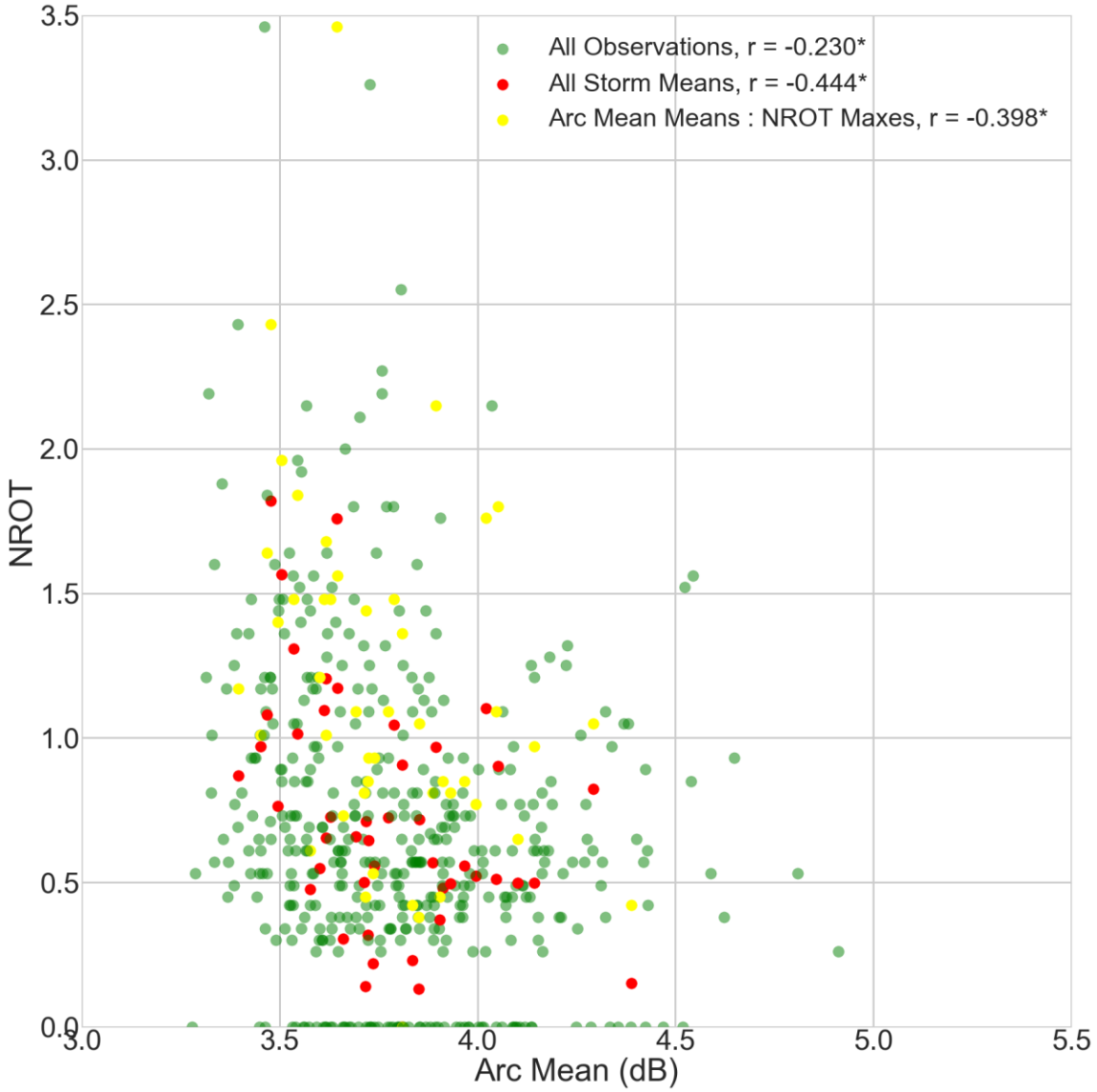

Figure 4.21: Scatter plot of mean arc Z_{DR} value and NROT. Red dots indicate both variables averaged for each storm, while the yellow dots are storm-average mean arc Z_{DR} values plotted against storm maximum rotational velocity. Correlations are displayed for each comparison at top right and are significant at $p < 0.05$ if followed by an asterisk.

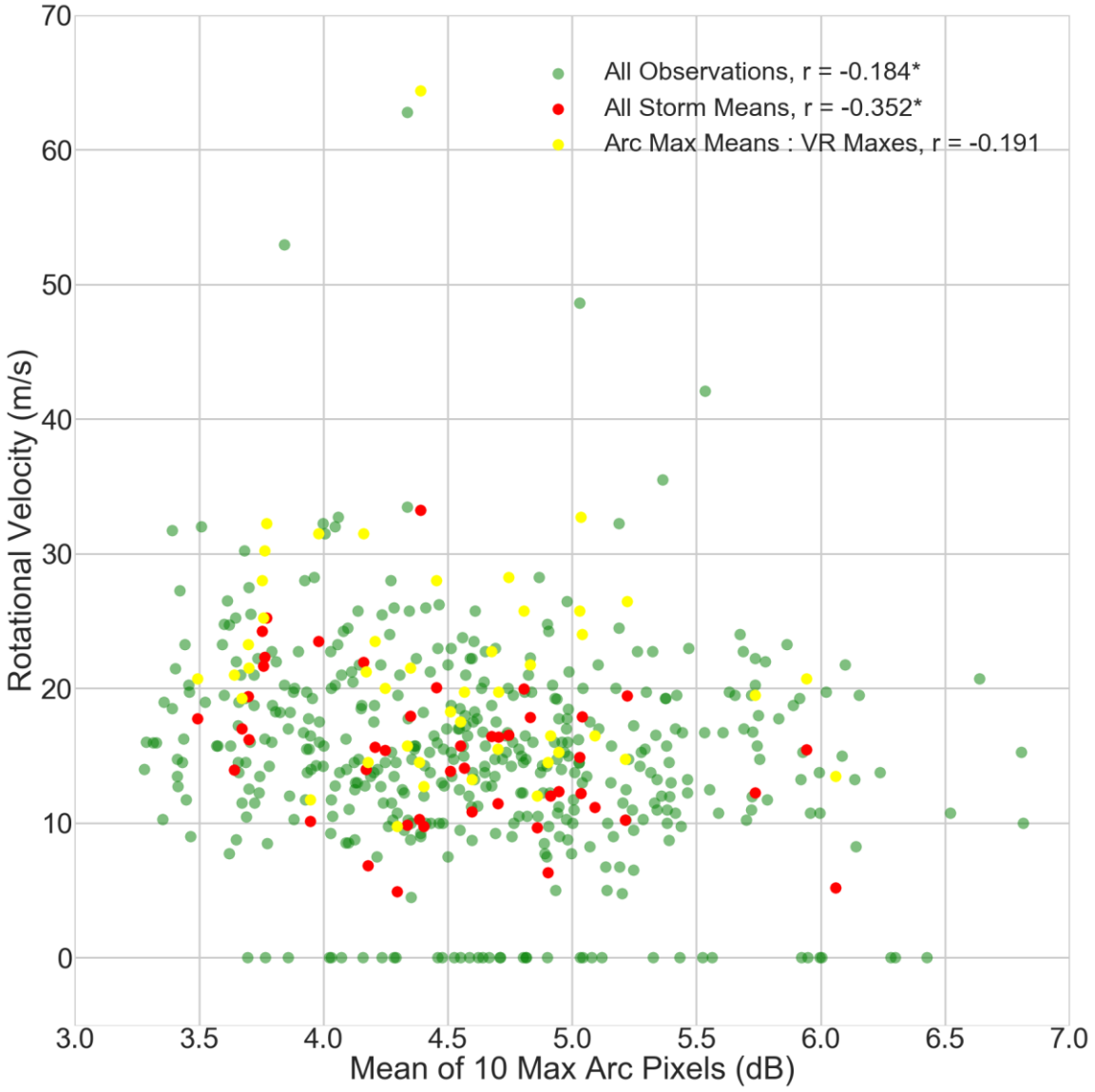

Figure 4.22: Scatter plot of the mean of the ten highest arc Z_{DR} pixels and rotational velocity. Red dots indicate both variables averaged for each storm, while the yellow dots are storm-average mean arc Z_{DR} values plotted against storm maximum rotational velocity. Correlations are displayed for each comparison at top right and are significant at $p < 0.05$ if followed by an asterisk.

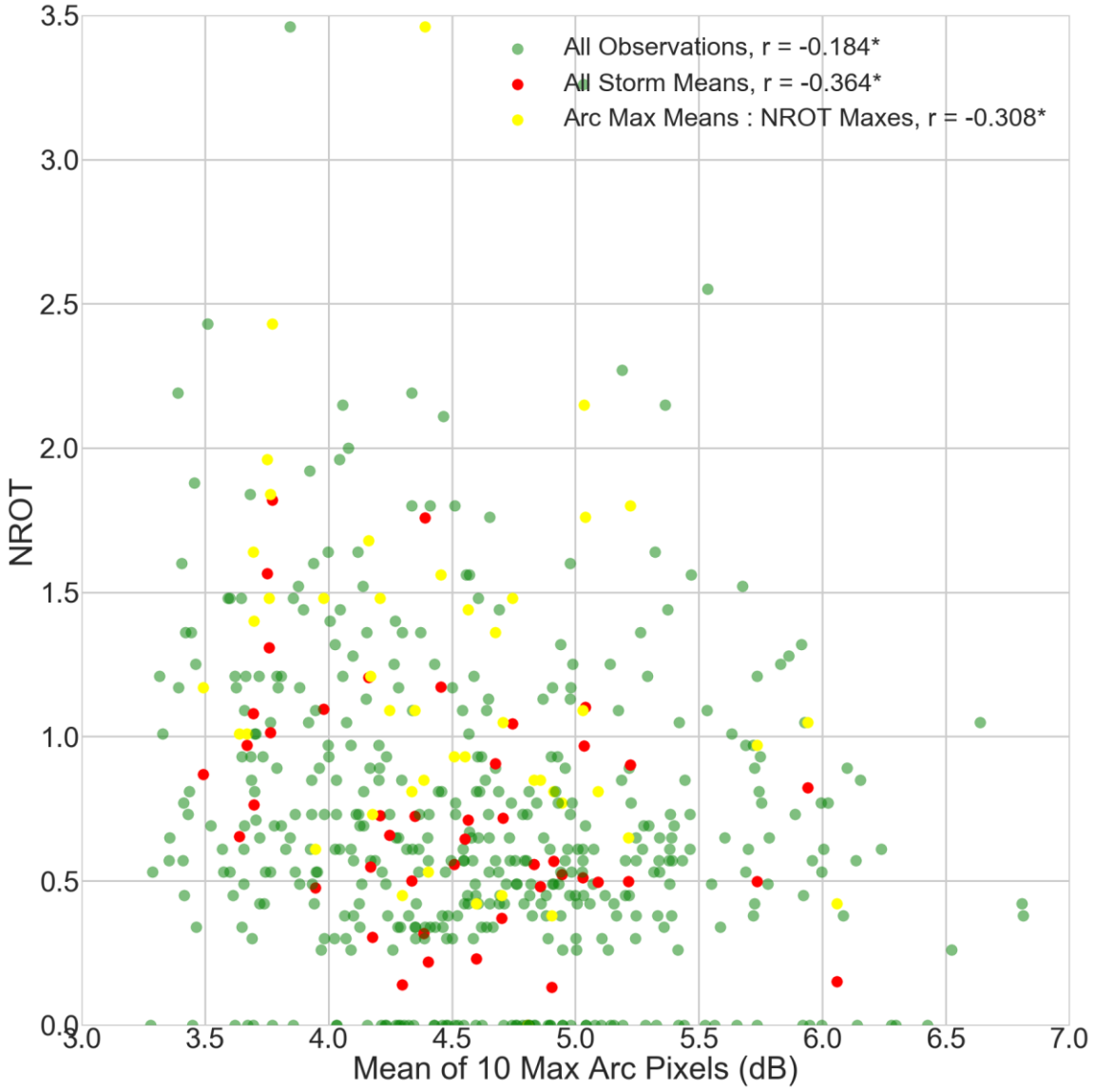

Figure 4.23: Scatter plot of the mean of the ten highest arc Z_{DR} pixels and NROT. Red dots indicate both variables averaged for each storm, while the yellow dots are storm-average mean arc Z_{DR} values plotted against storm maximum rotational velocity. Correlations are displayed for each comparison at top right and are significant at $p < 0.05$ if followed by an asterisk.

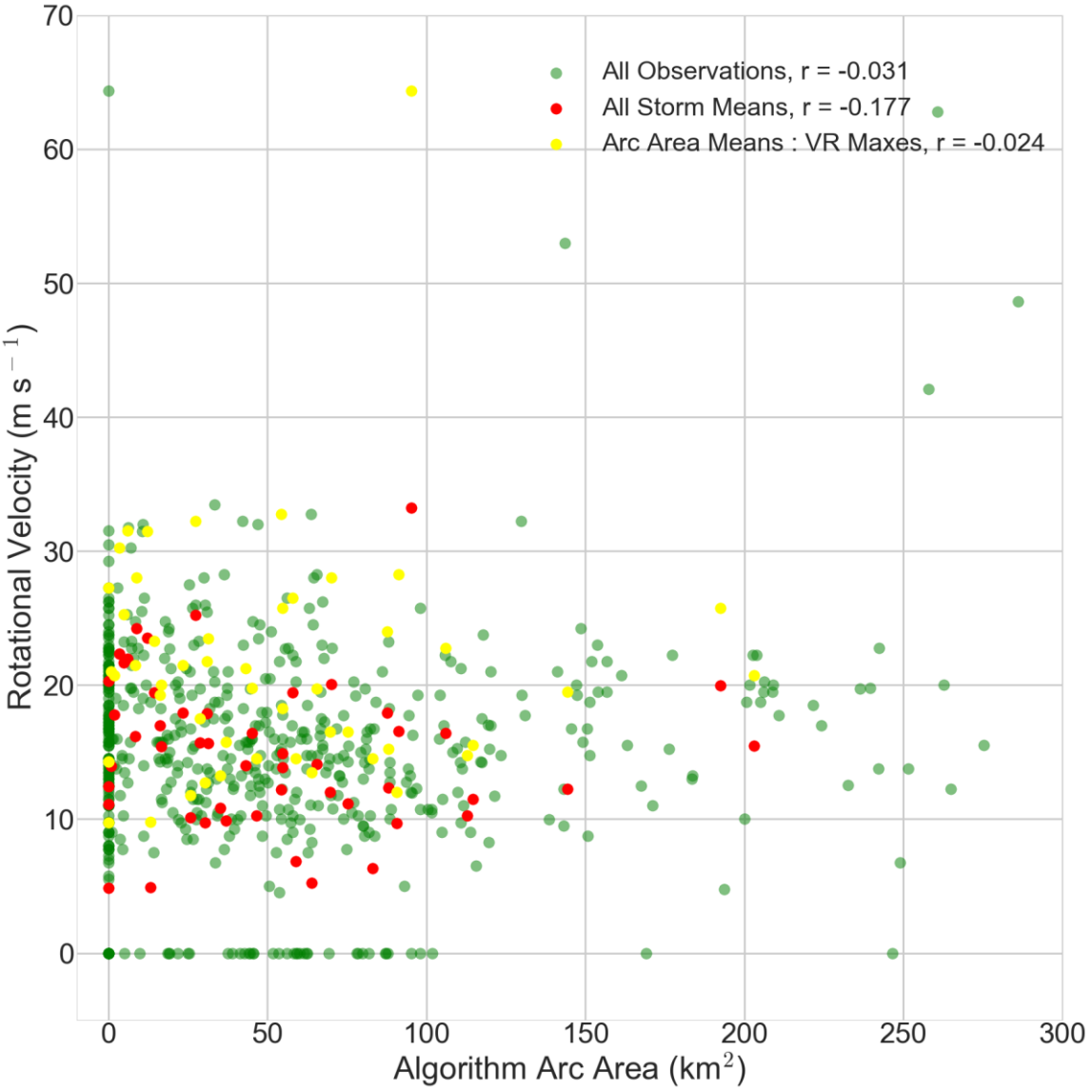

Figure 4.24: Scatter plot of arc area and rotational velocity. Red dots indicate both variables averaged for each storm, while the yellow dots are storm-average mean arc Z_{DR} values plotted against storm maximum rotational velocity. Correlations are displayed for each comparison at top right and are significant at $p < 0.05$ if followed by an asterisk.

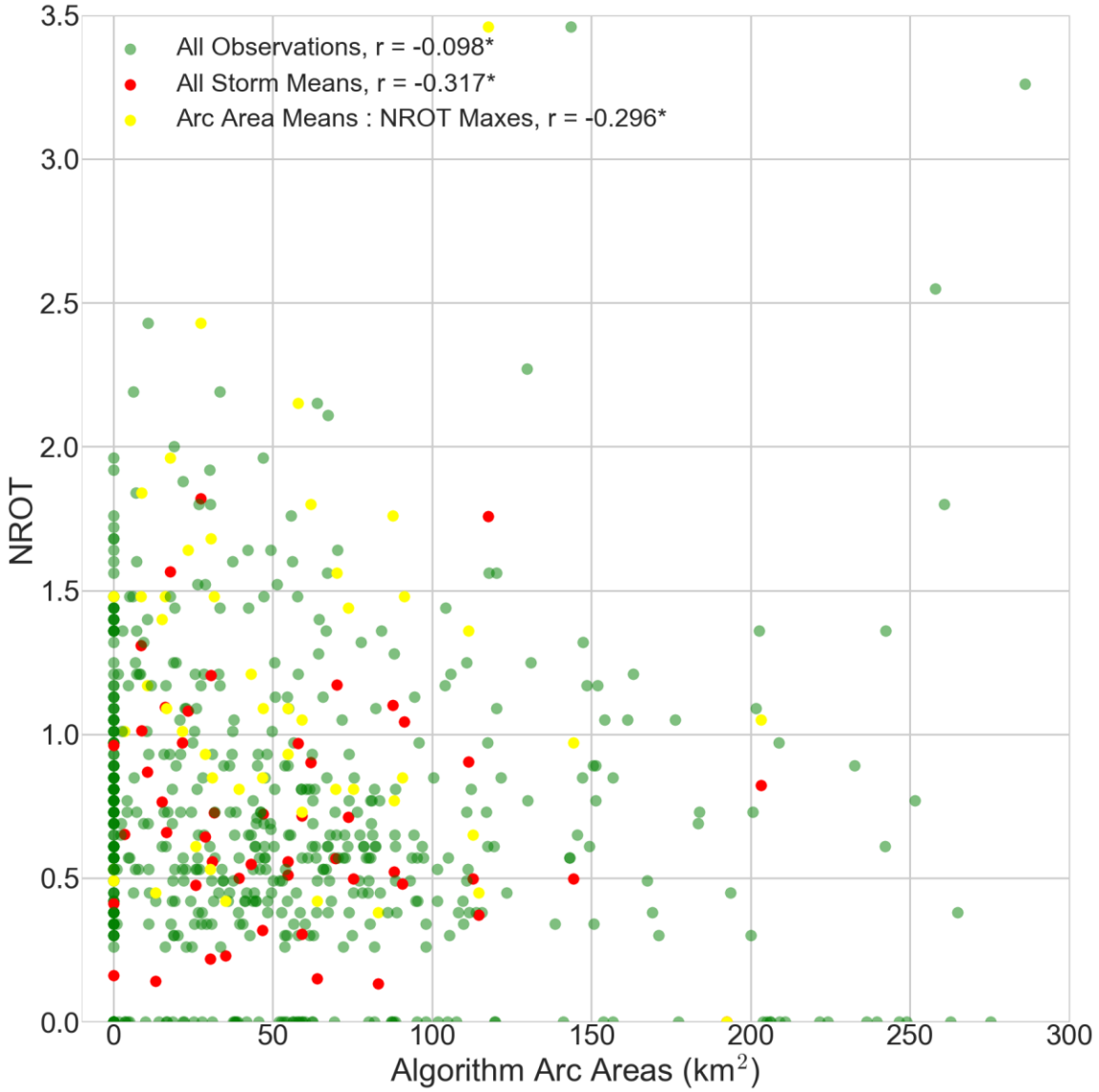

Figure 4.25: Scatter plot of arc area and NROT. Red dots indicate both variables averaged for each storm, while the yellow dots are storm-average mean arc Z_{DR} values plotted against storm maximum rotational velocity. Correlations are displayed for each comparison at top right and are significant at $p < 0.05$ if followed by an asterisk.

III. Z_{DR} Arc Characteristics over Supercell and Tornado Life Cycles

A. Mean Arc Characteristics in Tornadic and Nontornadic Storms

Previous work comparing the Z_{DR} arc characteristics of small samples of tornadic and nontornadic storms has found that tornadic storms are more likely to produce very high values of Z_{DR} in their arcs (Crowe et al. 2012) and that tornadic storms often have larger, more intense arcs during times when they are producing a tornado than times when no tornado is present (VDB17). Thus, it might be expected that tornadic storms would generally have larger, stronger Z_{DR} arcs than nontornadic storms. However, the results presented here using the 109 supercells from section 4 show that tornadic and nontornadic supercells generally have similar distributions of arc characteristics, with no statistically significant differences found between storm mean arc areas, arc mean Z_{DR} values, or the mean of the 10 maximum arc Z_{DR} values between the two categories (figures 4.26, 4.27, and 4.28). Nontornadic storms did tend to have slightly more intense arcs (figures 4.26 and 4.27), however, this trend was not statistically significant and was so small (less than 0.5 dB difference for both metrics) as to be of little operational use in differentiating tornadic and nontornadic storms. For these comparisons and all other boxplots in this thesis, the statistical significance of comparisons between tornadic and nontornadic samples is determined using a Wilcoxon-Mann-Whitney test, with differences considered significant when $p < 0.05$.

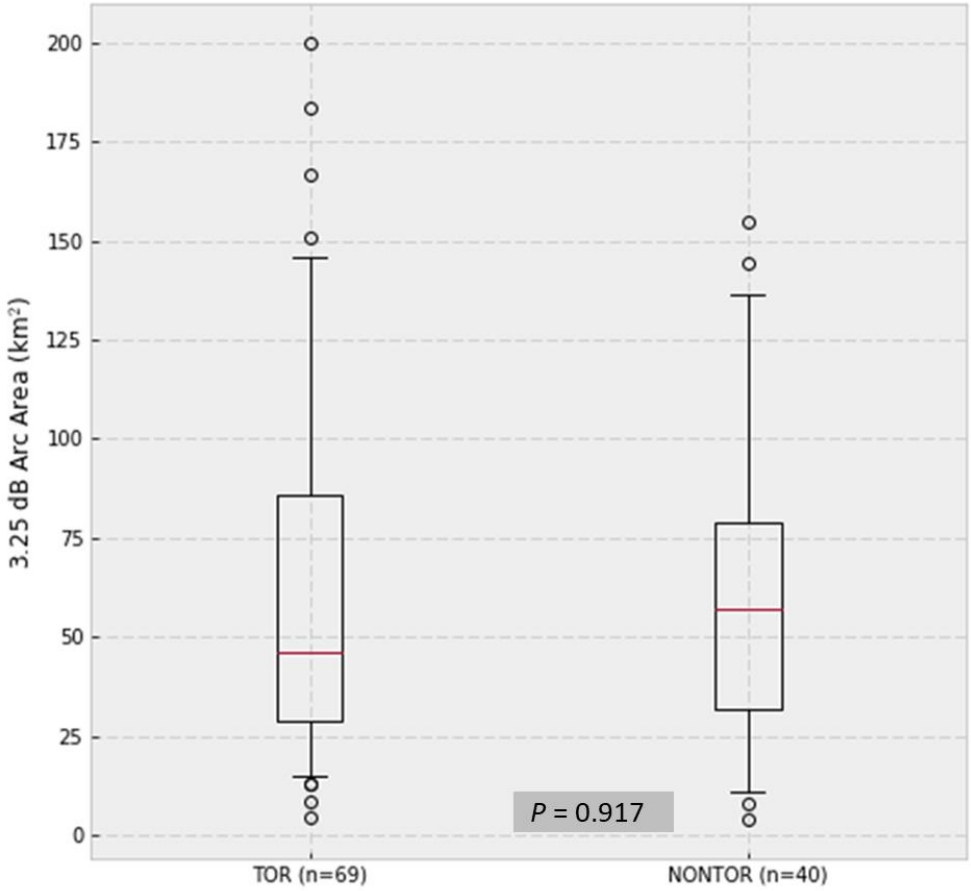

Figure 4.26: Box-and-whisker plot of Z_{DR} arc areas for the tornadic and nontornadic supercell datasets. Wilcoxon-Mann-Whitney *p*-values are displayed in the bottom center of the plot, and boxes extend from the 25th to 75th percentiles with whiskers extending to the 5th and 95th percentiles.

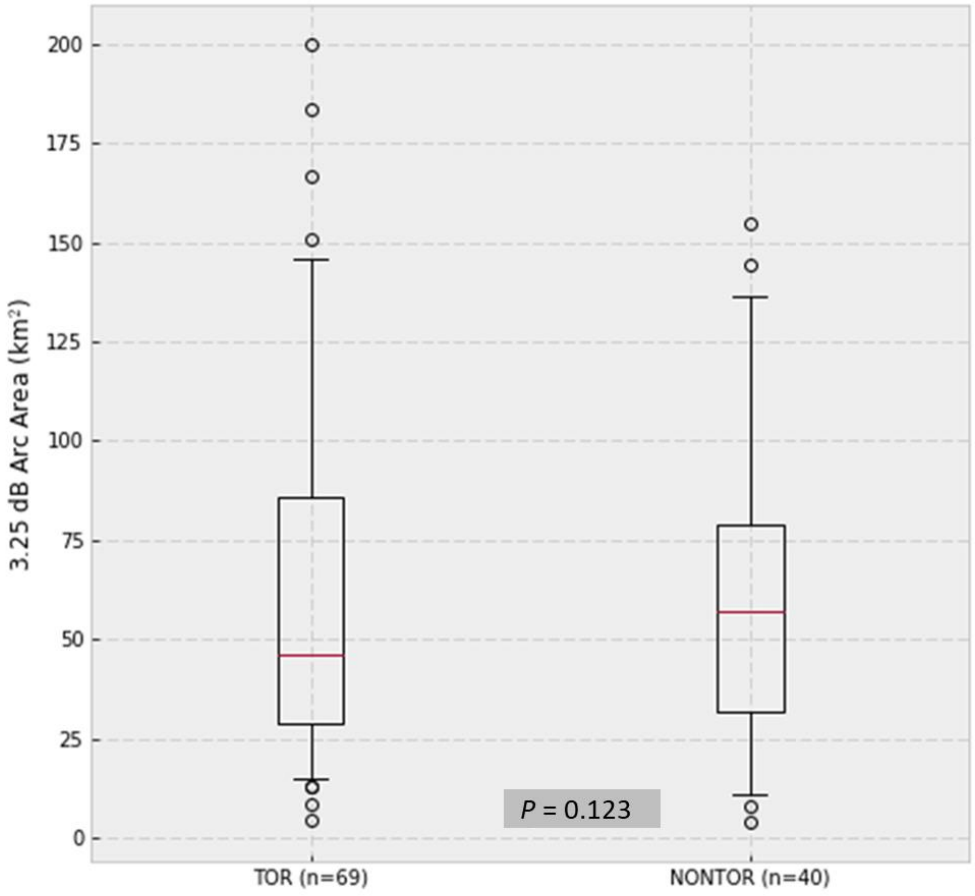

Figure 4.27: Box-and-whisker plot of mean arc Z_{DR} value for the tornadic and nontornadic supercell datasets. Boxplots are formatted as in figure 4.27.

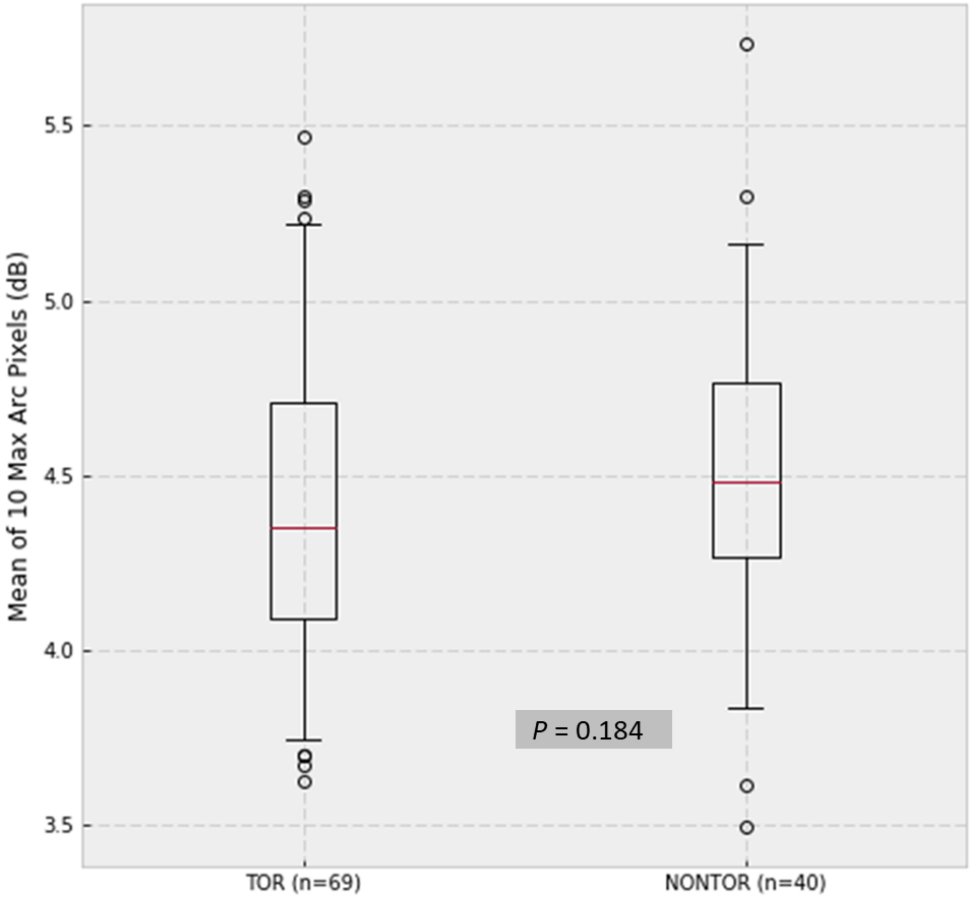

Figure 4.28: Box-and-whisker plot of the mean of the 10 highest arc Z_{DR} values for the tornadic and nontornadic supercell datasets. Boxplots are formatted as in figure 4.27.

B. Arc Characteristics Just Before Tornadogenesis and Tornadogenesis Failure

Prior studies of Z_{DR} arcs in tornadic storms have hinted that an increase in Z_{DR} arc size and intensity may occur during or before tornadogenesis, with Palmer et al. (2011)

observing that a tornado formed as the Z_{DR} arc reorganized following an occlusion cycle in an Oklahoma supercell on 10 May 2010, and VDB17 finding that tornadic supercells tended to have larger and more intense arcs at times when a tornado was occurring than when a tornado was absent. To determine whether a ramp-up in arc size and intensity consistently precedes tornadogenesis, 22 supercells with at least 10 radar scans in SAILS mode capturing the Z_{DR} arc prior to tornadogenesis were selected from the full supercell dataset using the criteria presented in section 3.7. In addition, a tornadogenesis failure dataset of 10 supercells was constructed by selecting storms from the nontornadic dataset which had 10 or more scans of the Z_{DR} arc prior to a well-defined low-level rotation peak (defined as NROT of 0.5 or greater), the time of which was used as the time of tornadogenesis failure as in Markowski et al. (2002). One additional nontornadic storm was added which was not used in the environmental variability analysis due to the absence of RAP sounding data for Z_{DR} calibration as described in section 3.2, bringing the nontornadic dataset to 11 storms. For the tornadic and nontornadic datasets, time series of arc area, arc mean Z_{DR} value, and the mean of the 10 maximum arc pixels were plotted relative to the time of tornadogenesis or tornadogenesis failure and aggregated for all storms as a box-and-whisker plot for each radar scan. In this section, radar scans with no detected arcs were assigned an arc area of 0 km^2 with arc intensity metrics set to NaNs before aggregation. This analysis showed that arc area displays a somewhat consistent increase around 5 radar scans prior to tornadogenesis or tornadogenesis failure, which corresponds to a lag of around 10-15 minutes using a typical SAILS 0.5-degree scan update time of 2 to 3 minutes (figure 4.29). Since this increase could just be a function of increasing storm size during storm strengthening, time series of arc area normalized by

the lowest reflectivity threshold used by the storm tracking algorithm (45 dBZ in most cases) were also plotted (figure 4.30). Although somewhat less pronounced, the increasing trend in arc area seen around 5 radar scans prior to tornadogenesis or tornadogenesis failure is still evident in the normalized arc area, indicating that this trend is likely not just due to increasing storm size. Arc area also appears to decrease during and immediately following tornadogenesis or tornadogenesis failure, although this signal is not as clearly evident as the earlier increase. Meanwhile, the arc intensity metrics displayed a much more ambiguous signal, with no consistent, substantial trends apparent prior to tornadogenesis success or failure in the mean arc value or mean of 10 maximum arc pixels analyses (figures 4.31 and 4.32).

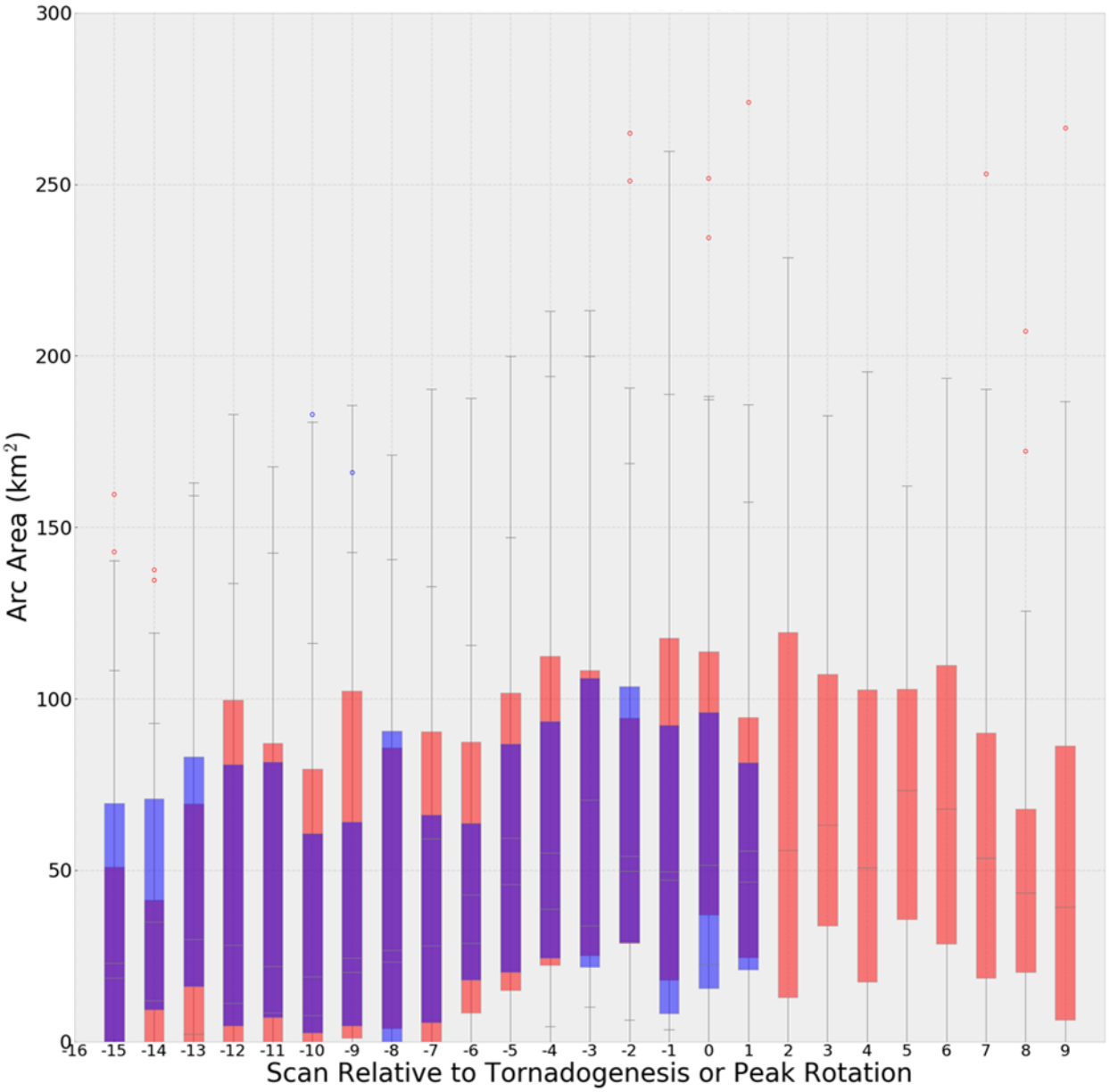

Figure 4.29: Time series of aggregated arc areas for all tornadic (red) and nontornadic (blue) storms relative to tornadogenesis for the tornadic storms or peak NROT for the nontornadic storms. Purple areas represent where box plots for both datasets overlap.

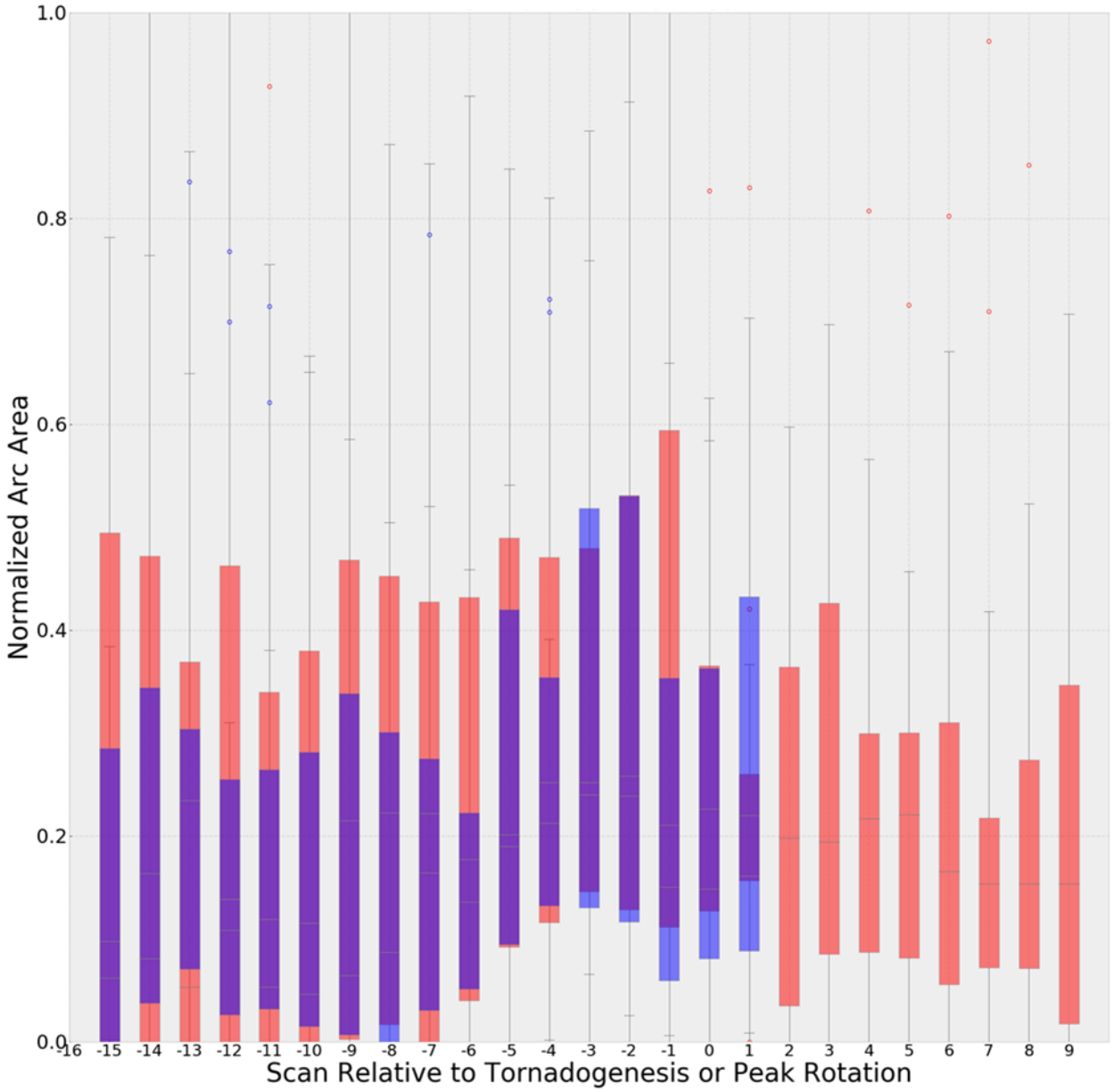

Figure 4.30: As in figure 4.29, except arc area extent is normalized by the area of the lowest reflectivity contour used for storm tracking (45 dBZ in most cases).

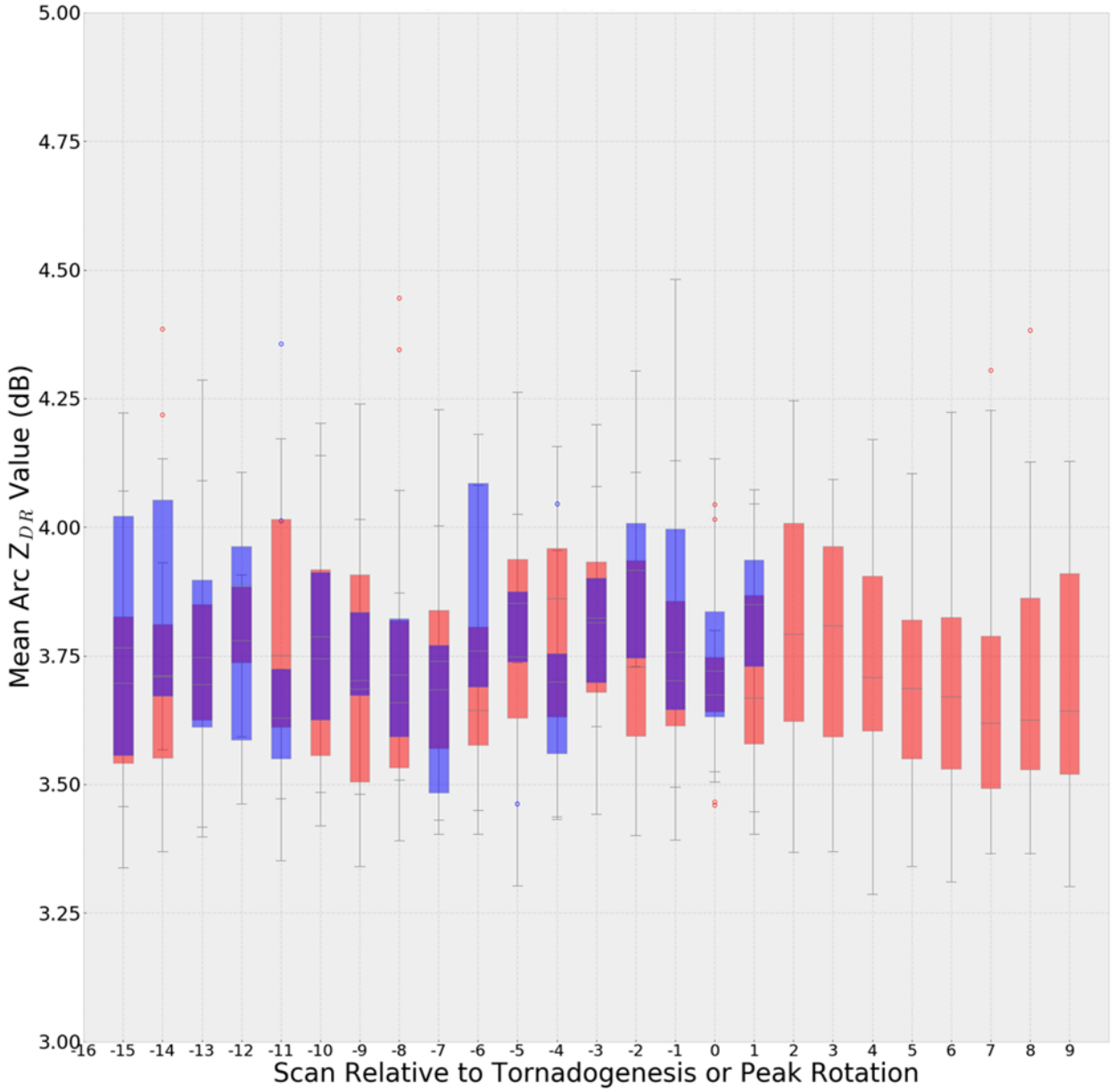

Figure 4.31: As in figure 4.29, except for mean arc Z_{DR} value.

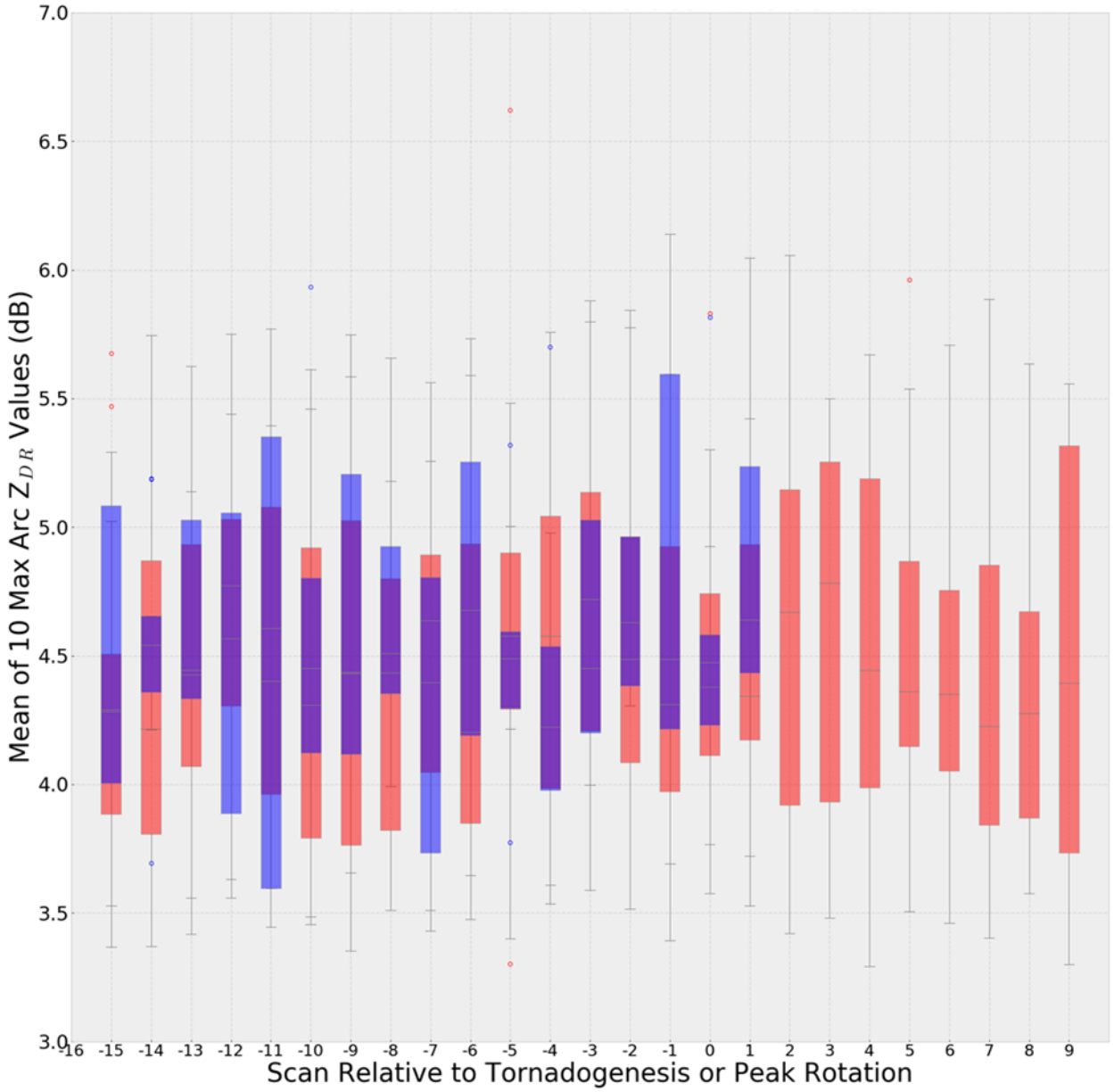

Figure 4.32: As in figure 4.29, except for the mean of the 10 highest arc Z_{DR} values.

C. Arc Changes During Mesocyclone Occlusion

Previous observations in case studies of a tornadic supercell by Palmer et al. (2011) and a nontornadic supercell by Kumjian et al. (2010) found that Z_{DR} arcs followed

a repeatable pattern during low-level mesocyclone cycling, with arcs strengthening and extending back toward the hook echo prior to occlusion and quickly contracting and weakening once occlusion takes place and low-level inflow weakens. To examine whether this pattern holds in a larger sample of supercells, storms which clearly fit the cycling pattern described by Beck et al. (2006) shown in figure 3.7 were sought from the 33-storm dataset examined in the previous section. This resulted in a dataset of 8 storms with at least one clearly identifiable full mesocyclone cycle, for which each radar scan was then assigned to a stage of the Beck et al. (2006) cycling model as described in figure 3.8. Time series of arc characteristics for all 8 storms were then aligned based on the beginning of the first occlusion (defined as the first radar scan to be assigned to stage 2 of the Beck et al. (2006) model) and the end of the first occlusion (defined as the last radar scan from the first category to be assigned to stage 2, since not all storms went through an identifiable stage 3). This analysis revealed variable behavior in arc area extent among the 8 storms examined, with some storms showing a clear drop in arc size around the time of occlusion, while others showed little change or displayed a strengthening arc trend (figures 4.33 and 4.34). Arc intensity metrics showed a slightly more consistent pattern, with most of the storms examined showing a drop in mean arc Z_{DR} value and the mean of the 10 highest arc pixels leading into occlusion (figures 4.35 through 4.38); however, this drop was somewhat small (on the order of ~0.5 dB) and may not be easily distinguishable in operations. Furthermore, due to the very small sample size in this analysis, a study of a larger sample of supercells using a stricter criterion for determining the onset of occlusion is likely necessary in order to draw any definite conclusions as to whether consistent patterns in arc behavior related to mesocyclone occlusion cycles exist.

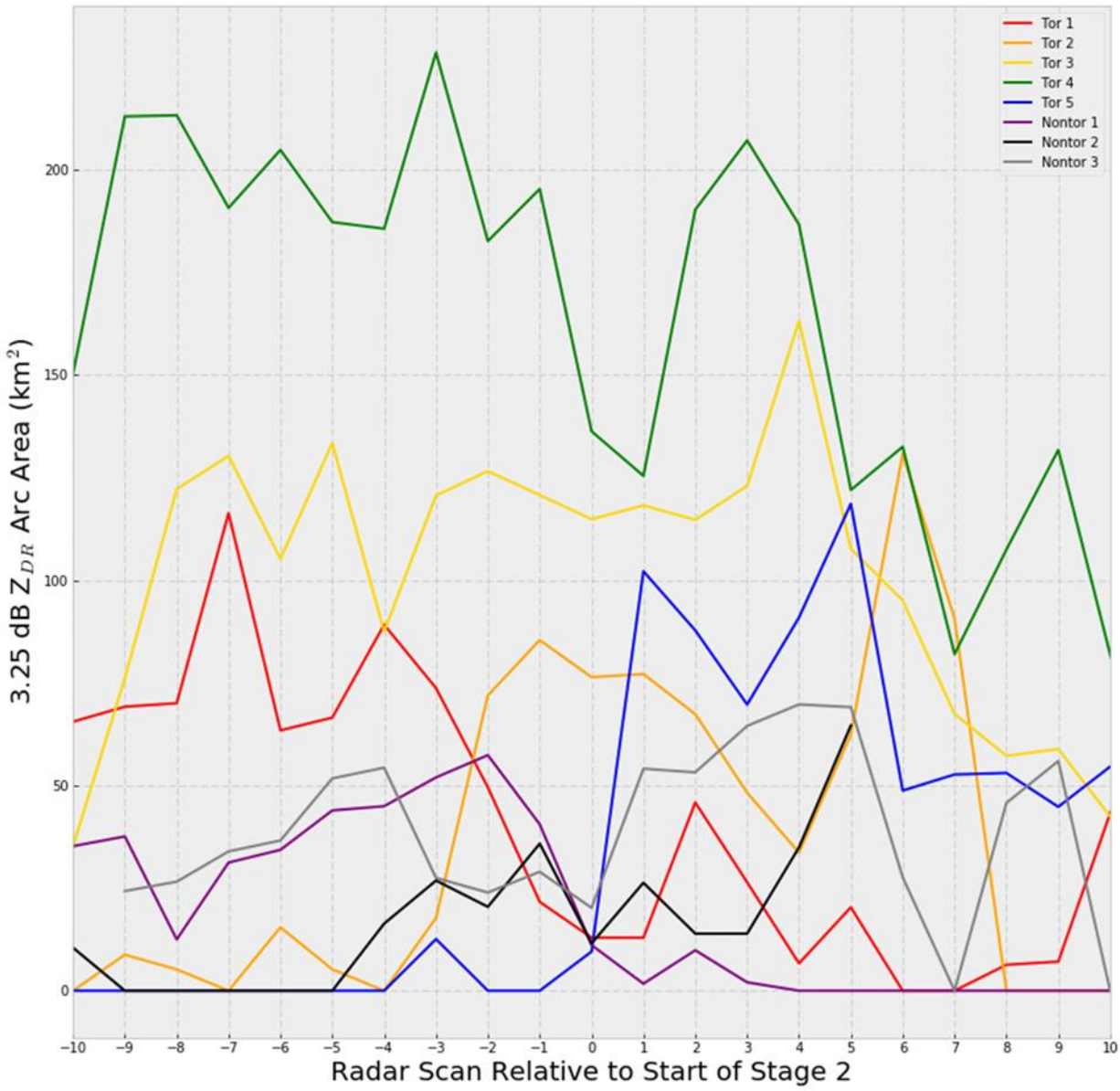

Figure 4.33: Time series of arc areal extent relative to the beginning of occlusion stage 2 for each storm.

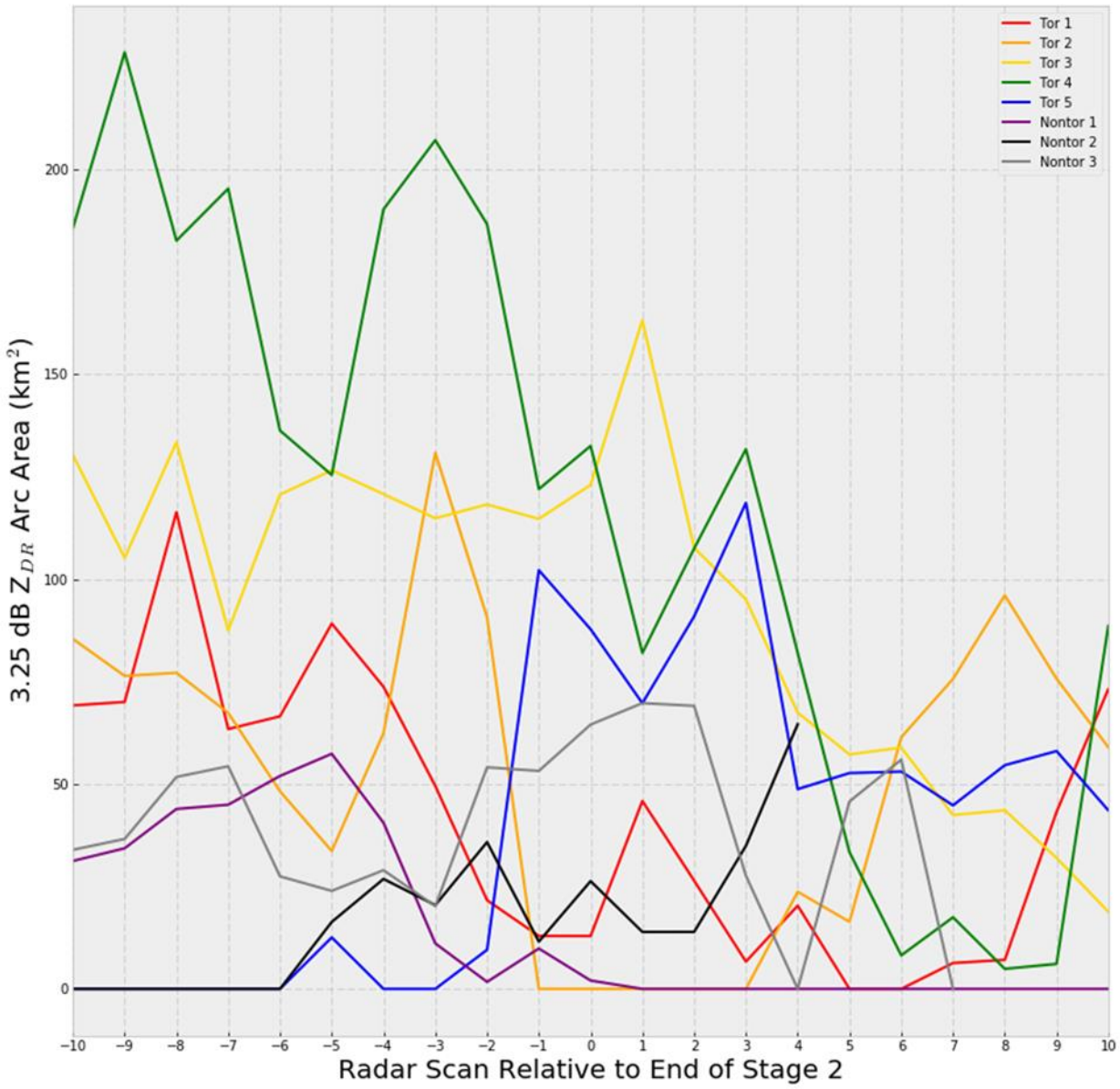

Figure 4.34: As in figure 4.33, except relative to the end of occlusion stage 2.

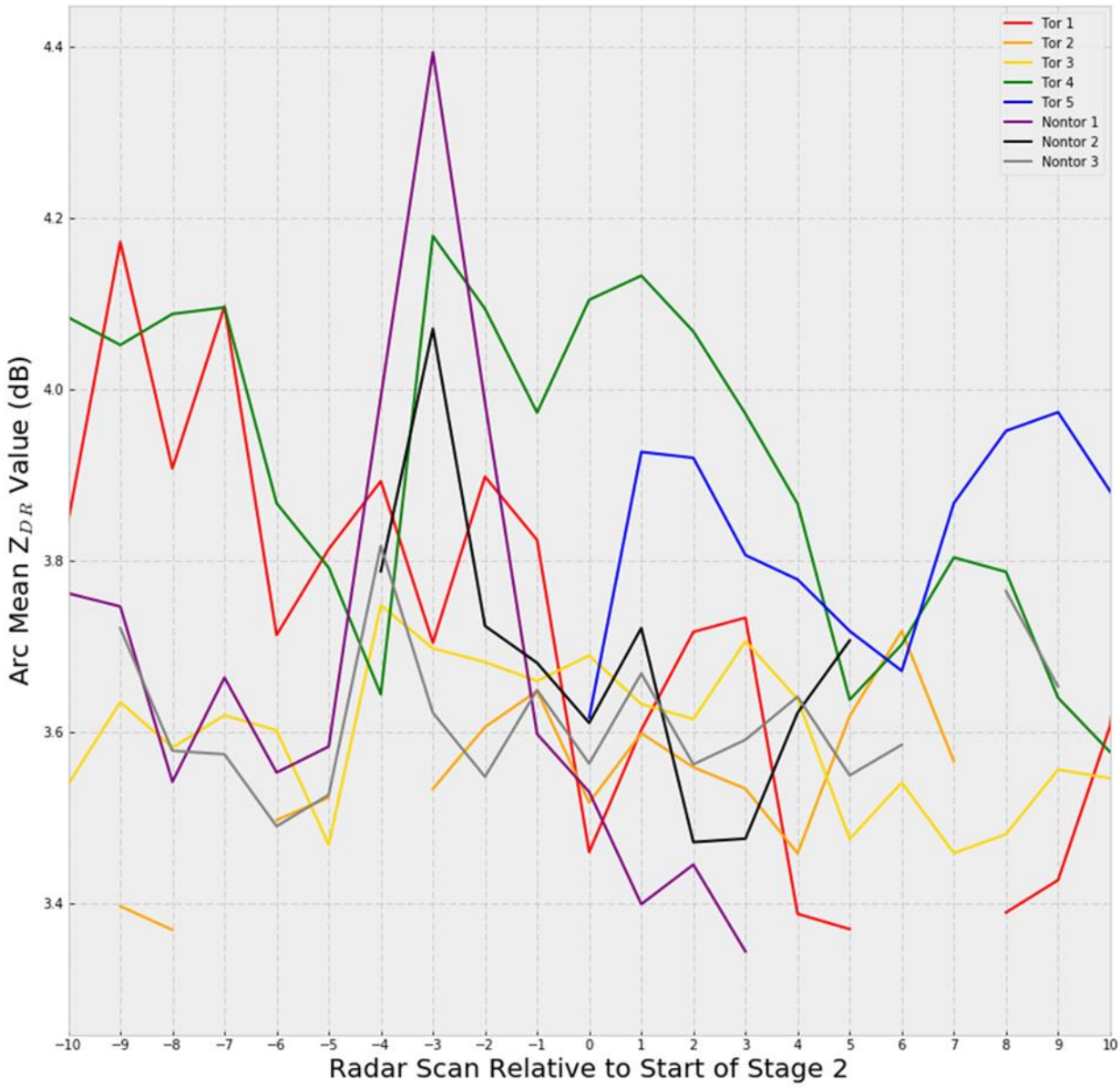

Figure 4.35: As in figure 4.33, except for arc mean Z_{DR} value instead of arc area.

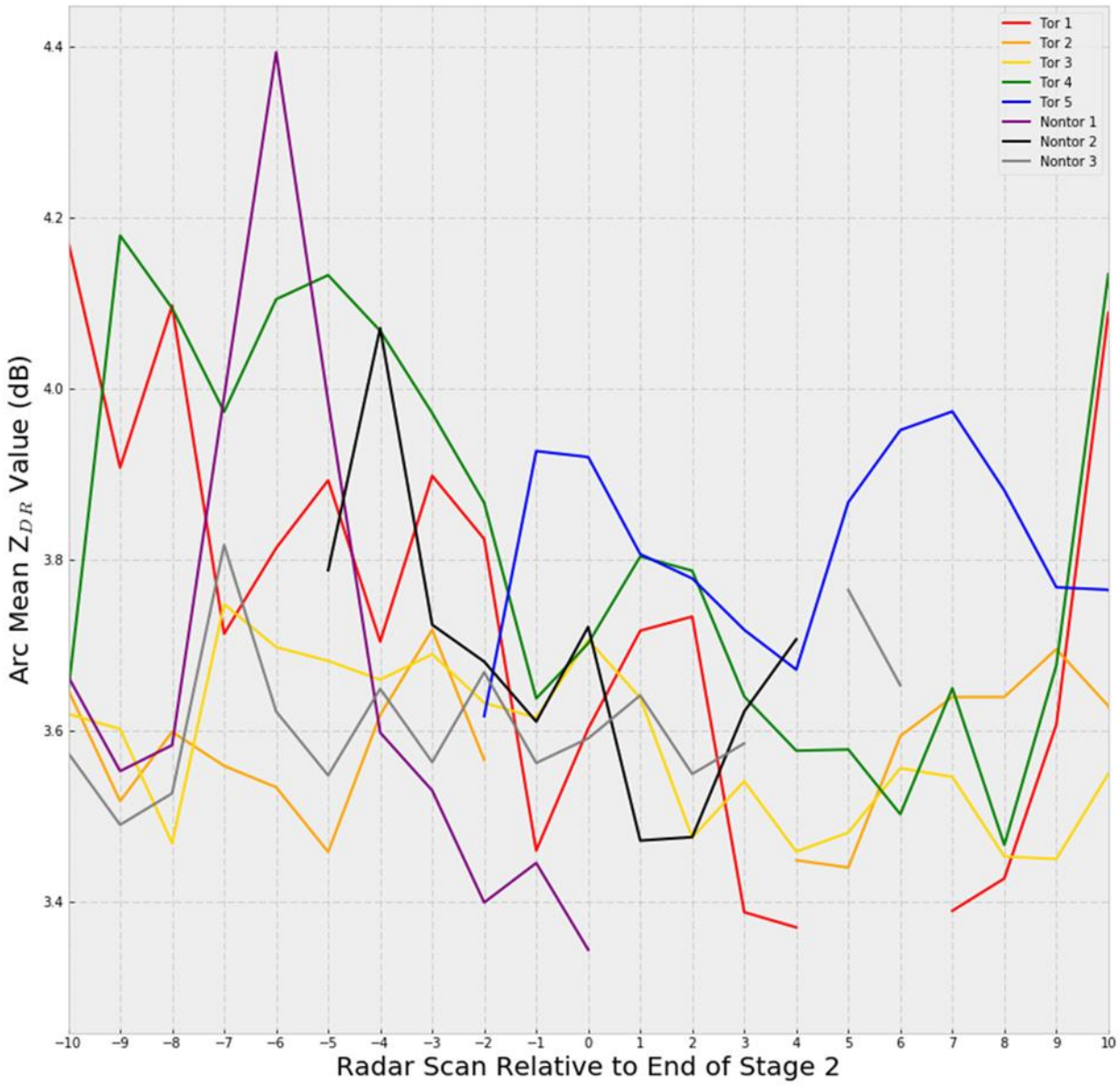

Figure 4.36: As in figure 4.35, except relative to the end of occlusion stage 2.

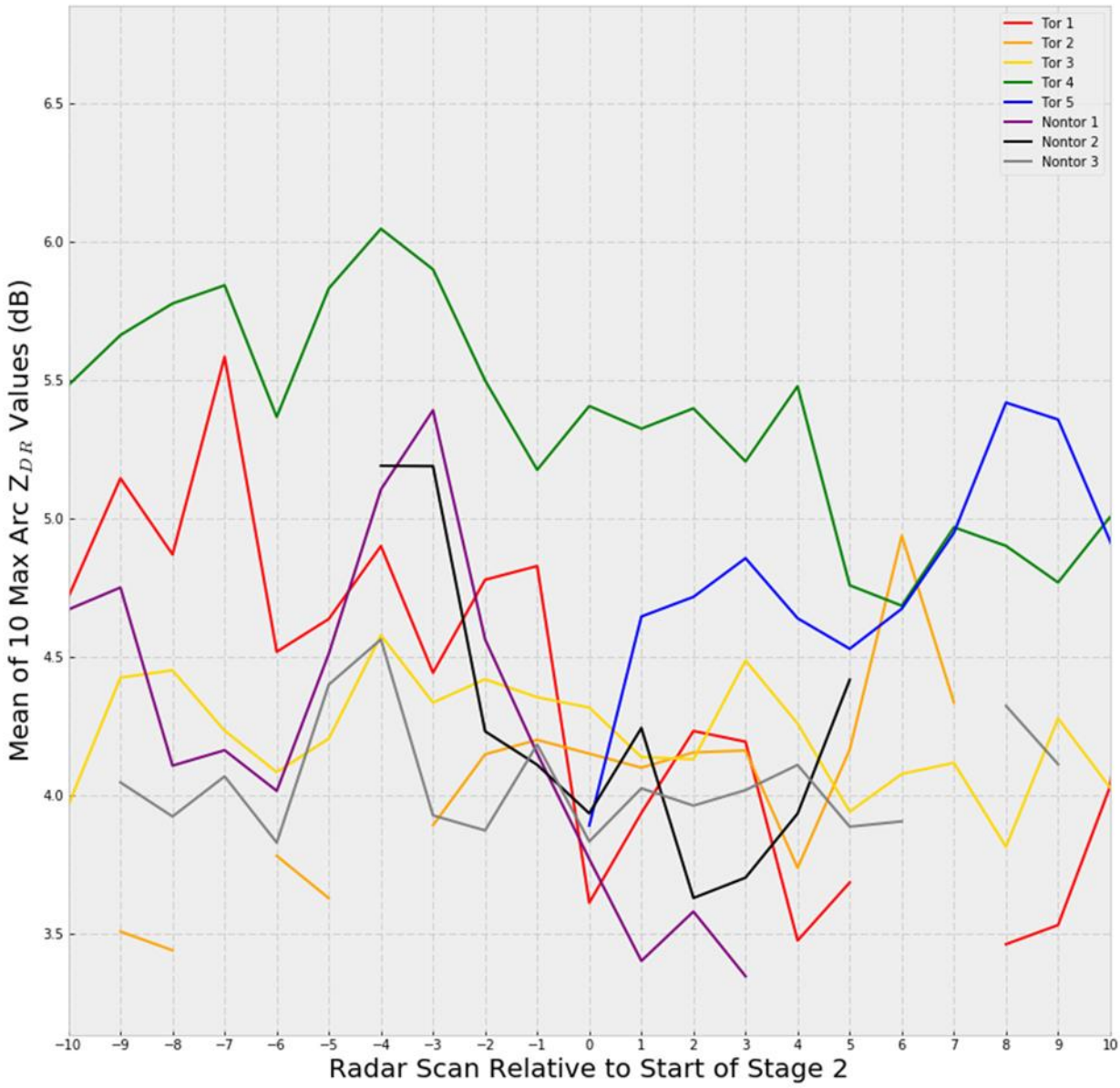

4.37: As in figure 4.33, except for the mean of the 10 maximum arc pixels instead of arc area.

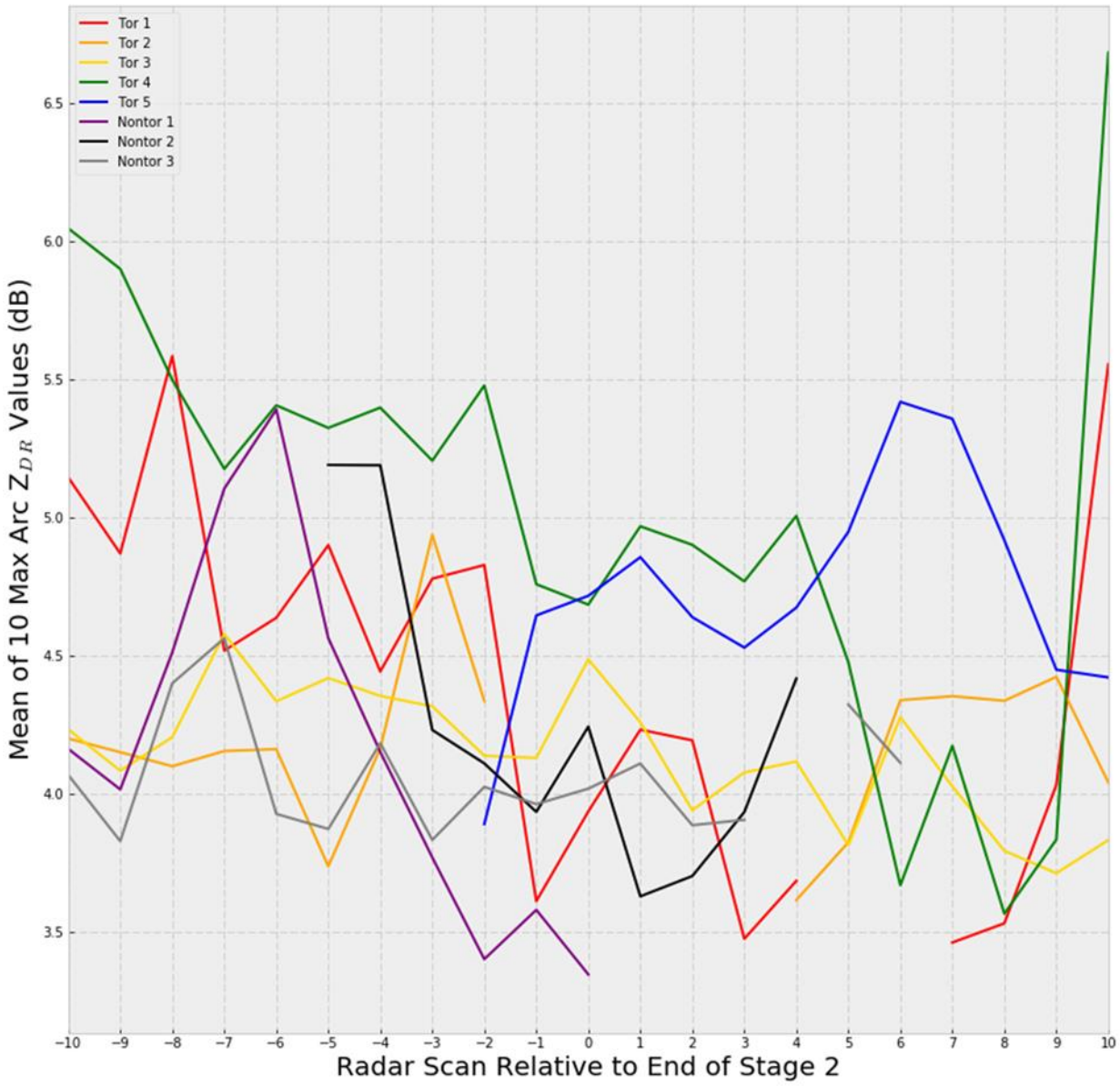

Figure 4.38: As in figure 4.37, except relative to the end of occlusion stage 2.

IV. K_{DP}-Z_{DR} Separation Analysis

According to the results of Loeffler and Kumjian (2018) and Jurewicz et al. (2018), the angle between the K_{DP}-Z_{DR} separation vector and storm motion vector should

generally be larger in tornadic storms and in environments with stronger low-level SRH. To examine whether these hypotheses hold for the supercell dataset examined in this study, separation angles were calculated for all 109 supercells as described in section 3.5. Time steps and storms for which a separation angle could not be calculated due to the absence of an algorithm-identified Z_{DR} arc or K_{DP} foot were set to NaNs. One nontornadic storm had to be removed from the dataset due to the absence of any algorithm-identified K_{DP} foot signatures, resulting in a dataset of 108 storms. In this analysis, tornadic storms had a significantly larger ($p = 0.000540$ using predicted storm motion or $p = 0.000178$ using observed motion) mean separation angle than nontornadic storms (figures 4.39 and 4.40). The magnitude of the difference in separation angles between the tornadic and nontornadic storms, with the tornadic mean close to 55 degrees and the nontornadic mean around 20 degrees, suggests that this difference may be of use in operations. Separation angles also tended to increase with larger surface-1 km shear and surface-1 km SRH, with the correlations being fairly similar whether observed or predicted storm motions are used (figures 4.41 through 4.44). Separation vector length and direction were also plotted against the speed and direction of the storm-relative wind in the 1-3 km and 2-4 km layers, with a moderate correlation found between separation vector direction and storm-relative wind direction (figure 4.45, only 1-3 km layer shown) and no significant correlation found between separation vector length and storm-relative wind speed (figure 4.46).

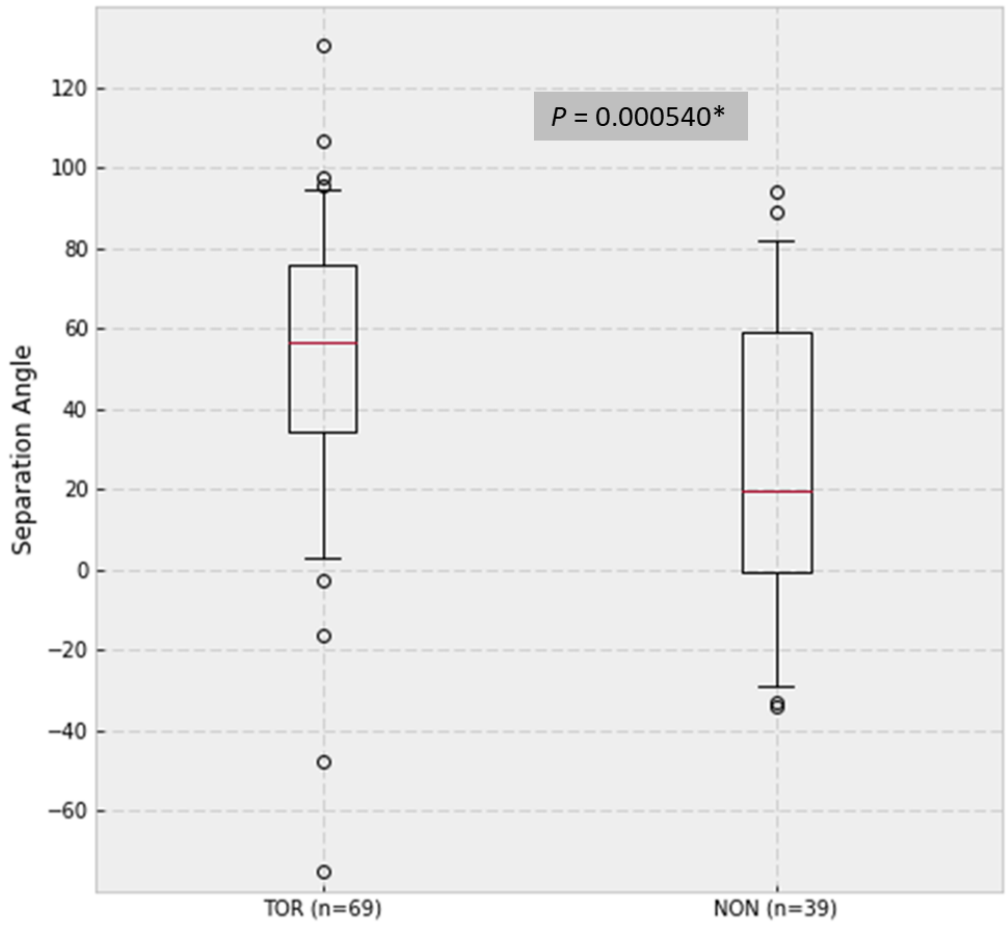

Figure 4.39: Box-and-whisker plot of separation angles for the tornadic and nontornadic supercell datasets. Separation angles are here calculated using predicted storm motions. Boxplots are formatted as in figure 4.27.

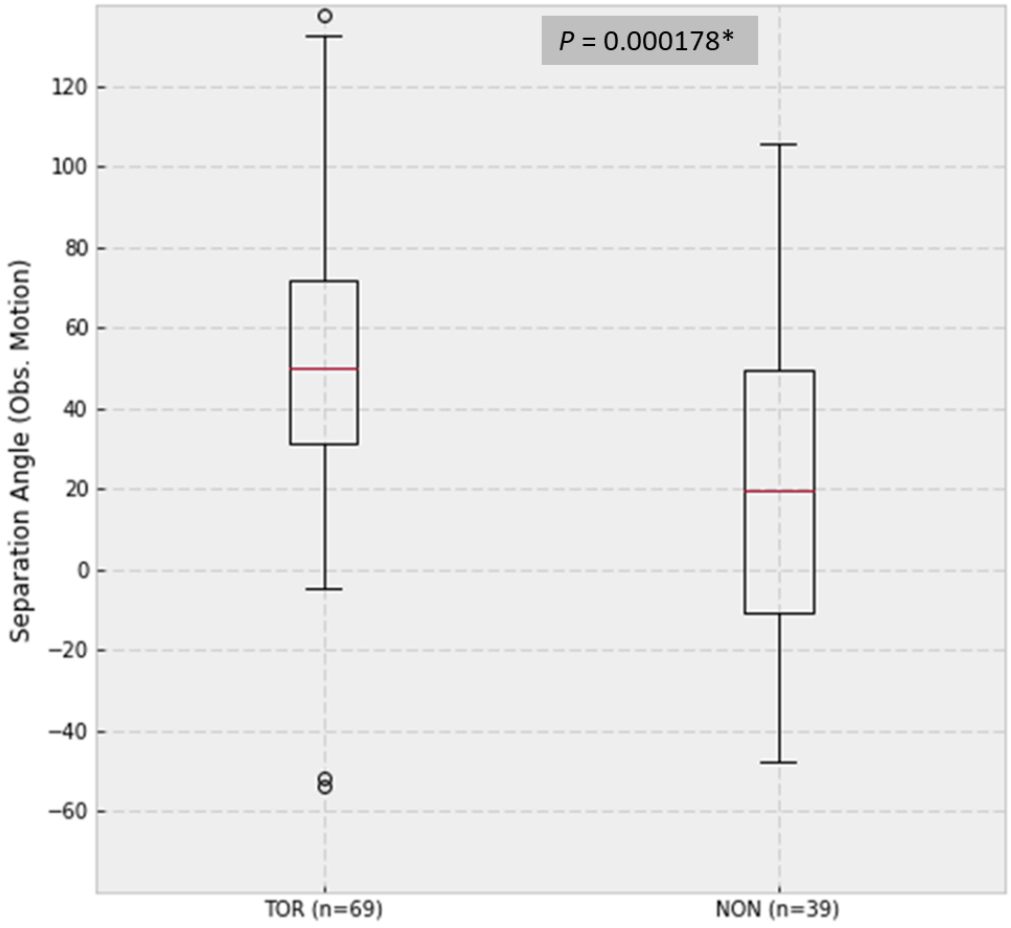

Figure 4.40: As in figure 4.39, except separation angles are calculated using observed storm motions. Boxplots are formatted as in figure 4.27.

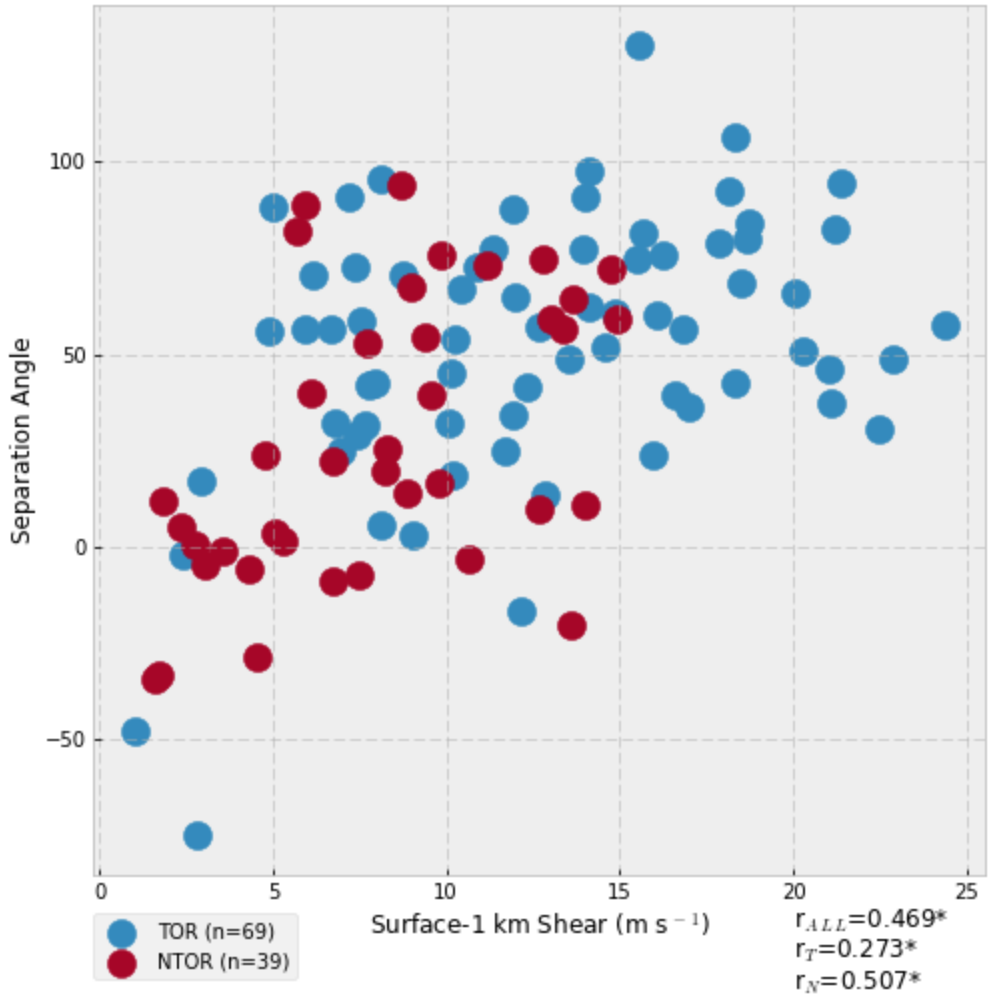

Figure 4.41: Scatterplot of separation angles and surface-1km shear, with the separation angles calculated using predicted storm motions. Correlations at the bottom right are statistically significant at $p < 0.05$ if followed by an asterisk.

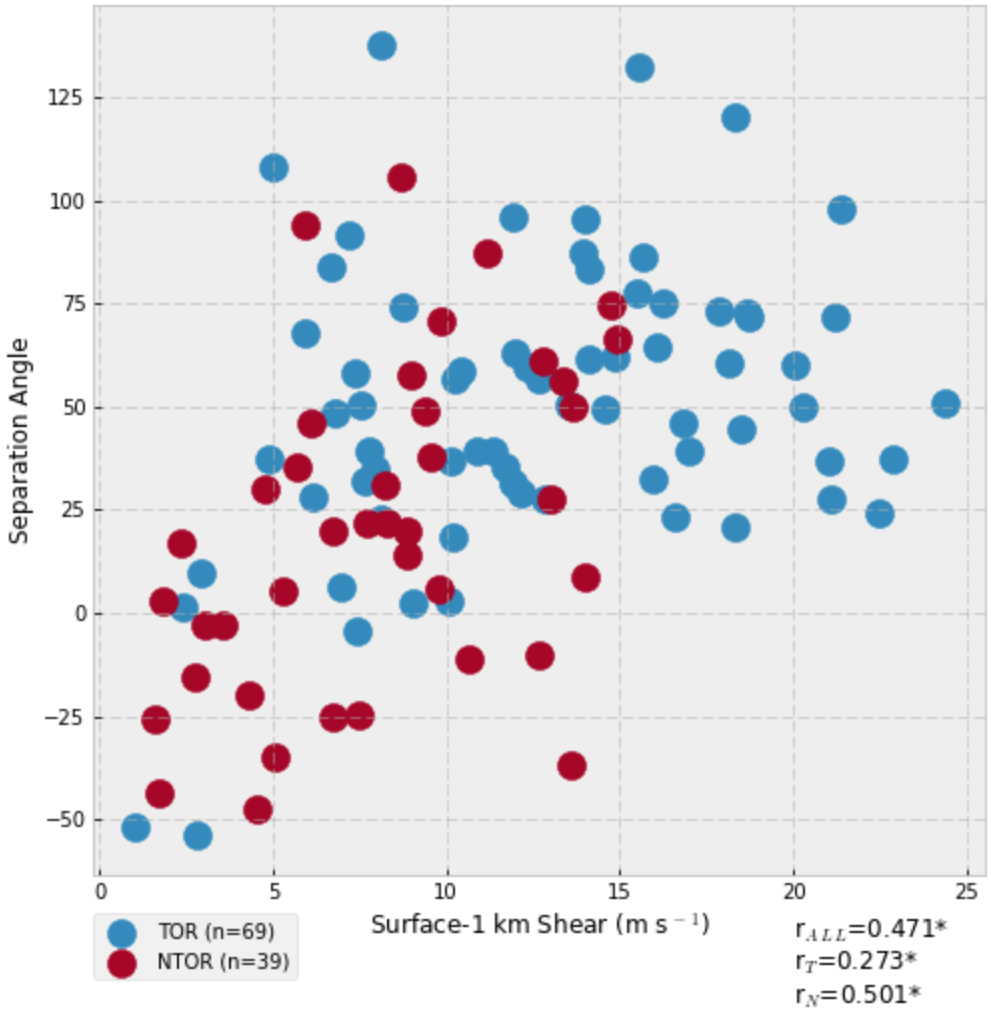

Figure 4.42: As in figure 4.41, except with separation angles are calculated using observed storm motions.

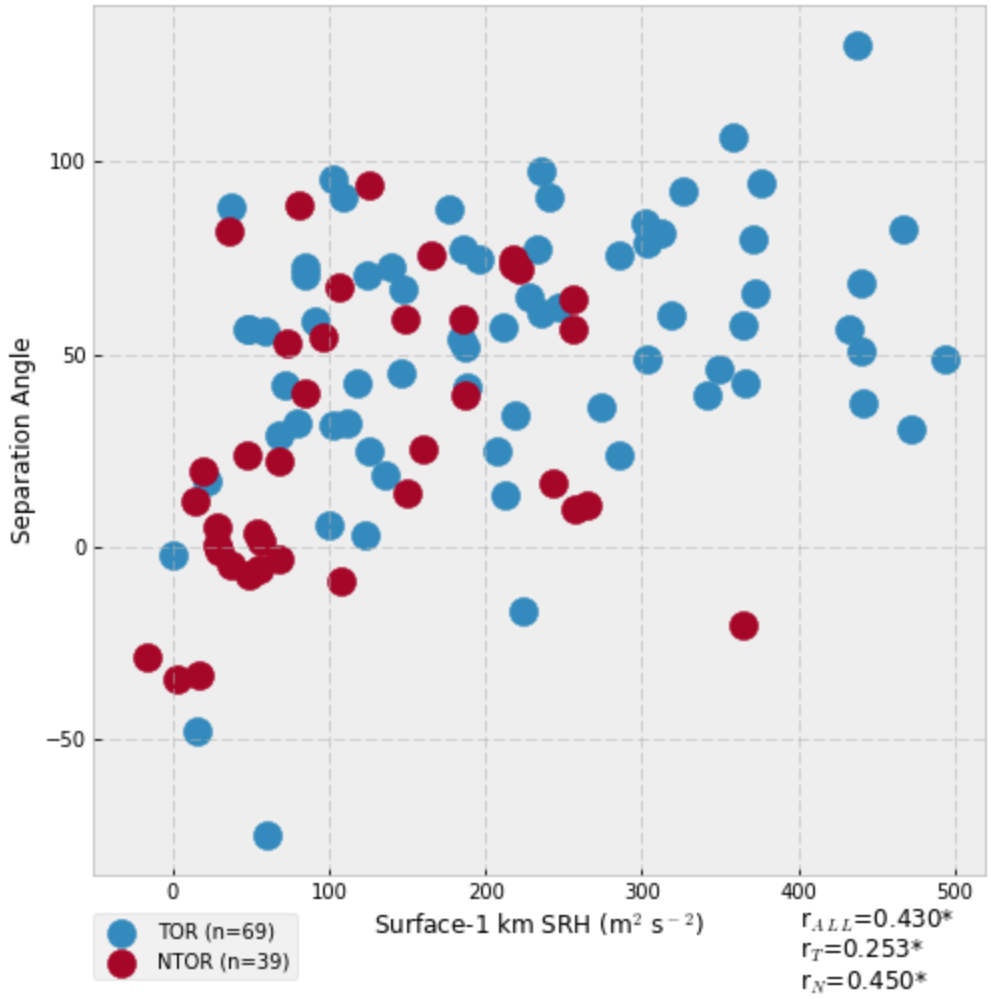

Figure 4.43: Scatterplot of separation angles and surface-1km SRH, with the separation angles and SRH calculated using predicted storm motions. Correlations at the bottom right are statistically significant at $p < 0.05$ if followed by an asterisk.

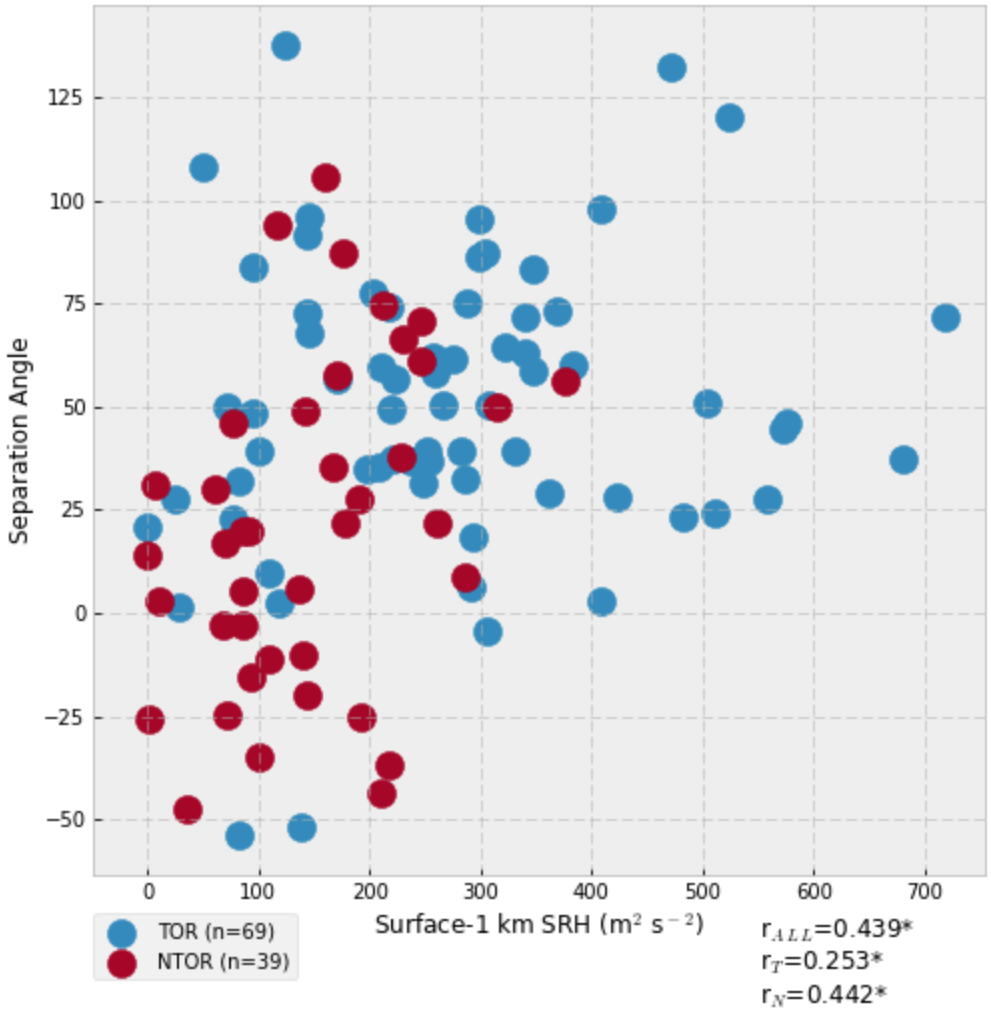

Figure 4.44: As in figure 4.43, except with separation angles and surface-1 km SRH calculated using observed storm motions.

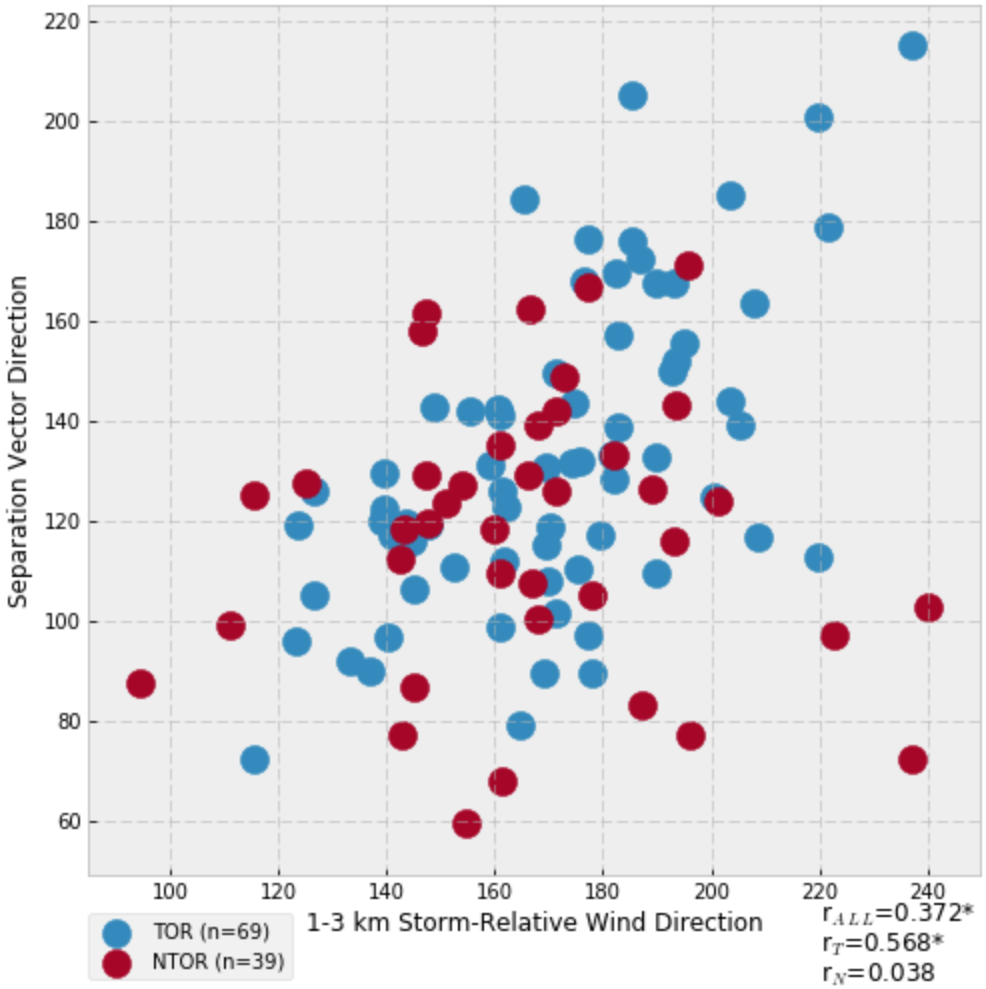

Figure 4.45: Scatterplot of separation vector directions and 1-3 km storm-relative wind directions, with both calculated using predicted storm motions. Correlations at the bottom right are statistically significant at $p < 0.05$ if followed by an asterisk

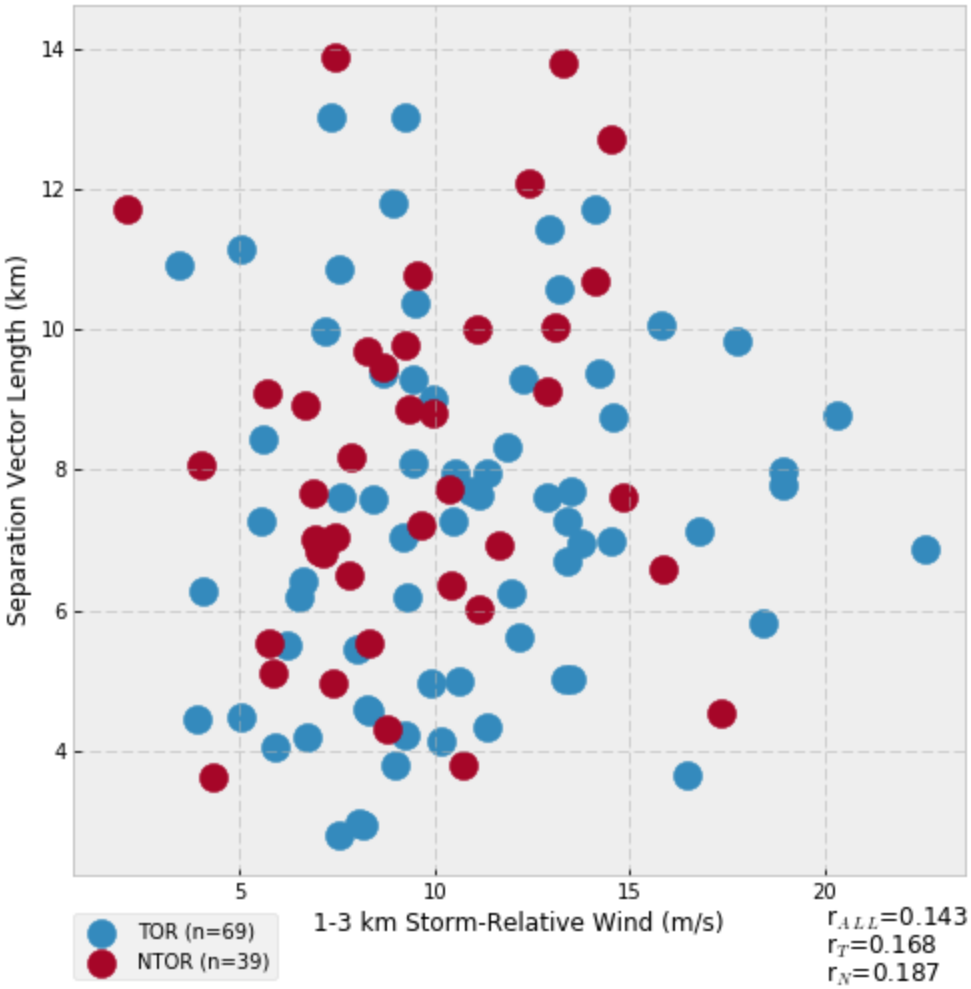

Figure 4.46: Scatterplot of separation vector length and 1-3 km storm-relative wind speed, with both calculated using predicted storm motions. Correlations at the bottom right are statistically significant at $p < 0.05$ if followed by an asterisk.

Chapter V: Discussion

I. Environmental Controls on Arc Characteristics

The results indicate that Z_{DR} arc characteristics are most strongly affected by the amount of instability available to a supercell and the mid- to low-level RH in the near-storm environment. Arcs were found to generally be larger and more intense in environments with greater instability (figures 4.2 and 4.3), arcs tended to be smaller in environments with higher 3-6 km mean relative humidity (figure 4.4), and arcs increased in intensity with lower 1 km relative humidity (figures 4.5 and 4.6). Although none of these relationships was particularly strong, with no correlations with $r > 0.5$ found when using the full dataset, these results do match those found in prior work with a smaller sample of supercells (VDB16). As noted by VDB16, the increase in arc size with higher MLCAPE is likely due to higher supersaturations in stronger updrafts in high-instability environments producing more large drops which then fall into the arc region, which skews the drop-size distribution towards larger drops and helps enhance Z_{DR} in that area before size sorting by the storm-relative wind enhances it further. A similar hypothesis likely explains the relationship between lower mid- and low-level RH and larger and more intense arcs, with preferential evaporation of small drops as hypothesized by Kumjian and Ryzhkov (2008b) skewing the drop-size distribution toward larger drops and raising Z_{DR} in the arc region. The observed weak correlation between higher LCLs and larger, stronger arcs may also be a product of preferential evaporation of smaller drops below cloud base.

Low-level shear and SRH parameters were generally found to have weak negative correlations with arc size and intensity, with a slight tendency for arcs to be smaller and

less intense in environments with higher surface-1 km shear and surface-1 km SRH (figures 4.13-4.16). In addition, the storm-relative winds in two layers above the arc (1-3 km AGL and 2-4 km AGL) were found to be essentially unrelated to arc size and intensity (figures 4.17-4.19). Since prior idealized modelling studies of Z_{DR} arc signatures (Kumjian and Ryzhkov 2009; Dawson et al. 2014a,b) have shown that the enhanced Z_{DR} in the arc region is due to drop size sorting by the storm-relative wind and found that Z_{DR} values in the arc should be higher in environments with stronger storm-relative flow in the layer just above the arc along with stronger low-level shear and SRH, these results were unexpected. Possible explanations for the lack of correlation between arc size and intensity and storm-relative wind magnitude in the layer above the arc may include:

1. Variation in arc size and intensity due to other environmental factors, such as MLCAPE and mid-to-low level RH, is larger than the signal from the storm-relative wind magnitude and obscures it.
2. Storm-induced modifications to the wind field could play a role in enhancing drop-size sorting in the arc region and may be a primary control of arc size and intensity.
3. The arc metrics used in this study (the area of the 3.25 dB Z_{DR} arc, the mean Z_{DR} value in the arc, and the mean of the 10 highest Z_{DR} values in the arc) are not good proxies for the degree of drop-size sorting in the arc region, possibly due to sensitivity to the initial drop-size distribution which enters the region above the arc where size sorting occurs.

Further investigation of these unexpected results is likely warranted and could include simulating supercells using a wide range of different environmental parameters

and extracting simulated dual-pol signatures. This would allow a careful examination of how Z_{DR} arcs respond to changes in environmental parameters in a more controlled manner than is possible using observed supercells and RAP soundings and could also shed light on the role of storm-induced perturbations to the wind field in generating the arc.

II. Arc Characteristics and Low-Level Rotation

In a sample of 50 storms drawn from the dataset used to train the Z_{DR} arc algorithm in this study, arc areal extent was found to have no statistically significant relationships with low-level rotational velocity or NROT at time lags of up to 3 radar scans (figures 4.26 and 4.27, table 4.1). Both arc intensity metrics exhibited statistically significant negative correlations with low-level rotation, with the strongest correlations being between mean intensity and rotation metrics for each storm; however, correlations were still generally weak to moderate with a lot of scatter (figures 4.22 through 4.25). Moreover, these relationships generally became weaker with increasing lag time (table 4.1). Thus, the results of this study differ from the hypothesis posed by Kumjian and Ryzhkov (2009) that an increase in arc size and intensity could be used to anticipate the strengthening of low-level rotation in a supercell due to its movement into a higher-SRH environment, since this analysis has found that arc metrics overall tend to have relatively weak, negative correlations with both SRH and low-level rotation. It is possible that storms with stronger low-level rotation tend to have less intense Z_{DR} arcs in part because they are in environments with higher SRH; however, the weakness of the correlations found in this study and the multitude of other environmental variables which could affect arc intensity make any connection tenuous at best. Further exploration of how low-level

rotation, arc metrics, and environmental parameters are related in time and as storm averages using simulated supercells as suggested in section 5.1 may thus be useful. It is also possible that any positive relationship between arc metrics, mesoscale variations in SRH, and low-level rotation occurs on timescales longer than the 3-radar-scan lag which was the maximum examined here, and a dataset with more supercells for which longer time series of arc metrics and low-level rotation metrics are available would be needed to properly examine this question.

III. Tornadic-Nontornadic Comparison and Arc Changes in Tornadogenesis, Tornadogenesis Failure, and Mesocyclone Cycling

Arc characteristics in tornadic and nontornadic storms were generally found to be similar, with only a slight, non-statistically-significant increase in arc size and intensity metrics in nontornadic storms which is probably not readily detectable in operations (figures 4.28 through 4.30). This result makes sense given that many of the environmental variables which were found to be most important in controlling arc size and intensity (MLCAPE, low- and mid- level relative humidity) are not necessarily those which prior studies have found to be most important in determining whether a storm will produce a tornado or not, such as surface-1 km shear and SRH (Thompson et al. 2003; Esterheld and Giuliano 2008). Thus, arc size and intensity are likely not particularly useful in differentiating between tornadic and nontornadic supercells.

Although arc characteristics were not found to be meaningfully different between tornadic and nontornadic storms, an analysis of time series of arc characteristics prior to tornadogenesis in 22 tornadic supercells found a noticeable jump in mean and median arc areal extent centered around 5 radar scans before tornado formation (figures 4.31 and

4.32). A similar jump was found in nontornadic storms prior to tornadogenesis failure (defined here as the time of peak NROT for that storm), and this jump remained in both datasets when Z_{DR} arc areas were normalized by the area of the parent supercell (figures 4.31 and 4.32). This increase may be large enough to be noticeable in operations, with median arc areas increasing from around 25 km^2 at 8 and 9 scans prior to tornadogenesis success (or failure in nontornadic storms) to around 50 km^2 at 1 and 2 scans prior to that time. This result initially seems to contradict the lack of correlation between time series of low-level rotation and arc area discussed earlier, and several possible reasons for this difference may exist. Firstly, the analysis discussed in section 2 of this chapter used data from radars scanning in a non-SAILS mode with updates every ~5 minutes, while this time series analysis used data from radars in SAILS mode with low-level scans every 2 to 3 minutes. Thus, the higher temporal resolution of this data may have better captured changes not apparent in the non-SAILS dataset. Secondly, the inclusion of nontornadic supercells which did not develop any significant rotation in the dataset used in section 2 may have produced noise which could have masked any signal coming from the supercells which did develop substantial low-level rotation. Finally, many of the time series used in section 2 are relatively short, and the limited number of data points available for those storms may have limited the usefulness of that analysis. To better answer the question of whether an increase in Z_{DR} arc areal extent can be a reliable precursor to tornadogenesis or the development of a strong low-level rotation peak, this analysis should be extended by using a much larger sample of tornadic and nontornadic supercells.

A similar sample-size issue likely affects the analysis of arc characteristics during mesocyclone occlusion presented in section 4.3. Although overall slight decreases in arc intensity were found in many of the storms analyzed just before and during mesocyclone occlusion, trends vary substantially between storms and a consistent signal was difficult to discern in the small sample of 8 storms. Thus, an analysis of trends in arc characteristics during mesocyclone occlusion in a larger sample of supercells is still needed to determine whether the decreases in arc size and intensity during occlusion noted in case studies by Kumjian et al. (2010) and Palmer et al. (2011) are prevalent in supercells in general. This question could also be approached using high-resolution simulations of supercells, where the exact timing of occlusion might be more readily determined than in operational radar data.

IV. K_{DP}-Z_{DR} Separation Analysis

The angle between the K_{DR}-Z_{DR} separation vector and the storm motion vector (figure 2.5) was found to generally increase with larger values of surface-1 km shear and SRH (figures 4.39 and 4.41). Although the correlations between the separation angle and low-level shear and SRH were moderate, they were still some of the highest found in this study and only weakened slightly when using observed storm motions instead of predicted motions (figures 4.40 and 4.42). Moreover, a substantial, statistically significant difference existed between the median separation angle in tornadic storms (~55 deg) and the median separation angle in nontornadic storms (~20 deg). This difference may be due to the separation angle's correlation with low-level shear and SRH, which previous work has found tend to be higher in tornadic environments (Thompson et al. 2003, Esterheld and Giuliano 2008). Although much overlap still exists

between tornadic and nontornadic separation angle populations, this difference is large enough to suggest that it has the potential to be operationally useful. The results presented here match well with the results of Loeffler and Kumjian (2018), who found evidence of a correlation between more orthogonal separation angles in nonsupercell tornadic storms. They are also consistent with the qualitative assessment of storm-scale SRH using the separation vector presented in Jurewicz et al. (2018), since a larger separation angle should produce a larger area on their diagram for assessing SRH assuming an unchanged separation vector magnitude (figure 2.5). Future work could focus on incorporating something similar to the Jurewicz et al. (2018) SRH assessment into the automated Z_{DR} arc algorithm and analyzing its relationship to near-storm SRH derived from RAP soundings.

V. Algorithm Limitations

Although the automated Z_{DR} arc detection and tracking algorithm used in this study and described in detail in chapter 2 performs well with most of the supercells in the dataset used to test it (figure 3.5) and qualitatively appeared to capture the extent of the Z_{DR} arc well in most of the rest of the 109-supercell dataset, some recurrent biases and limitations of the algorithm did become evident. Storms with large amounts of high-Z_{DR} pixels in their rear flank downdraft regions would occasionally have erroneous arc detections there, and these became particularly difficult to remove in cases where the region of high Z_{DR} in the arc was continuous with high Z_{DR} values in the storm's rear. Since the algorithm identified possible arc objects by breaking a contour of quality-controlled Z_{DR} at 3.25 dB into polygons and eliminates erroneous polygons with a random forest classifier, a polygon that contains both an actual arc and a spurious arc

detection on the storm's rear flank results in either an excessively large arc area if it is classified as an arc or a small or missing arc if it is classified as a non-arc area of high Z_{DR}. The algorithm also relies on a relatively rudimentary storm tracking algorithm to produce storm objects to which potential arc objects are assigned, and a missed or incorrectly tracked storm can occasionally cause arc objects to be lost or assigned to a storm other than the storm they are actually associated with. Arc objects on extremely large storms can also occasionally be missed when the random forest considers their distance from the storm centroid to be too great. Future improvements to the algorithm, including the adoption of an improved storm tracking algorithm and the use of a convolutional neural network (as in Mahesh et al. (2019)) to identify arcs pixel by pixel instead of as polygons from a contour of Z_{DR} may be able to partially mitigate some of these limitations.

Chapter VI: Summary and Conclusions

This study has used an automated Z_{DR} arc detection and tracking algorithm to examine characteristics of Z_{DR} arcs and the separation between areas of enhanced K_{DP} and Z_{DR} in a large sample of supercell storms. Algorithm output from this 109-supercell dataset was used to attempt to answer several questions about what Z_{DR} arc and K_{DR}-Z_{DR} separation characteristics can tell forecasters about supercells and their environments. Principal results from this analysis include that:

- Z_{DR} arcs tend to be larger and more intense in environments with higher MLCAPE, lower RH in the mid- to low-levels, and higher LCLs. This is hypothesized to be due to stronger updrafts with higher supersaturations producing more large drops in high-CAPE environments and drier mid- to low- levels allowing the preferential evaporation of small drops, consistent with the findings of VDB16 and Kumjian and Ryzhkov (2008b).
- In contrast to the results of Kumjian and Ryzhkov (2009), who suggested that Z_{DR} arcs should be stronger in higher-SRH environments, low level shear and SRH were found to have generally weak and often negative correlations with arc size and intensity.
- The magnitude of the storm-relative wind in layers just above the arc (defined here as 1-3 km and 2-4 km) was not found to be related to arc size or intensity. Possible explanations for this result and the lack of a strong correlation between low-level shear and SRH and arc metrics include the possibility that variations in arc area and strength related to thermodynamic and moisture parameters are large enough to mask

variation due to kinematic variables, that modifications to the environmental wind profile by the storm itself could make the RAP soundings used in this study unrepresentative of the wind profile which leads to the size sorting in the arc, and that the arc metrics used here may not be the best measures of the degree of size sorting.

- Z_{DR} arc metrics were not found to be well-correlated with or predictive of changes in low-level rotation magnitude, with storm mean arc intensity displaying a moderate negative correlation with rotational velocity and NROT at lags of up to 3 non-SAILS radar scans (~15 minutes).
- Arc size and intensity were not found to be meaningfully different between tornadic and nontornadic supercells.
- While arc intensity did not display any substantial trends prior to tornadogenesis or tornadogenesis failure, arc areal extent showed a somewhat consistent increase which preceded tornadogenesis success or failure by ~5 radar scans (equivalent to 10-15 minutes in SAILS).
- Arc areal extent showed no consistent trend during storm occlusion cycles, but a slight decrease in arc intensity metrics may be evident just before and during occlusion. This analysis and the analysis of changes in arc metrics leading up to tornadogenesis success or failure are both limited by small sample sizes (8 and 33 storms respectively), and a larger-scale study of both would be useful.
- Separation angles were substantially different between tornadic and nontornadic supercells (~55 deg for tornadic storms compared to ~20 deg

for nontornadic storms) and were positively correlated with low-level shear and SRH. Further work in this area to improve the reliability of the K_{DP}-Z_{DR} separation portion of the Z_{DR} arc detection and tracking algorithm and to incorporate an automated implementation of the Jurewicz and Gitro (2018) storm-scale SRH assessment technique could be beneficial.

This study has three main findings which may be relevant to operations. Firstly, the lack of correlation between arc size and intensity metrics and low-level shear and SRH, as well as the lack of significant differences in these metrics between tornadic and nontornadic storms, may indicate that these Z_{DR} arc metrics may not be of much use in identifying which supercells are most likely to be tornadic. Secondly, the consistent ramp-up in arc areal extent found approximately five scans before tornadogenesis (or peak NROT in nontornadic supercells) may indicate that a storm which experiences a rapid increase in arc area may be one to watch for the subsequent development of intense low-level rotation. Thirdly, the large (~35 degrees) and statistically significant difference in mean separation angles between tornadic and nontornadic storms and the substantial correlations between separation angle and low-level shear and SRH indicates that this parameter could be operationally useful in helping determine which supercells are most likely to be tornadic and how a storm's low-level shear environment may be changing on short timescales. Overall, results from this study should hopefully further inform the use of Z_{DR} arc and K_{DP}-Z_{DR} separation signatures in operations and provide inspiration for further observational and modelling studies of these signatures and their relationship to environmental parameters, tornado production, and mesocyclone cycling. Additionally, it

is hoped that the automated Z_{DR} arc detection and tracking algorithm presented in this study could serve as a framework for the object-based objective investigation of other supercell dual-pol characteristics, such as Z_{DR} column depth and area and the areal coverage of radar-indicated large hail.

References

Adlerman, E. J., K. K. Droegemeier, R. Davies-Jones, 1999: A numerical simulation of cyclic mesocyclogenesis. *J. Atmos. Sci.*, **56**, 2045–2069, doi:10.1175/1520-0469(1999)056<2045:ANSOCM>2.0.CO;2.

——, and K. K. Droegemeier, 2005: The dependence of numerically simulated cyclic mesocyclogenesis upon environmental vertical wind shear. *Mon. Wea. Rev.*, **133**, 3595–3623, doi:10.1175/MWR3039.1.

Beck, J. R., J. L. Schroeder, J. M. Wurman, 2006: High-resolution dual-doppler analyses of the 29 May 2001 Kress, Texas, cyclic supercell. *Mon. Wea. Rev.*, **134**, 3125–3148, doi:10.1175/MWR3246.1.

Blumberg, W. G., K.T. Halpert, T.A. Supinie, P.T. Marsh, R.L Thompson, and J.A. Hart 2017: SHARPpy: An open-source sounding analysis toolkit for the atmospheric sciences. *Bull. Amer. Meteor. Soc.*, **98**, 1625–1636, doi:10.1175/BAMS-D-15-00309.1.

Breiman, L., 2001: *Random Forests*. 5-32 pp. https://link.springer.com/content/pdf/10.1023/A:1010933404324.pdf.

Bunkers, M. J., M. R. Hjelmfelt, and P. L. Smith, 2006: An observational examination of long-lived supercells. part I: Characteristics, evolution, and demise. *Wea. Forecasting.*, **21**, 673–688, doi:10.1175/WAF949.1.

Bunkers, M., D. Barber, R. Thompson, R. Edwards, and J. Garner, 2014: Choosing a universal mean wind for supercell motion prediction. *J. Oper. Meteorol.*, **2**, 115–

129, doi:10.15191/nwajom.2014.0211.

Coffer, B. E. and M. D. Parker, 2017: Simulated supercells in nontornadic and tornadic VORTEX2 environments. *Mon. Wea. Rev.*, **145**, 149–180, doi:10.1175/MWR-D-16-0226.1.

Cooper, D.T and A. B Vorst, 2016: Assessing the utility of normalized rotation in detecting tornado development along the allegheny front. *Northeast Regional Operational Workshop XVII*, Albany, NY

Crowe, C., C. Schultz, M. Kumjian, L. Carey, and W. Petersen, 2012: Use of dual-polarization signatures in diagnosing tornadic potential. *Electron. J. Oper. Meteorol.*, **13**, 57–78.

Crowe, C. C., W. A. Petersen, L. D. Carey, and D. J. Cecil, 2010: A dual-polarization investigation of tornado-warned cells associated with Hurricane Rita (2005). *Electron. J. Oper. Meteorol.*, **4**, 1–25.

Davies-Jones, R., 2015: A review of supercell and tornado dynamics. *Atmos. Res.*, **158**–**159**, 274–291, doi:10.1016/j.atmosres.2014.04.007.

——, 1984: Streamwise vorticity: The origin of updraft rotation in supercell storms. *J. Atmos. Sci.*, **41**, 2991–3006, doi:10.1175/1520-0469(1984)041<2991:SVTOOU>2.0.CO;2.

Dawson, D. T., E. R. Mansell, Y. Jung, L. J. Wicker, M. R. Kumjian, and M. Xue, 2014a: Low-level Z_{DR} signatures in supercell forward flanks: The role of size sorting and melting of hail. *J. Atmos. Sci.*, **71**, 276–299, doi:10.1175/JAS-D-13-0118.1.

Dawson, D. T., E. R. Mansell, and M. R. Kumjian, 2014b: Does wind shear cause hydrometeor size sorting? *J. Atmos. Sci.*, **72**, 340–348, doi:10.1175/JAS-D-14-0084.1.

Dowell, D. C. and H. B. Bluestein, 2002: The 8 June 1995 McLean, Texas, storm. part I: Observations of cyclic tornadogenesis. *Mon. Wea. Rev.*, **130**, 2626–2648, doi:10.1175/1520-0493(2002)130<2626:TJMTSP>2.0.CO;2.

Duda, J. D. and W. A. Gallus, 2010: Spring and summer midwestern severe weather reports in supercells compared to other morphologies. *Wea. Forecasting.*, **25**, 190–206, doi:10.1175/2009WAF2222338.1.

Edwards, R., A. R. Dean, R. L. Thompson, and B. T. Smith, Convective modes for significant severe thunderstorms in the contiguous United States. part III: Tropical cyclone tornadoes. *Wea. Forecasting.* doi:10.1175/WAF-D-11-00117.1.

Gibson, M., 2017: FAQ: NROT and GR-MDA Products. *GRlevelx User Forums*.

Esterheld, J. M., and D. J. Giuliano, 2008: Discriminating between tornadic and non-tornadic supercells: A new hodograph technique. *E-Journal Sev. Storms Meteorol.*, **3**, 1–50. http://www.ejssm.org/ojs/index.php/ejssm/article/view/33/37.

Haberlie, A. M., and W. S. Ashley, 2018: A method for identifying midlatitude mesoscale convective systems in radar mosaics. part I: Segmentation and classification. *J. Appl. Meteor. Climatol.*, **57**, 1575–1598, doi:10.1175/JAMC-D-17-0293.1.

Helmus, J. J., and S. M. Collis, 2016: The python ARM radar toolkit (Py-ART), a library

for working with weather radar data in the python programming language. *J. Open Res. Softw.*, **4**, doi:10.5334/jors.119.

Herman, G. R., and R. S. Schumacher, 2018: Money doesn't grow on trees, but forecasts do: Forecasting extreme precipitation with random forests. *Mon. Wea. Rev.*, **146**, 1571–1600, doi:10.1175/MWR-D-17-0250.1.

Houston, A. L., R. L. Thompson and R. Edwards, 2008: The optimal bulk wind differential depth and the utility of the upper-tropospheric storm-relative flow for forecasting supercells. *Wea. Forecasting.*, **23**, 825–837, doi:10.1175/2008WAF2007007.1.

Jurewicz, M.L. and C. M. Gitro, 2018: Incorporating dual-polarization signatures into the tornado warning process: K_{DP}/Z_{DR} separation signals, Z_{DR} arc considerations, and initial results of hook echo investigations. *98th Amer. Meteor. Soc. Annual Meeting,* Austin, TX, 12B.2

Kumjian, M. R., and A. V. Ryzhkov, 2008a: Polarimetric signatures in supercell thunderstorms. *J. Appl. Meteor. Climatol.*, **47**, 1940–1961, doi:10.1175/2007JAMC1874.1.

Kumjian, M., and A. Ryzhkov, 2008b: Microphysical differences between tornadic and nontornadic supercell rear-flank downdrafts revealed by dual-polarization radar measurements. 24th Conf. on Severe Local Storms, Savannah, GA, Amer. Meteor. Soc., 3B.4

——, and ——, 2009: Storm-relative helicity revealed from polarimetric radar measurements. *J. Atmos. Sci.*, **66**, 667–685, doi:10.1175/2008JAS2815.1.

——, ——, V. M. Melnikov, and T. J. Schuur, 2010: Rapid-scan super-resolution observations of a cyclic supercell with a dual-polarization WSR-88D. *Mon. Wea. Rev.*, **138**, 3762–3786, doi:10.1175/2010MWR3322.1.

——, A. P. Khain, N. Benmoshe, E. Ilotoviz, A. V. Ryzhkov, and V. T. J. Phillips, 2014: The anatomy and physics of Z_{DR} columns: Investigating a polarimetric radar signature with a spectral bin microphysical model. *J. Appl. Meteor. Climatol.*, **53**, 1820–1843, doi:10.1175/JAMC-D-13-0354.1.

Lemon, L. R. and C. A. Doswell, 1979: Severe thunderstorm evolution and mesocyclone structure as related to tornadogenesis. *Mon. Wea. Rev.*, **107**, 1184–1197, doi:10.1175/1520-0493(1979)107<1184:STEAMS>2.0.CO;2.

Loeffler, S. D. and M. R. Kumjian, 2018: Quantifying the separation of enhanced Z_{DR} and K_{DP} regions in nonsupercell tornadic storms. *Wea. Forecasting.*, **33**, 1143–1157, doi:10.1175/WAF-D-18-0011.1.

Mahesh, A, T. O'Brien, W. Collins, M. Prabhat, K. Kashinath, M. Mudigonda, 2019: Probabalistic detection of extreme weather using deep learning methods. *99th Amer. Meteor. Soc. Annual Meeting*, Phoenix, AZ, 3A.2

Markowski, P., Y. Richardson, E. Rasmussen, J. Straka, R. Davies-Jones, and R. J. Trapp, 2008: Vortex lines within low-level mesocyclones obtained from pseudo-dual-doppler radar observations. *Mon. Wea. Rev.*, **136**, 3513–3535, doi:10.1175/2008MWR2315.1.

Markowski, P., and Y. Richardson, 2010: Mesoscale meteorology in midlatitudes. Wiley-Blackwell, Chichester.

——, J. M. Straka, and E. N. Rasmussen, 2002: Direct surface thermodynamic observations within the rear-flank downdrafts of nontornadic and tornadic supercells. *Mon. Wea. Rev.*, **130**, 1692–1721, doi:10.1175/1520-0493(2002)130<1692:DSTOWT>2.0.CO;2..

Martinaitis, S. M., 2017: Radar observations of tornado-warned convection associated with tropical cyclones over Florida. *Wea. Forecasting.*, **32**, 165–186, doi:10.1175/WAF-D-16-0105.1.

May, R. M., Arms, S. C., Marsh, P., Bruning, E. and Leeman, J. R., 2017: MetPy: A Python package for meteorological data. Unidata, Accessed 31 March 2017. [Available online at https://github.com/Unidata/MetPy.] doi:10.5065/D6WW7G29.

Mecikalski, J. R., and Coauthors, 2015: Probabilistic 0–1-h convective initiation nowcasts that combine geostationary satellite observations and numerical weather prediction model data. *J. Appl. Meteor. Climatol.*, **54**, 1039–1059, doi:10.1175/JAMC-D-14-0129.1.

Moller, A. R., C. A. Doswell, M. P. Foster, and G. R. Woodall, 1994: The Operational recognition of supercell thunderstorm environments and storm structures. *Wea. Forecasting.*, **9**, 327–347, doi:10.1175/1520-0434(1994)009<0327:TOROST>2.0.CO;2.

Orf, L., R. Wilhelmson, B. Lee, C. Finley, and A. Houston, 2017: Evolution of a long-track violent tornado within a simulated supercell. *Bull. Amer. Meteor. Soc.*, **98**, 45–68, doi:10.1175/BAMS-D-15-00073.1.

Palmer, R. D., D. Bodine, M. Kumjian, B. Cheong, G. Zhang, Q. Cao, H. Bluestein, A. Ryzhkov, T. Yu, and Y. Wang, 2011: Observations of the 10 May 2010 tornado outbreak using OU-PRIME: Potential for new science with high-resolution polarimetric radar. *Bull. Amer. Meteor. Soc.*, **92**, 871–891, doi:10.1175/2011BAMS3125.1.

Parker, M. D., 2014: Composite VORTEX2 supercell environments from near-storm soundings. *Mon. Wea. Rev.*, **142**, 508–529, doi:10.1175/mwr-d-13-00167.1.

Pedregosa, F., G. Varoquaux, A. Gramfort, V. Michel, B. Thirion, O. Grisel, M. Blondel, P. Prettenhoffer, R. Weiss, V. Duborg, J. Vanderplas, A. Passos, D. Cournapeau, M. Brucher, M. Perrot, and E. Duchesnay, 2011: Scikit-learn: Machine learning in Python. *Journal of Machine Learning Research*, **12**, 2825-2830 pp. http://scikit-learn.sourceforge.net. (Accessed February 13, 2019).

QGIS Development Team (2019). **QGIS** Geographic Information System. Open Source Geospatial Foundation Project. http://**qgis**.osgeo.org

Rasmussen, E. N., and J. M. Straka, 1998: Variations in supercell morphology. Part I: Observations of the role of upper-level storm-relative flow. *Mon. Wea. Rev.*, **126**, 2406–2421, doi:10.1175/1520-0493(1998)126<2406:VISMPI>2.0.CO;2.

Rinehart, R. E., 2010: *Radar for meteorologists: or you, too, can be a radar meteorologist, part III.* Rinehart Publications, Nevada, MS.

Romine, G. S., D. W. Burgess, and R. B. Wilhelmson, 2008: A dual-polarization-radar-based assessment of the 8 May 2003 Oklahoma City area tornadic supercell. *Mon. Wea. Rev*, **136**, 2849-2870, doi:10.1175/2008MWR2330.1.

Rotunno, R. and J. B. Klemp, 1982: The influence of the shear-induced pressure gradient on thunderstorm motion. *Mon. Wea. Rev.*, **110**, 136–151, doi:10.1175/1520-0493(1982)110<0136:TIOTSI>2.0.CO;2.

—— and —— , 1985: On the rotation and propagation of simulated supercell thunderstorms. *J. Atmos. Sci.*, **42**, 271–292, doi:10.1175/1520-0469(1985)042<0271:OTRAPO>2.0.CO;2.

Ryzhkov, A. V., T. J. Schuur, D. W. Burgess, and D. S. Zrnic, 2005: Polarimetric tornado detection. *J. Appl. Meteor. Climatol.*, 44, 557–570, doi:10.1175/jam2235.1.

Seliga, T. A., and V. N. Bringi, 1976: Potential use of radar differential reflectivity measurements at orthogonal polarizations for measuring precipitation. *J. Appl. Meteorol. Climatol.*, **15**, 69–76, doi:10.1175/1520-0450(1976)015<0069:PUORDR>2.0.CO;2.

Snyder, J. C., and A. V. Ryzhkov, 2015: Automated detection of polarimetric tornadic debris signatures using a hydrometeor classification algorithm. *J. Appl. Meteorol. Climatol.*, **54**, 1861–1870, doi:10.1175/JAMC-D-15-0138.1.

——, ——, M. R. Kumjian, A. P. Khain, and J. Picca, 2015: A Z_{DR} column detection algorithm to examine convective storm updrafts. *Wea. Forecasting,* **30,** 1819–1845, doi:10.1175/WAF-D-15-0068.1.

Thompson, R. L., R.L. Edwards, J.A. Hart, K.L Elmore, and P. Markowski, 2003: Close proximity soundings within supercell environments obtained from the rapid update cycle. *Wea. Forecasting,* **18**, 1243–1261, doi:10.1175/1520-0434(2003)018<1243:CPSWSE>2.0.CO;2.

——, B.T. Smith, J.S. Grams, A.R. Dean, J.C. Picca, A.E. Cohen, E.M. Leitman, A.M. Gleason, and P.T. Marsh: 2017: Tornado damage rating probabilities derived from WSR-88D data. *Wea. Forecasting*, **32**, 1509–1528, doi:10.1175/WAF-D-17-0004.1.

Trapp, R. J., G. J. Stumpf, and K. L. Manross, 2005: A Reassessment of the percentage of tornadic mesocyclones. *Wea. Forecasting*, **20**, 680–687, doi:10.1175/WAF864.1.

Van Den Broeke, M. S., 2016: Polarimetric variability of classic supercell storms as a function of environment. *J. Appl. Meteor. Climatol.*, **55**, 1907–1925, doi:10.1175/JAMC-D-15-0346.1.

——, 2017: Polarimetric radar metrics related to tornado life cycles and intensity in supercell storms. *Mon. Wea. Rev.*, **145**, 3671–3686, doi:10.1175/MWR-D-16-0453.1.

——, and S. T. Jauernic, 2014: Spatial and temporal characteristics of polarimetric tornadic debris signatures. *J. Appl. Meteor. Climatol.*, **53,** 2217–2232, doi:10.1175/JAMC-D-14-0094.1.

——, and C. A. Van Den Broeke, 2015: Polarimetric radar observations from a waterspout-producing thunderstorm. *Wea. Forecasting.*, **30**, 329–348, doi:10.1175/WAF-D-14-00114.1.

——, J. M. Straka, and E. N. Rasmussen, 2008: Polarimetric radar observations at low levels during tornado life cycles in a small sample of classic southern plains supercells. *J. Appl. Meteor. Climatol.*, **47**, 1232–1247, doi:10.1175/2007JAMC1714.1.

Ward, A, M. Kumjian, M. J. Bunkers, S. W. Bieda III, and R. J. Simpson, 2018: Using polarimetric radar to identify potentially hazardous hail accumulations. *98th Amer. Meteor. Soc. Annual Meeting,* Austin, TX, 11B.1

Weisman, M. L. and J. B. Klemp, 1982: The dependence of numerically simulated convective storms on vertical wind shear and buoyancy. *Mon. Wea. Rev.*, **110**, 504–520, doi:10.1175/1520-0493(1982)110<0504:TDONSC>2.0.CO;2.

Weiss, C. C., D. C. Dowell, J. L. Schroeder, P. S. Skinner, A. E. Reinhart, P. M. Markowski, and Y. P. Richardson, 2015: A comparison of near-surface buoyancy and baroclinity across three VORTEX2 supercell intercepts. *Mon. Wea. Rev.*, **143**, 2736–2753, doi:10.1175/MWR-D-14-00307.1.

Wilhelmson, R. B., and J. B. Klemp, 1978: A numerical study of storm splitting that leads to long-lived storms. *J. Atmos. Sci.*, **35**, 1974–1986, doi:10.1175/1520-0469(1978)035<1974:ANSOSS>2.0.CO;2.

Zrnic, D. S. and A. V. Ryzhkov, 1999: Polarimetry for weather surveillance radars. *Bull. Amer. Meteor. Soc.*, **80**, 389–406, doi:10.1175/1520-0477(1999)080<0389:PFWSR>2.0.CO;2.